KARADENİZ TECHNICAL UNIVERSITY
THE GRADUATE SCHOOL OF NATURAL AND APPLIED SCIENCES

DEPARTMENT OF CIVIL ENGINEERING

FREE VIBRATION, BENDING, AND BUCKLING ANALYSIS OF CARBON NANOTUBE-REINFORCED COMPOSITE BEAMS USING HIGHER-ORDER SHEAR DEFORMATION THEORY

MASTER THESIS

Serhan KOÇ

JUNE 2024
TRABZON

KARADENİZ TECHNICAL UNIVERSITY

THE GRADUATE SCHOOL OF NATURAL AND APPLIED SCIENCES

DEPARTMENT OF CIVIL ENGINEERING

FREE VIBRATION, BENDING, AND BUCKLING ANALYSIS OF CARBON NANOTUBE-REINFORCED COMPOSITE BEAMS USING HIGHER-ORDER SHEAR DEFORMATION THEORY

Serhan KOÇ

ORCID : - - -

This thesis is accepted to give the degree of

"MASTER OF SCIENCE"

By

The Graduate School of Natural and Applied Sciences at Karadeniz Technical University

The Date of Submission : 28 / 05 /2024

The Date of Examination : 28 / 06 /2024

Supervisor : Asst. Prof. Gökhan ADIYAMAN

ORCID : - - -

Trabzon 2024

ACKNOWLEDGEMENT

I would like to express my deepest gratitude to my supervisor Asst. Prof. GÖKHAN ADIYAMAN for his guidance, recommendations, trust and encouragement throughout this research and preparation of this thesis.

At the end of the Master program, I thank God for giving me the strength to accomplish this thesis, and for His blessings, strength, and guidance.

I dedicate this work to my parents and brothers. I offer them my sincere love, gratitude, and appreciation for their love, support, patience, and understanding throughout the entire journey.

Serhan KOÇ

Trabzon 2024

DECLARATION PAGE

I have submitted this study titled " Free Vibration, Bending, And Buckling Analysis Of Carbon Nanotube-Reinforced Composite Beams Using Higher-Order Shear Deformation Theory ", which I submitted as a Master's Thesis, from beginning to end, by my supervisor, Asst. Prof. GÖKHAN ADIYAMAN, that I have collected the data/samples myself, that I have fully indicated the information I received from other sources in the text and in the bibliography, that I have acted in accordance with scientific research and ethical rules during the working process, and that I have made all kinds of decisions in case the opposite arises. I declare that I accept the legal result. 28/06/2024

Serhan KOÇ

TABLE OF CONTENTS

Yüksek Lisans

ÖZET

YÜKSEK MERTEBE KAYMA DEFORMASYON TEORİSİ KULLANILARAK KARBON NANOTÜP TAKVİYELİ KOMPOZİT KİRİŞLERİN SERBEST TİTREŞİM, EĞİLME VE BURKULMA ANALİZİ

Serhan KOÇ

Karadeniz Teknik Üniversitesi
Fen Bilimleri Enstitüsü
İnşaat Mühendisliği Anabilim Dalı
Danışman: Dr. Öğr. Üyesi Gökhan ADIYAMAN
2024, 129 Sayfa

Tez, özgün bir sonlu eleman modeli ve yüksek mertebe kayma deformasyon teorisi kullanılarak karbon nanotüp takviyeli kompozit kirişlerin serbest titreşim, eğilme ve burkulma analizini yapmayı amaçlamaktadır.

Birinci bölüm, insanlığın yapı malzemeleri arayışının ve yapıda kullanılan malzemelerin tarihsel bir perspektifini sunarak, karbon nanotüp malzemesinin özelliklerini ve potansiyelini detaylıca ele alır. Daha sonra geçmişte yapılmış çalışmaları kronolojik sırayla sunmaktadır. İkinci ve üçüncü bölüm, yapılan çalışmaları, elde edilen bulguları ve bu bulguların değerlendirilmelerini ele almaktadır. Öncelikle sonlu eleman modeli oluşturulmuş ve yer değiştirme denklemleri elde edilmiştir. Daha sonra potansiyel, kinetik ve iş denklemleri hesaplanmıştır. Hareket denklemi Lagrange bağıntılarıyla çözülmüştür. Analizler için yakınsama kontrolü yapılmıştır. Serbest titreşim, eğilme ve burkulma analizleri için hesaplamalar yapılmış ve literatürde diğer sonuçlarla karşılaştırılmıştır. Bu sonuçlar araştırmayı doğrulamıştır. Dördüncü bölümde, çalışma neticesinde elde edilen bulgular ve gelecek araştırmalar için yol gösterici nitelikte öneriler detaylı bir şekilde sunulmuştur. Son bölüm ise bu çalışmada yararlanılan kaynaklara yer verilmiştir.

Anahtar Kelimeler: Karbon nanotüp, Sonlu Elemanlar Yöntemi, Yüksek Mertebe Kayma Deformasyon Teorisi, Serbest Titreşim, Burkulma, Eğilme

Master's Thesis

SUMMARY

FREE VIBRATION, BENDING, AND BUCKLING ANALYSIS OF CARBON NANOTUBE-REINFORCED COMPOSITE BEAMS USING HIGHER-ORDER SHEAR DEFORMATION THEORY

Serhan KOÇ

Karadeniz Technical University
The Graduate School of Natural and Applied Sciences
Civil Engineering Graduate Program
Supervisor: Asst. Prof. GÖKHAN ADIYAMAN

2024, 129 Pages

The paper aims the free vibration, bending, and buckling analysis of carbon nanotube-reinforced composite beams are performed using a novel finite element model and a high-order shear deformation theory.

Chapter 1 delves into the historical journey of humanity's pursuit of building materials and the evolution of materials utilized in construction. It further explores the characteristics and potential of carbon nanotube materials in detail, followed by a chronological overview of past research conducted in this field. Chapter 2 and 3 focuses on the current study, encompassing the methodologies employed, the findings obtained, and their subsequent evaluation. A finite element model is established, and displacement equations are derived. Potential, kinetic, and work equations are calculated, and the equation of motion is solved using Lagrange's equations. Convergence control is meticulously implemented for all analyses. Calculations for free vibration, bending, and buckling analyses are performed and compared with existing results in the literature, validating the research approach. Chapter 4 meticulously presents the findings derived from the study and provides insightful recommendations to guide future research endeavors. The concluding chapter presents a thorough compilation of references employed in this research.

Key Words: Carbon Nanotube; Finite Element Method; High Order Shear Deformation Theory, Free Vibration, Bending, Buckling

LIST OF FIGURES

Page

LIST OF TABLES

Page

LIST OF SYMBOLS AND ABBREVIATIONS

CNT	: Carbon nanotube
$SWCNT$	: Singe-walled CNT
$MWCNT$	: Multi-walled CNT
UD	: Uniformly distributed
FG	: Functionally graded
FGA	: Functionally graded-A
FGX	: Functionally graded-X
FGO	: Functionally graded-O
FG-CNTRC	: Functionally graded carbon nanotube reinforced composite
$CNTRC$	: Carbon nanotube reinforced composite
V_{tcnt}	: Total volume fraction of the carbon nanotube
V_{cnt}	: Volume fraction of the carbon nanotube
θ	: Orientation angle
Lt/h	: Slenderness ratio
K	: Stiffness matrix
M	: Mass matrix
K_G	: Geometric stiffness matrix
F	: Force matrix
C-C	: Clamped-Clamped
S-S	: Simple-Simple
C-S	: Clamp-Simple
C-F	: Clamp-Free
ω	: Frequency
$\bar{\omega}$	: Non-dimensional frequency
N_{cr}	: Critical buckling load
$\bar{N}_{cr}$	: Non-dimensional buckling load
$\bar{w}$	: Non-dimensional vertical displacement
$\bar{\sigma}_{xx}$	: Non-dimensional normal stress
$\bar{\sigma}_{xz}$	: Non-dimensional shear stress

1. GENERAL INFORMATION

1.1. Introduction

Humans have always been in search of ways to sustain their lives. The basic needs of better agriculter, shelter and transportation have shaped the development of other needs. As technology has advanced, structures have also advanced in a similar way.The materials used have changed, and they have benefited humanity according to the prevailing weather conditions and geography. Engineers have sought materials with better durability to move society forward. Throughout the realm of engineering, humanity is perpetually seeking materials that are dependable, cost-effective, and less detrimental to the environment. The materials used in the early ages were natural materials. These materials were earth, stone, wood and animal skins. In the Middle Ages, metals began to be used in structures. Metals were preferred because they were more durable and long-lasting than natural materials. Structural materials have also developed with the advancement of technology. In the modern era, new materials began to be used in structural materials with the development of chemical science. These materials were concrete and steel. Concrete and steel are two fundamental construction materials with distinct properties and applications. Concrete, a composite material composed of cement, sand, and water, is renowned for its compressive strength and durability. Steel, an alloy of iron, is valued for its tensile strength, versatility, and malleability.

The construction industry has long relied on two fundamental materials: concrete and steel. However, the rapid development of technology has made nanotechnology an inevitable part of our future, and it has become one of the most important topics of our time. Materials such as nanoparticles, thin films, and nanotubes, with their unique physical properties and the shrinking of sizes, offer a wide range of applications in technology. Nanotechnology is defined as the study and application of materials, devices, and systems at the nanoscale, which is about 1 to 100 nanometers in size. A nanometer is one billionth (10^{-9}) of a meter, which is about 100,000 times smaller than the width of a human hair. The impact of nanoscience and nonotechnology on strcutural materials will enable significant developments in structural materials.

1.2. Materials Used for Construction

The advent of composite materials has revolutionized various industries, including construction, due to their exceptional properties that surpass those of traditional materials. Composite materials are engineered combinations of two or more distinct materials that result in enhanced properties that outperform their individual components. They offer a unique combination of desirable characteristics such as high strength, lightweight, and resistance to corrosion, making them the material of choice for a wide range of applications. Table 1 highlights the evolution of materials over time.

Table 1. Material used through history

Era	***Material***
Prehistory	Wood, Earth, and Stone
Ancient Times	Brick, Marble, Concrete
Middle Ages	Stone and Concrete
Industrial Revolution	Steel
20th Century	Concrete and Steel
21st Century	Fiberglass and composite materials

The ongoing advancements in composite materials continue to drive innovation and open up new possibilities for engineers and designers such as carbon nanotubes(CNTs) and graphene, to further enhance the properties of composites.

By adding fiberglass to plastic, the resulting composites were not only stronger and stiffer but also had higher resistance to environmental factors and corrosion. This made it ideal for numerous industrial and commercial applications.

In the 1960s, the era of carbon fiber composites began. Carbon fiber, which has excellent stiffness, strength, and thermal resistance, quickly became the material of choice for demanding applications in the aerospace, automotive, and electronics industries.

Additionally, carbon fiber composites have numerous technological applications, from high-performance sports equipment such as tennis rackets and bicycles to electronic devices, including laptops, smartphones, and headphones.

Today, composite materials continue to develop, with researchers exploring new avenues for reinforcement, such as nanotubes and graphene, aiming to improve their properties even further. The potential for composite materials is vast, and they hold a vital role in shaping the future of various industries.

1.3. Carbon Nanotubes:CNTS

Their discovery in 1991 by Japanese scientist Sumio Iijima marked a significant milestone in materials science and sparked a surge of research into their properties and applications.

The concept of CNTs, however, dates to 1952 when German scientist Manfred M. Schwarz theoretically predicted their existence based on his understanding of graphite's structure. Schwarz envisioned CNTs as cylindrical structures composed of carbon atoms arranged in a hexagonal lattice, like the arrangement in graphene sheets.

In the early 1980s, Russian scientists, including Evgeny Dodatko and Vladimir E. Nazarov, independently reported the synthesis of CNTs using an electric arc discharge method. However, these early CNTs were of poor quality and not well understood, hindering further research and development.

It was Iijima's remarkable discovery in 1991 that brought CNTs into the spotlight. Using arc-evaporation techniques, Iijima produced high-quality CNTs with diameters ranging from 0.7 to 1.3 nanometers. He observed that these CNTs were formed by rolling up a single layer of graphene, a two-dimensional form of carbon, into a seamless cylinder.

Iijima's work sparked a revolution in nanotechnology, as scientists around the world began to explore the unique properties of CNTs: high tensile strength, low density and high stiffness, excellent electrical conductivity, high thermal conductivity.

1.3.1. Types of CNTs

CNTs are cylindrical nanostructures made of carbon atoms arranged in a hexagonal lattice. They are a form of fullerene, a class of nanomaterials composed entirely of carbon atoms. CNTs have a diameter of just a few nanometers, but they can be several micrometers long. They can be categorized into two main types: single-walled carbon nanotubes (SWCNTs), consisting of a single layer of carbon atoms, and multi-walled carbon nanotubes (MWCNTs), composed of multiple concentric layers.

The geometry of a CNT is defined by the chiral vector $\mathbf{C_h}$ and the chiral angle θ. The chiral vector is represented by two unit vectors $\alpha 1$ and $\alpha 2$ and two integers m and n (Yengejeh et al., 2015) .

The base configuration of CNTs can be described based on the chiral vector or angle by which the sheet is rolled into a cylinder, as shown in Fig. 1.

An armchair CNT is formed, regarding chiral vector (m = n) or with respect to chiral angle (ϑ = 30°), as shown in Fig. 2.

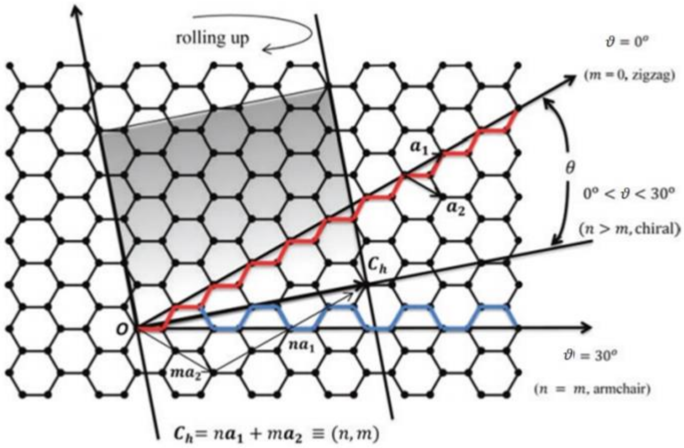

Figure 1. Schematic of a graphene sheet and definition of geometrical parameters for describing a CNT

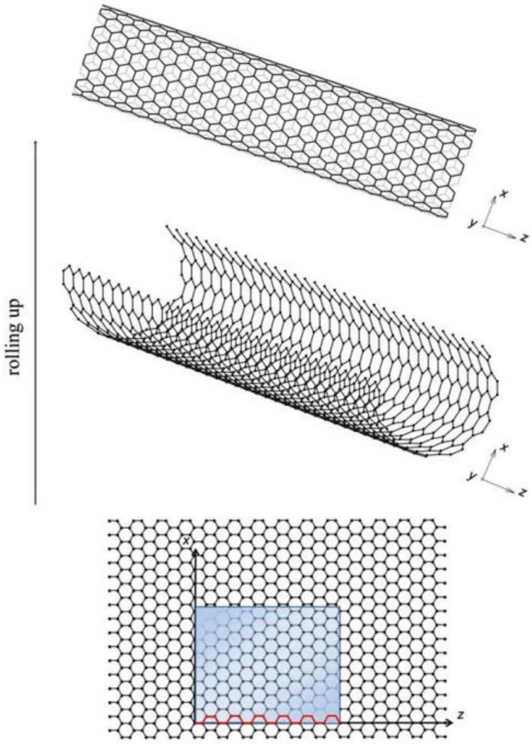

Figure 2. Rolling up process of a graphene sheet into an armchair tube

1.3.2. Single-walled Carbon Nanotubes (SWCNTs)

SWCNTs are the simplest type of CNT, consisting of a single layer of carbon atoms arranged in a hexagonal lattice. The diameter of SWCNTs can range from about 0.8 nanometers to about 3 nanometers. SWCNTs can be either metallic or semiconducting, depending on their chirality, which is the arrangement of carbon atoms in the hexagonal lattice. Metallic SWCNTs exhibit exceptional electrical conductivity, approaching that of copper. Semiconducting SWCNTs have tunable bandgaps, making them suitable for electronic applications.

1.3.3. Multi-walled Carbon Nanotubes (MWCNTs)

MWCNTs are composed of multiple layers of carbon atoms arranged in a concentric fashion. The diameter of MWCNTs can range from about 3 nanometers to about 100 nanometers. MWCNTs are typically metallic and exhibit high electrical conductivity. The types of CNTs are shown in Figure 3.

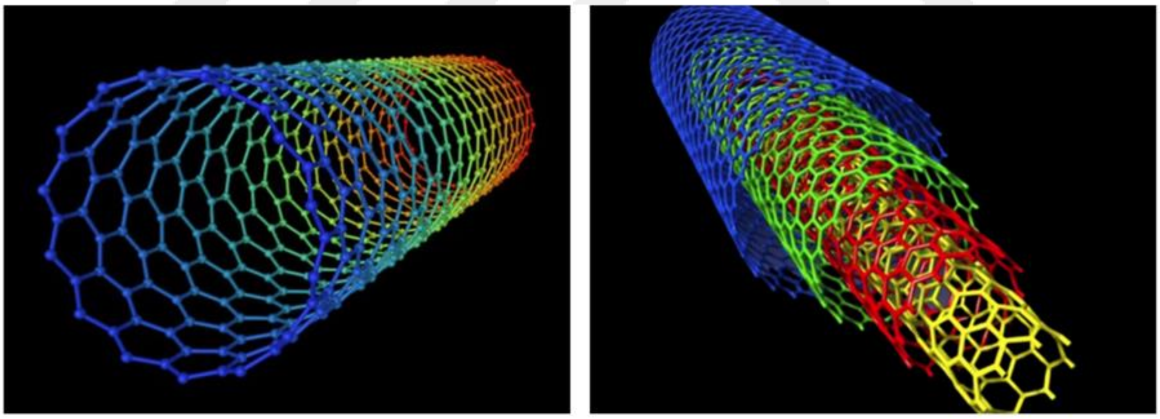

(a) (b)

Figure 3. Types of CNTs (a) SWCNT and (b) MWCNT

1.3.4. CNTs Mechanical Properties

CNTs are the strongest and stiffest materials known, with exceptional electrical and thermal conductivity. They are also lightweight and chemically resistant. However, they are also expensive to produce.

CNTs have the potential to revolutionize a wide range of industries, including aerospace, automotive, electronics, energy and construction. This extraordinary tensile strength allows CNTs to withstand significant stress without deformation or fracture, making them ideal for applications demanding exceptional strength-to-weight ratios. Young's modulus, a measure of a material's stiffness or rigidity, represents the stress required to cause a given strain in the material. This remarkable stiffness allows CNTs to resist deformation under applied forces, making them incredibly stiff and resistant to bending or stretching. Compressive strength values for CNTs range from 20 to 60 GPa.

Table 2 presents analysis of the elastic modulus and tensile strength for a range of materials, highlighting the superior mechanical properties of CNTs and diamond. Diamond exhibits the highest Young's modulus, indicating exceptional stiffness and resistance to elastic deformation, followed closely by both single-walled and multi-walled CNTs. Steel, concrete, and wood demonstrate significantly lower Young's moduli, suggesting their relative flexibility compared to the materials.

Table 2. Properties of most used materials(Kausar et al., 2017)

Property	**SWCNT**	**MWCNT**	**Diamond**	**Steel**	**Concrete**	**Wood**
Elastic modulus (GPa)	1054	1200	1210	200	27-37	16
Tensile strength (MPa)	$150*10^3$	$150*10^3$	2930	400	1,4-2,5	8

Furthermore, diamond demonstrates the highest tensile strength, signifying its superior ability to withstand tensile loading without failure. SWCNTs and MWCNTs exhibit remarkable tensile strength, surpassing steel and significantly exceeding that of concrete and wood. This underscores the potential of CNTs as reinforcement in applications demanding high strength and load-bearing capacity.

1.3.5. Methods of Obtaining CNTs

There are several methods for synthesizing CNTs, each with its own advantages and limitations. Some of the most common methods are given in Table 3.

Table 3. Methods of obtaining CNTs (Baddour & Briens, 2005)

Method	***Description***	***Advantages***	***Disadvantages***
Arc discharge	CNT growth on graphite electrodes during direct current arc-discharge evaporation of carbon in presence of an inert gas	* Simple, inexpensive	* Purification of crude product is required, method cannot be scaled up, must have high temperature
Chemical vapor deposition	Fixed bed method: acetylene decomposition over graphite-supported iron particles at 700° C	* Simple, inexpensive, low temperature, high purity, and high yields, aligned growth is possible, fluidized bed technique for large-scale	* CNTs usually are MWCNTs, parameters must closely be watched to obtain SWCNTs
Laser ablation	Vaporization of a mixture of carbon (graphite) and transition metals located on a target to form CNTs	* Relatively high purity CNTs, room temperature synthesis option with continuous laser	* Cannot produce MWCNTs, method only adapted to lab-scale, crude product purification required

The selection of CNT production method hinges on the specific demands of the application. Arc discharge is an appropriate choice for applications where low cost is paramount. Chemical vapor deposition is a suitable choice for applications that necessitate high control over properties. Laser ablation is a favorable choice for applications that require high purity. Arc discharge is a prevalent method for producing CNTs.

1.3.6. Examples of CNT Used in Sectors

As the cost of CNT production continues to decrease, CNT composites are poised to revolutionize a wide range of industries. Their potential for lightweight, high-strength, and multifunctional structures is transforming the design and performance of products across various sectors, including:

General Electric is employing CNTs in the blades of their wind turbines to enhance their structural integrity, longevity, and overall performance. CNTs, a type of nanomaterial boasting exceptional properties such as superior strength, exceptional electrical conductivity, and remarkable thermal conductivity, are being seamlessly integrated into wind turbine blades, enabling the creation of lighter, stronger, and more efficient blades.

Intel is pioneering the use of CNTs in the semiconductor industry to create advanced transistors that are smaller, faster, and more energy efficient. As silicon transistors reach their physical miniaturization limits, CNTs offer a promising alternative due to their exceptional one-dimensional structure and ability to be synthesized at atomic scales. While current CNT transistors have not yet matched the performance of top silicon transistors, there is potential for them to become superior with further research. In the interim, integrating CNT and silicon transistors could lead to enhanced circuitry and scalability in electronic devices.

The Shimizu Mega-City Pyramid, a visionary 2004-meter-tall city design conceived by Japanese architects, comprises 55 smaller pyramids stacked in eight layers. This colossal structure necessitates exceptionally strong yet lightweight materials like carbon nanotubes (CNTs), as conventional materials would be too heavy for such a massive construction. The remarkable Young's modulus and tensile strength of CNTs make them ideal for producing ultra-strong cables used in long-span bridges. For instance, the two recently constructed cable-stayed bridges flanking the existing Longfellow Bridge, designed by ASN, boast back spans of 128 meters and a main span of 256 meters. Looking towards the future, Tokyo's Obayashi Corp envisions Space Elevation 2050, a space station positioned 36,000 kilometers above Earth, connected by a 96,000-kilometer-long cable constructed from CNTs. This ambitious project even proposes an elevator system to transport tourists into space (Yang, 2023).

1.4. Literature Review

In 1991, Japanese scientists Sumio Iijima (Iijima, 1991) and Takashi Ichihashi published the first detailed microscopic images of CNTs, which were produced by heating graphite through an electric arc. These images revealed that CNTs had a tubular structure with walls composed of a single atomic layer. The work of Iijima and Ichihashi opened a new frontier in the research and development of CNTs. CNTs were quickly recognized as powerful and lightweight materials with extraordinary mechanical, electrical, and thermal properties.

Thostenson et al. (2001) present a thorough examination of the advancements made in CNTs and their composites. In the publication, the authors delve into the synthesis methods, properties, and potential applications of CNTs, with a specific emphasis on their viability in composite materials. The paper additionally underscores the ongoing challenges in CNT-based composite development, while proposing avenues for future research.

Vodenitcharova and Zhang (2006) conducted a study investigating the bending-induced local buckling and pure bending behavior of nanocomposite beams reinforced with single-walled carbon nanotubes (SWNTs). Their analysis employed the Airy stress-function method to examine the deformation of the matrix material while accounting for cross-sectional changes in the SWNT during bending. A key focus of their research was the influence of SWNT radial flexibility on the strain and stress states, as well as the overall buckling behavior of the nanocomposite structure. The study revealed that thicker matrix layers resulted in local buckling of the SWNT at smaller bending angles and higher flattening ratios. This, in turn, led to elevated strain and stress levels within the surrounding matrix, ultimately causing a degradation in the overall strength of the nanocomposite.

Han and Elliott (2007) explored the potential of CNTs to improve the structural, mechanical, and electronic properties of polymeric materials. Utilizing classical molecular dynamics (MD) simulations, they investigated model polymer/CNT composites, embedding a single-walled (10, 10) CNT into two distinct amorphous polymer matrices: poly(methyl methacrylate) (PMMA) and poly(m-phenylenevinylene) (PmPV). Their findings indicated that CNTs can effectively reinforce a suitable polymer matrix, particularly along the longitudinal axis of the nanotube.

Murmu and Pradhan (2009) employed the differential transformation method (DTM) to predict the buckling behavior of SWCNTs embedded in Winkler foundations and subjected to various boundary conditions. Their study explored the effects of SWCNT size, nonlocal parameter, and Winkler elastic modulus on the nonlocal critical buckling loads. The implementation of DTM for the nonlocal SWCNT analysis demonstrated high accuracy in predicting buckling behavior. Furthermore, the researchers noted the applicability of their method to both linear and nonlinear problems.

Zadeh et al. (2012) axial compressive, bending, and torsional loading conditions. Their study utilized a structural mechanics model, incorporating nonlinear spring elements to represent the influence of van der Waals forces between the nanotubes. The research explored the effects of various boundary conditions on the buckling behavior of nanotubes with different aspect ratios.

Thai and Vo (2012) presented the development of several higher-order shear deformation beam theories for the analysis of bending and free vibration behavior in FG beams. These theories incorporate higher-order variations of transverse shear strain through the beam's depth and satisfy stress-free boundary conditions on both the top and bottom surfaces. Equations of motion and boundary conditions were derived using Hamilton's principle. The study further examined the influence of the power law index and shear deformation on the bending and free vibration responses of FG beams.

Yas and Samadi (2012) investigated free vibrations and buckling behavior in nanocomposite Timoshenko beams reinforced with SWCNTs and supported by an elastic foundation. The study assumed straight, aligned, and uniformly distributed SWCNTs, considering four different distribution patterns: uniform distribution and three functionally graded distributions along the beam's thickness. The rule of mixtures was employed to determine the effective material properties of the nanocomposite beams. Hamilton's principle was used to derive the governing equations, which were subsequently solved using the generalized differential quadrature method (GDQM). The analysis provided valuable insights into the natural frequencies and critical buckling loads of the nanocomposite beams under various boundary conditions. Furthermore, the study explored the influence of parameters such as nanotube volume fraction, foundation stiffness, slenderness ratios, CNT distribution patterns, and boundary conditions on the natural frequencies and critical buckling loads of the nanocomposite beams.

Wattanasakulpong and Ungbhakorn (2013) presented analytical solutions for the analysis of bending, buckling, and vibration responses in CNTRC beams resting on elastic foundations. The beams under consideration consisted of a polymeric matrix with aligned and distributed SWCNTs. Various reinforcement patterns were considered, and the rule of mixtures was employed to determine the effective material properties of the CNTRC beams. The researchers utilized several shear deformation theories to analyze the aforementioned structural behaviors. Validation of the mathematical models was achieved through comparison with existing numerical results. Additionally, the study explored the influence of factors such as beam types, spring constant values of the elastic foundation, and the volume fraction of CNTs on the structural responses.

Shen and Xiang (2013) conducted a study exploring the behaviors of large amplitude vibration, nonlinear bending, and thermal post-buckling in nanocomposite beams reinforced with SWCNTs and supported by an elastic foundation in thermal environments. Employing a higher-order shear deformation beam theory, the researchers numerically investigated the nonlinear vibration, nonlinear bending, and thermal post-buckling responses of CNTRC beams resting on Pasternak elastic foundations under various thermal conditions. Their findings revealed that a CNTRC beam with an intermediate CNT volume fraction does not necessarily exhibit intermediate values for nonlinear frequencies, buckling temperatures, and thermal post-buckling strengths.

Pradhan and Mandal (2013), investigated the vibration, buckling, and bending behavior of CNTs using finite element analysis. Their study integrated nonlocal Timoshenko beam theory with thermal sensitivity, enabling a comprehensive examination of thermal effects on the nonlocal and thermal elasticity of CNTs. The analysis explored the influence of geometrical properties, the nonlocal parameter, and environmental temperature variations on the structural response. The findings offer valuable insights for the design and development of advanced nanodevices and structures incorporating CNTs.

Şimşek and Reddy (2013) conducted a study on the static bending and free vibration of functionally graded (FG) microbeams, employing the modified couple stress theory (MCST) and various higher-order beam theories (HOBTs). Their non-classical microbeam model incorporated a material length scale parameter to account for size effects. Hamilton's principle was utilized to derive the governing equations and associated boundary conditions. The researchers developed a Navier-type solution for microbeams with simply supported boundary conditions. Numerical results were presented to examine the influence of the material length scale parameter, different material compositions, and shear deformation on the bending and free vibration behavior of FG microbeams.

Ansari et al. (2014) studied the forced vibration behavior of nanocomposite beams reinforced with SWCNTs using TBM and incorporating von Kármán geometric nonlinearity. The nonlinear governing equations and corresponding boundary conditions were derived through Hamilton's principle and subsequently discretized using the generalized differential quadrature (GDQ) method. Numerical results were presented to analyze the influence of various parameters, including nanotube volume fraction, slenderness ratio, dimensionless damping parameter, dimensionless transverse force, CNT distribution patterns, and boundary conditions, on the natural frequencies and frequency responses of functionally graded carbon nanotube-reinforced composite (FG-CNTRC) beams.

Lin and Xiang (2014) examined the linear free vibration of nanocomposite beams reinforced with SWCNTs. The virtual strain and kinetic energies of the functionally graded carbon nanotube (FG-CNT) composite beams were determined using the classical variational method of Hamilton's principle. Subsequently, the p-Ritz method was employed to solve the equations of motion. The study presented vibration frequency parameters for FG-CNT beams based on both first-order and third-order beam theories, highlighting the differences in vibration frequencies predicted by each theory. Tagrara et al. (2015) presented a study on a trigonometric refined beam theory for the analysis of bending, buckling, and free vibration of CNTRC beams resting on an elastic foundation. This model offers the advantage of accounting for shear deformation effects while utilizing only three unknowns, similar to the TBM, without the need for a shear correction factor. Furthermore, the study investigated the influence of various beam parameters on the bending, buckling, and free vibration responses of CNTRC beams.

Mustafa and Aydogdu (2016) investigated the bending behavior of CNTs using the nonlocal Euler-Bernoulli beam model. Their study explored the influence of nonlocality, characteristic length ratio, and the magnitude of applied external uniform load on the bending response of CNTs.

Chaudhari and Lal (2016), delves into the buckling and free vibration of nanocomposite beams reinforced with FG, agglomerated CNTs in a polymer matrix. Material properties are estimated using the Eshelby-Mori-Tanaka rule, while Lagrange's principle and refined higher-order beam theory are employed to derive governing equations. The differential quadrature finite element method then computes natural frequencies and buckling loads for diverse boundary conditions.

García-Macías et al. (2017) conducted a study on the linear buckling analysis of FG-CNTRC cylindrical curved panels subjected to compressive and shear loading. Effective material properties for panels reinforced with SWCNTs were estimated using micromechanical models based on either the Eshelby-Mori-Tanaka approach or the extended rule of mixtures. The researchers performed a series of numerical simulations to investigate the influence of curvature, panel aspect ratio, reinforcement distribution profile (uniform and three non-uniform distributions), and CNT orientation angle on the critical buckling load under compressive and shear loading within uniform thermal environments. The results demonstrated that variations in fiber orientation, CNT distribution, panel aspect ratio, loading conditions, and temperature significantly impact the buckling strength and buckling modes of FG-CNTRC curved panels.

Kumar and Srinivas (2017a) presented a numerical analysis investigating the static and dynamic behavior of beams composed of FG-CNTRC and hybrid laminated composites consisting of carbon-reinforced polymer with CNT layers. The Timoshenko beam theory was employed to determine the stress and strain formulations for the multi-layered composite system. Additionally, the study conducted free vibration, bending, and buckling analyses on the FG-CNTRC beam to investigate the influence of factors such as CNT volume fraction, number of walls in the nanotube, distribution profiles, boundary conditions, and beam slenderness ratios.

Kumar and Srinivas (2017b) explored the potential of polymer nanocomposites reinforced with uniformly dispersed and randomly oriented multi-walled carbon nanotubes (MWCNTs) for use in functionally graded (FG) structural components. Their study investigated the static and dynamic behavior of FG polymer composite plates reinforced with randomly oriented MWCNTs using a novel layer-wise formulation approach. Based on generalized HSDT, a system of governing equations was derived. The Navier technique was employed to obtain solutions for free vibration, buckling, and static bending problems of simply supported plates under axial and transverse loading conditions with varying aspect ratios. Parametric studies were conducted to examine the influence of key reinforcement and plate parameters on the natural frequencies, critical buckling loads, and bending deflections.

Arefi et al. (2017), explores the nonlinear-free vibration responses of sandwich nano-beams with FG face-sheets reinforced with CNTs. The analysis incorporates higher-order shear deformation beam theories and nonlocal strain gradient theory. The nano-beam is subjected to thermal and electrical loads, resting on a nonlinear Pasternak foundation. The governing equations are derived using Hamilton's principle based on various shear deformation theories and solved using the differential quadrature method.

Ebrahimi and Rostami (2018), explores the propagation of waves in CNTRC beams resting on a Winkler elastic foundation. The analysis considers four distribution patterns for SWCNTs within the polymer matrix and employs the rule of mixture for simplified mechanical property calculations. Additionally, it compares various shear deformation theories explored in previous studies. The governing equations are derived using the extended Hamilton's principle, obtained through energy methods, and subsequently solved analytically. The validity of the results is confirmed by previous investigations, paving the way for future research in wave propagation within CNTRC structures.

Mohammadimehr et al. (2018) presents an experimental tensile test and the manufacturing process of a CNTRC. Additionally, various beam theories such as Euler-Bernoulli, Timoshenko, and Reddy beams are considered for the bending, buckling, and vibration analysis of CNTRC. Theoretical analysis demonstrated that the minimum deflection occurred in bending analysis. Young's modulus, shear modulus, and density were obtained through experimental tests, in contrast to relying on results from previous research. These obtained mechanical properties were then used for the theoretical analysis of bending, buckling, and vibration in this study.

Alimirzaei et al. (2019), investigates the nonlinear static, buckling, and vibration behavior of a viscoelastic micro-composite beam reinforced with varying distributions of boron nitrid nanotubes (BNNTs). The analysis incorporates initial geometrical imperfections and utilizes the modified strain gradient theory (MSGT) within a finite element framework. Stress components are calculated through piezo elasticity theory, accounting for mechanical, electrical, and thermal contributions. The governing equations of motion are derived using the energy method and Hamilton's principle, implemented within the context of MSGT. Subsequently, the finite element method is employed to solve the derived equations.

Vo-Duy et al. (2019) investigated the free vibration of laminated FG-CNTRC beams. Using the first-order shear deformation theory, they formulated a governing equation for predicting the free vibration behavior. This equation was then solved numerically via the finite element method under various boundary conditions. They conducted several numerical tests to analyze the impact of various factors including CNTs volume fractions, distributions, orientation angles, boundary conditions, length-to-thickness ratios, and the number of layers. Additionally, they examined a laminated composite beam incorporating various types of CNTs distributions.

Bousahla *et al.* (2020) examined the buckling and vibration behavior of a composite beam reinforced with CNTRCs on a Winkler-Pasternak elastic foundation. The CNTRC beam was modeled using a new first-order shear deformation theory. This novel theory includes three variables and employs shear correction factors. The equivalent properties of the CNTRC beam were calculated using the mixture rule. The equations of motion were derived and solved by applying Hamilton's principle and the Navier solution to the proposed model.

Kumar and Sarangi (2021), the harmonic response of CNT reinforced functionally graded beams. They considered two different varieties of CNT reinforced composite beams. Finite element models for the beams were generated in the ANSYS environment using the computed material properties.

Karamanli and Vo (2021) investigates bending, vibration and buckling analysis of CNTRC and graphene nanoplatelet-reinforced composite (GPLRC) beams. Both normal and shear effects are included in the formulation of the governing equations of motion of the beams. Equations of motion and boundary conditions of the present theory are derived from Hamilton's principle. The finite element model is employed to determine displacements, critical buckling loads and natural frequencies of the beams with different boundary conditions. Several important factors in parametric studies including distribution pattern, volume fraction of CNTs, GPL weight fraction, slenderness ratio, boundary condition, etc. are investigated.

Zerrouki *et al.* (2021) have developed a novel numerical tool to predict the bending response of CNTRC beams. The study employs the higher-order shear deformation beam theory (HSDT) to establish strain-displacement relationships. The governing equations are derived through Hamilton's principle, and numerical models are presented to validate the accuracy of the proposed theory. The study thoroughly examines and discusses the effects of the aspect ratio (l/d), CNT volume fraction (V_{cnt}), and the order of the exponent (n) on displacements and stresses.

Biswas and Datta (2021) focused on analyzing the free vibration of FG-CNTRC beams. They examined the accuracy and feasibility of different refined deformation theories, such as the first-order shear deformation theory (FSDT) and other theories incorporating higher order terms. The governing equations were derived using Hamilton's principle and solved using the finite element method (FEM) with a C_0 finite element implemented in MATLAB. The study investigated the influence of key parameters, namely CNT volume fraction, distribution type of CNTs, boundary conditions, and slenderness ratio, on the natural frequencies of FG-CNTRC beams.

El-Ashmawy and Xu (2021) addressed the impact of CNT orientation and gradation distribution on the static and free vibration analysis of FG-CNTRC beams. They developed an efficient finite beam element based on the Timoshenko beam theory that can control both parameters effectively. The study focused on using Single-Walled CNTs (SWCNTs) as the primary reinforcement, which were graded through the thickness of the beam. It demonstrated high accuracy and could be extended to accommodate various orientations and grading exponents. This expansion allowed for passive control of beam stiffness and strength without increasing the structural weight or altering constituent material quantities and volume fractions.

Wang et al. (2022) aimed to investigate the buckling performance of a sandwich structure consisting of FG-CNTRC. Analytical model for the sandwich structure of FG-CNTRC was established using the first-order shear deformation theory. The energy method was utilized to obtain the governing equation for predicting the buckling performance of the sandwich structure of FG-CNTRC. Additionally, an analytical solution was achieved that could satisfy both boundary conditions. The theoretical model and method were validated through literature analysis, and the influence of each parameter on the buckling performance was evaluated based on the corroborated model. The findings of this study can provide a solid foundation for the design and application of the sandwich structure of FG-CNTRC.

Dash et al. (2022), investigates the buckling and free vibration behavior of three-phase randomly distributed CNT reinforced fiber composite (RD-CNTRFC) beams subjected to in-plane compressive loads and thermal environments. A semi-analytical approach is employed to delve deeper into this analysis. The governing equations of motion are derived using the Lagrange equation and incorporate higher-order shear deformation theory (HSDT) for displacement-based calculations. The effective material properties of RD-CNTRFC are determined in a two-step process. First, the effective properties of the hybrid matrix (CNTs + Polymer) are evaluated using the Eshelbhy-Mori-Tanaka approach. Subsequently, the overall effective properties of CNTRFC are estimated through the implementation of various homogenization techniques.

Garg et al. (2022) conducted bending and free vibration analyses of sandwich beams reinforced with FG-CNT. A finite element-based higher-order zigzag theory was employed for the study. The face sheets of the beam were assumed to be made of FG-CNTR composite, while the core was assumed to be composed of balsa wood (softcore). The computational model incorporated the consideration of transverse shear stress and transverse normal stress continuity conditions at the interfaces. Additionally, the model ensured the satisfaction of the zero transverse shear stress condition at the top and bottom surfaces of the beam. Furthermore, the analysis utilized the principle of minimum potential energy for bending analysis and Hamilton's principle for free vibration analysis. The investigation focused on analyzing the mechanical behavior of the sandwich FG-CNTRC beam by considering different gradation laws that govern the distribution of CNTs across the thickness of the face sheets.

Madenci et al. (2023) conducted a comprehensive study to investigate the influence of CNT additives on the elastic behavior of textile-based composites. The materials consisted of three phases: carbon fiber fabric, epoxy matrix, and CNTs. Different weight fractions of CNTs were employed, with 0% serving as a reference and 0.3% representing the experimental group. Various mechanical tests, including tension and three-point bending beam tests, were performed to assess the material properties. The experimental results revealed that the samples with CNTs exhibited an average increase of 9% and 23% in axial tensile force and bending capacity, respectively, compared to those without CNTs (NEAT). Furthermore, it was observed that adding 0.3% by weight of MWCNT enhanced the tensile modulus by approximately 9%.

Belarbi et al. (2023) introduce a hyperbolic shear deformation theory and examine its application in analyzing the bending and buckling behavior of FG-CNTRC beams. The proposed theory effectively accounts for the parabolic variation of shear stress distribution across the thickness of the FG-CNTRC beams, satisfying the zero-shear stress condition on the upper and bottom surfaces without requiring correction factors associated with conventional equivalent single-layer theories. The governing equations are solved using a finite element method, and new numerical results are presented to demonstrate the robustness and reliability of the proposed model. Furthermore, the study investigates the influence of various material and geometric parameters, such as the CNTs volume fraction, distribution patterns of CNTs, boundary conditions, and the length-to-thickness ratio, on the bending and buckling responses of FG-CNTRC beam structure.

Eghbali and Hosseini (2023), utilize various higher-order shear deformation theories to investigate the axial and transverse dynamic response of CNTRC beams subjected to a moving harmonic load. The governing equations of the CNTRC beam are derived based on the shear deformation beam theory and the Hamilton principle, leading to an exact solution for the dynamic response through the Laplace transform.

Houalef et al. (2023), delves into the buckling and free vibration of nanocomposite beams reinforced with FG, agglomerated CNTs in a polymer matrix. Material properties are estimated using the Eshelby-Mori-Tanaka rule, while Lagrange's principle and refined higher-order beam theory are employed to derive governing equations. The differential quadrature finite element method then computes natural frequencies and buckling loads for diverse boundary conditions.

1.5. The Purpose and the Scope of the Study

Based on the preceding discussions, it can be inferred that the FG-CNT composite possesses numerous advantages and holds the potential to emerge as a prominent material for multifunctional engineering applications in the future.

Nevertheless, it is noteworthy that the overall behavior of structures constructed using this innovative type of FG-CNT composites has not been comprehensively evaluated.

When the literature is examined, it has been seen that CNT reinforced composite beams have not been adequately examined by using HSDT and FEM together. Section three of this study investigates free vibration, buckling, and bending problems in composite beams reinforced with carbon nanotubes (CNTs). This was conducted using the FEM within the framework of HSDT. The finite element used in the study has twelve degrees of freedom with 3 nodes. Fundamental relations of composite beams reinforced with CNTs were derived by using HSDT. Material properties such as Young's modulus, Poisson's ratio and shear modulus were obtained by the extended mixture rule. Lagrange equations were employed to derive the equation of motion, which was then solved numerically. Dimensionless frequency, mode shapes critical buckling load, buckling modes, displacement, and stress values for various support conditions, different volume ratios and slenderness ratios are given in graphs and tables.

1.5.1. The Distribution of CNTs

The uniform distribution (UD), along with three FG distributions (FGA, FGO, and FGX), of CNTRC beam over the cross-section are shown in Fig. 4. The dimensions of the beam are indicated by L and b, and the height by h.

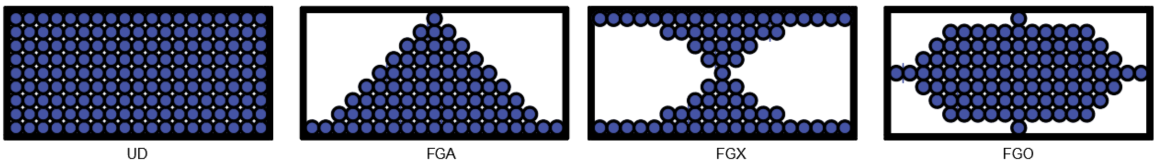

Figure 4. SWCNT patterns in a CNTRC beams UD, FGA, FGX and FGO

The distribution of volume fraction of CNTs (V_{CNT}) can be expressed as a function of the z-axis, where it is defined as the product of the total volume fraction of CNTs (V_{tcnt}) and a position-dependent function.

$$V_{CNT}(z) = V_{tcnt}\mathrm{f(z)} \tag{1}$$

The mechanical properties of composites depend on the volume fraction of the reinforcement and matrix. The effective Young's modulus and shear modulus of CNT composite beams can be determined based on matching the results of the molecular dynamics simulation with the extended mixture rule (Ansari et al., 2014).

$$E_{11}(z) = \eta_1 V_{CNT}(z) E_{11}^{CNT} + V_m(z) E^m \tag{2}$$

$$\frac{\eta_2}{E_{22}(z)} = \frac{V_{CNT}(z)}{E_{22}^{CNT}} + \frac{V_m(z)}{E^m} \tag{3}$$

$$\frac{\eta_3}{G_{12}(z)} = \frac{V_{CNT}(z)}{G_{12}^{CNT}} + \frac{V_m(z)}{G^m} \tag{4}$$

$$\nu_{12}(z) = V_{CNT}(z)\nu_{12}^{CNT} + V_m(z)\nu^m \tag{5}$$

$$\rho(z) = V_{CNT}(z)\rho^{CNT} + V_m(z)\rho^m \tag{6}$$

$$V_m(z) = 1 - V_{CNT}(z) \tag{7}$$

$E_{11}, E_{22}, G_{12}, G_{13}, G_{23}$ elasticity and shear modulus of composite material depending on CNT and matrix;$E_{11}^{CNT}, E_{22}^{CNT}, G_{12}^{CNT}, E^m, G^m$ values of CNT and the elasticity and shear modulus of the matrix; η_1, η_2, η_3 values efficiency parameters, ν_{12} value is the Poisson ratio of the composite; ν_{12}^{CNT} ve ν^{m} values are Poisson ratios of CNT and matrix, $\rho^{\mathrm{CNT}}, \rho^{\mathrm{m}}$ mass densities of CNT and matrix.

1.6. General Strain-Displacement Relations

The following equations represent the linear strain-displacement relations of the beam:

$$\varepsilon_{ii} = \frac{\partial u_i}{\partial x_i} \tag{8}$$

$$\varepsilon_{ij} = \frac{\partial u_i}{\partial z_j} + \frac{\partial w_j}{\partial x_i} \quad (i \neq j) \tag{9}$$

1.7. Elastic Constitutive Relations

Kinematic relations, along with the principles of mechanics and thermodynamics, possess universal applicability to any continuum, irrespective of its physical composition. However, specific equations are required to characterize the behavior of individual materials when subjected to external loads. These equations, known as constitutive equations, define the relationship between stress and strain within the material. Materials exhibiting a linear stress-strain relationship are classified as linear elastic materials. For such materials, the following equation is commonly employed (Reddy, 2003):

$$\sigma_i = Q_{ij}\varepsilon_i \tag{10}$$

where σ is the stress tensor, Q is the 2^{nd}-order stiffness tensor of material parameters, and ε is the strain tensor. To show this we express Eq. (10) in an alternate form using single subscript notation for stresses and strains and two subscript notations for the material stiffness coefficients:

$$\begin{gathered}\sigma_1 = \sigma_{11}, \sigma_2 = \sigma_{22}, \sigma_3 = \sigma_{33}, \sigma_4 = \tau_{23}, \sigma_5 = \tau_{13}, \sigma_6 = \tau_{12}, \varepsilon_1 = \varepsilon_{11}, \\ \varepsilon_2 = \varepsilon_{22}, \varepsilon_3 = \varepsilon_{33}, \varepsilon_4 = \gamma_{23} = 2\varepsilon_{23}, \varepsilon_5 = \gamma_{13} = 2\varepsilon_{13}, \varepsilon_6 = \gamma_{12} = 2\varepsilon_{12}\end{gathered} \tag{11}$$

The relation (10) is also known as generalized Hooke's law. The expression can be written explicitly as:

$$\begin{Bmatrix}\sigma_1\\ \sigma_2\\ \sigma_3\\ \sigma_4\\ \sigma_5\\ \sigma_6\end{Bmatrix} = \begin{bmatrix} Q_{11} & Q_{12} & Q_{13} & Q_{14} & Q_{15} & Q_{16}\\ Q_{21} & Q_{22} & Q_{23} & Q_{24} & Q_{25} & Q_{26}\\ Q_{31} & Q_{32} & Q_{33} & Q_{34} & Q_{35} & Q_{36}\\ Q_{41} & Q_{42} & Q_{43} & Q_{44} & Q_{45} & Q_{46}\\ Q_{51} & Q_{52} & Q_{53} & Q_{54} & Q_{55} & Q_{56}\\ Q_{61} & Q_{62} & Q_{63} & Q_{64} & Q_{65} & Q_{66}\end{bmatrix} \begin{Bmatrix}\varepsilon_1\\ \varepsilon_2\\ \varepsilon_3\\ \varepsilon_4\\ \varepsilon_5\\ \varepsilon_6\end{Bmatrix} \tag{12}$$

Now the coefficients Q_{ij} must be symmetric, i.e. $Q_{ij} = Q_{ji}$ (i, j=1, 2,...,6) due to the assumption of hyper elastic material behavior.. Therefore, there are 21(6+5+4+3+2+1) independent stiffness coefficients associated with the most general elastic material.

1.7.1. Material Symmetry

If, at a given point, the elastic material parameters remain unchanged for any two coordinate systems that are mirror images across a specific plane, then that plane is defined as a material plane of symmetry.

The presence of a single plane of symmetry in the elastic coefficients at a point, such that their values are identical for mirrored coordinate systems, defines a monoclinic material. To illustrate this concept, two coordinate systems are considered: (x_1, x_2, x_3) and (x'_1, x'_2, x'_3) with the x_1, x_2-plane parallel to the plane of symmetry. The x'_3 $-$axis is chosen such that x'_3 = -x_3 (the specific orientation of the left-handed coordinate system is not relevant to the discussion). This configuration ensures that one coordinate system is a mirror image of the other across the plane of symmetry. In such cases, the number of independent elastic constants reduces to 13, and the material coefficient matrix **Q** takes the following form:

$$Q = \begin{bmatrix} Q_{11} & Q_{12} & Q_{13} & 0 & 0 & Q_{16} \\ Q_{12} & Q_{22} & Q_{23} & 0 & 0 & Q_{26} \\ Q_{13} & Q_{23} & Q_{33} & 0 & 0 & Q_{36} \\ 0 & 0 & 0 & Q_{44} & Q_{45} & 0 \\ 0 & 0 & 0 & Q_{45} & Q_{55} & 0 \\ Q_{16} & Q_{26} & Q_{36} & 0 & 0 & Q_{66} \end{bmatrix} \tag{13}$$

Orthotropic materials, possessing three mutually orthogonal axes of symmetry, the number of independent elastic constants is reduced to nine. The stress strain relations for an orthotropic material take the form.

$$\begin{Bmatrix} \sigma_1 \\ \sigma_2 \\ \sigma_3 \\ \sigma_4 \\ \sigma_5 \\ \sigma_6 \end{Bmatrix} = \begin{bmatrix} Q_{11} & Q_{12} & Q_{13} & 0 & 0 & 0 \\ Q_{12} & Q_{22} & Q_{23} & 0 & 0 & 0 \\ Q_{13} & Q_{23} & Q_{33} & 0 & 0 & 0 \\ 0 & 0 & 0 & Q_{44} & 0 & 0 \\ 0 & 0 & 0 & 0 & Q_{55} & 0 \\ Q_{16} & Q_{26} & Q_{36} & 0 & 0 & Q_{66} \end{bmatrix} \begin{Bmatrix} \varepsilon_1 \\ \varepsilon_2 \\ \varepsilon_3 \\ \varepsilon_4 \\ \varepsilon_5 \\ \varepsilon_6 \end{Bmatrix} \tag{14}$$

Here elastic constants Q_{ij},in terms of modulus of elasticity E_i,shear modulus G_{ij}, and Poisson ratio ν_{ij} (i, j=1,2,3) are defined as follows.

$$Q_{11} = \frac{1 - \nu_{23}\nu_{32}}{E_2 E_3 \Delta}, Q_{12} = \frac{\nu_{21} + \nu_{23}\nu_{31}}{E_2 E_3 \Delta} = \frac{\nu_{12} + \nu_{32}\nu_{13}}{E_1 E_3 \Delta} \quad (15a,b)$$

$$Q_{13} = \frac{\nu_{31} + \nu_{21}\nu_{32}}{E_2 E_3 \Delta} = \frac{\nu_{13} + \nu_{12}\nu_{23}}{E_1 E_2 \Delta} \quad (16)$$

$$Q_{22} = \frac{1 - \nu_{13}\nu_{31}}{E_1 E_3 \Delta}, Q_{23} = \frac{\nu_{33} + \nu_{21}\nu_{31}}{E_1 E_3 \Delta} = \frac{\nu_{23} + \nu_{21}\nu_{13}}{E_1 E_3 \Delta} \quad (17a,b)$$

$$Q_{33} = \frac{1 - \nu_{12}\nu_{21}}{E_1 E_2 \Delta}, Q_{44} = G_{23} \;\; Q_{55} = G_{31} \;\; Q_{66} = G_{12} \quad (18a\text{-}d)$$

$$\Delta = \frac{1 - \nu_{12}\nu_{21} - \nu_{23}\nu_{32} - \nu_{31}\nu_{13} - 2\nu_{21}\nu_{32}\nu_{13}}{E_1 E_2 E_3} \quad (19)$$

In the expressions (15-19), E_i (i= 1, 2,3) represents the elastic moduli in the 1, 2, and 3 directions, respectively, ν_{ij} and G_{ij} (i, j= 1, 2,3) represent the Poisson's ratios and shear moduli in the 2-3, 1-3, and 1-2 planes, respectively. In addition, the following relation is valid for orthotropic materials.

$$\frac{\nu_{ij}}{E_i} = \frac{\nu_{ji}}{E_j} \; (no\ sum\ on\ i, j) \quad (20)$$

for i,j = 1,2,3.

The 9 independent material coefficients for an orthotropic material are E_1, E_2, E_3, G_{23}, G_{13}, $G_{12}, \nu_{12}, \nu_{13}, \nu_{23}$. In the absence of preferred directions, a material exhibits an infinite number of material symmetry planes. Such materials, known as isotropic, can be described using just two independent elastic coefficients. This leads to $E_1 = E_2 = E_3 = E, G_{12} = G_{13} = G_{23} = G,\ \nu_{12} = \nu_{13} = \nu_{23} = \nu$.

Non-zero elastic constants $C_{ij}$for isotropic material

$$Q_{11} = Q_{22} = Q_{33} = \lambda + 2\mu,\ Q_{12} = Q_{13} = Q_{23} = \lambda,\ Q_{44} = Q_{55} = Q_{66} = \mu$$

is in the form. Here the Láme constants λ and μ are defined as follows:

$$\lambda = \frac{E}{(1+\nu)(1-2\nu)}, \;\; \mu = G = \frac{E}{2(1+\nu)} \quad (21a,b)$$

1.7.2. Coordinate Transformations

Constitutive relations are expressed in terms of stress and strain components within the principal material coordinate system. However, this system typically does not coincide with the coordinate system used for problem formulation. This case, the expressions given for local coordinates need to be transformed into global coordinates. For (x_1, x_2, x_3) local coordinates and (x,y,z) global coordinates, the following relations can be used to transform expressions between these two systems with the help of Figure 5 (Reddy, 2003):

$$\begin{Bmatrix} x_1 \\ x_2 \\ x_3 \end{Bmatrix} = \begin{bmatrix} cos\,\theta & -sin\,\theta & 0 \\ sin\,\theta & cos\,\theta & 0 \\ 0 & 0 & 1 \end{bmatrix} \begin{Bmatrix} x \\ y \\ z \end{Bmatrix} = [B] \begin{Bmatrix} x \\ y \\ z \end{Bmatrix} \tag{22}$$

relation is available. From this expression

$$\begin{Bmatrix} x \\ y \\ z \end{Bmatrix} = \begin{bmatrix} cos\,\theta & -sin\,\theta & 0 \\ sin\,\theta & cos\,\theta & 0 \\ 0 & 0 & 1 \end{bmatrix} \begin{Bmatrix} x_1 \\ x_2 \\ x_3 \end{Bmatrix} = [B]^T \begin{Bmatrix} x_1 \\ x_2 \\ x_3 \end{Bmatrix} \tag{23}$$

is obtained. Here $\boldsymbol{B^{-1}} = \boldsymbol{B^T}$ and θ is the angle made counterclockwise with the x axis in the x-y plane.

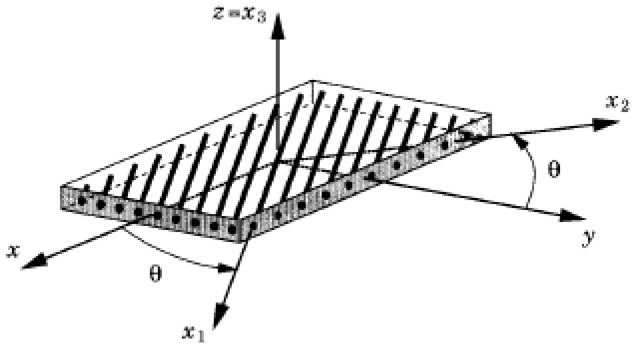

Figure 5. A lamina with material and problem coordinate systems (Reddy, 2003)

Considering the coordinate transformation relations given by equations (22) and (23), the relationship between the stress components can be expressed in matrix forms. Initially, 3x3 arrays are introduced to represent the stress components within each coordinate system.

$$[\sigma]_p = \begin{bmatrix} \sigma_{xx} & \sigma_{xy} & \sigma_{xz} \\ \sigma_{xy} & \sigma_{yy} & \sigma_{yz} \\ \sigma_{xz} & \sigma_{yz} & \sigma_{zz} \end{bmatrix},\ [\sigma]_c = \begin{bmatrix} \sigma_{11} & \sigma_{12} & \sigma_{13} \\ \sigma_{12} & \sigma_{22} & \sigma_{23} \\ \sigma_{13} & \sigma_{23} & \sigma_{33} \end{bmatrix} \tag{24}$$

Then (24) can be expressed in matrix form as

$$[\sigma]_p = [B]^t[\sigma]_c[B] \tag{25}$$

$$[\sigma]_c = [B][\sigma]_p\ [B]^t \tag{26}$$

Carrying out the matrix multiplications in (25), with [B] defined by (22), and rearranging the equations in terms of the single-subscript stress components in (x, y, z) and (x_1, x_2, x_3) coordinate systems, we obtain

$$\begin{Bmatrix} \sigma_{xx} \\ \sigma_{yy} \\ \sigma_{zz} \\ \sigma_{yz} \\ \sigma_{xz} \\ \sigma_{xy} \end{Bmatrix} = \begin{bmatrix} c^2 & s^2 & 0 & 0 & 0 & -2cs \\ s^2 & c^2 & 0 & 0 & 0 & 2cs \\ 0 & 0 & 1 & 0 & 0 & 0 \\ 0 & 0 & 0 & c & s & 0 \\ 0 & 0 & 0 & -s & c & 0 \\ sc & -sc & 0 & 0 & 0 & c^2 - s^2 \end{bmatrix} \begin{Bmatrix} \sigma_1 \\ \sigma_2 \\ \sigma_3 \\ \sigma_4 \\ \sigma_5 \\ \sigma_6 \end{Bmatrix} \tag{27}$$

or

$$[\sigma]_p = [T]\ [\sigma]_c \tag{28}$$

The inverse relationship between $\{\sigma\}_c$and $\{\sigma\}_p$, Eq. (26), is given by

$$\begin{Bmatrix} \sigma_1 \\ \sigma_2 \\ \sigma_3 \\ \sigma_4 \\ \sigma_5 \\ \sigma_6 \end{Bmatrix} = \begin{bmatrix} c^2 & s^2 & 0 & 0 & 0 & 2cs \\ s^2 & c^2 & 0 & 0 & 0 & -2cs \\ 0 & 0 & 1 & 0 & 0 & 0 \\ 0 & 0 & 0 & c & -s & 0 \\ 0 & 0 & 0 & s & c & 0 \\ -sc & sc & 0 & 0 & 0 & c^2 - s^2 \end{bmatrix} \begin{Bmatrix} \sigma_{xx} \\ \sigma_{yy} \\ \sigma_{zz} \\ \sigma_{yz} \\ \sigma_{xz} \\ \sigma_{xy} \end{Bmatrix} \tag{29}$$

or

$$[\sigma]_c = [R]\ [\sigma]_p \tag{30}$$

equations are obtained. Here, it is defined as c=$cos\ \theta$ and s=$sin\ \theta$

Strain components

$$[\varepsilon]_p = [L]^t[\varepsilon]_c[L] \tag{31}$$

$$[\varepsilon]_c = [L][\varepsilon]_p\ [L]^t \tag{32}$$

is in the form. Here ε_c and ε_p are the strain tensors in local and global coordinates.

$$\begin{Bmatrix} \varepsilon_{xx} \\ \varepsilon_{yy} \\ \varepsilon_{zz} \\ \varepsilon_{yz} \\ \varepsilon_{xz} \\ \varepsilon_{xy} \end{Bmatrix} = \begin{bmatrix} c^2 & s^2 & 0 & 0 & 0 & -cs \\ s^2 & c^2 & 0 & 0 & 0 & cs \\ 0 & 0 & 1 & 0 & 0 & 0 \\ 0 & 0 & 0 & c & s & 0 \\ 0 & 0 & 0 & -s & c & 0 \\ 2sc & -2sc & 0 & 0 & 0 & c^2 - s^2 \end{bmatrix} \begin{Bmatrix} \varepsilon_1 \\ \varepsilon_2 \\ \varepsilon_3 \\ \varepsilon_4 \\ \varepsilon_5 \\ \varepsilon_6 \end{Bmatrix} \tag{33}$$

And

$$\begin{Bmatrix} \varepsilon_1 \\ \varepsilon_2 \\ \varepsilon_3 \\ \varepsilon_4 \\ \varepsilon_5 \\ \varepsilon_6 \end{Bmatrix} = \begin{bmatrix} c^2 & s^2 & 0 & 0 & 0 & cs \\ s^2 & c^2 & 0 & 0 & 0 & -cs \\ 0 & 0 & 1 & 0 & 0 & 0 \\ 0 & 0 & 0 & c & -s & 0 \\ 0 & 0 & 0 & s & c & 0 \\ -2sc & 2sc & 0 & 0 & 0 & c^2 - s^2 \end{bmatrix} \begin{Bmatrix} \varepsilon_{xx} \\ \varepsilon_{yy} \\ \varepsilon_{zz} \\ 2\varepsilon_{yz} \\ 2\varepsilon_{xz} \\ 2\varepsilon_{xy} \end{Bmatrix} \tag{34}$$

(33) and (34) can be rewritten.

$$[\varepsilon]_p = [R]^T \{\varepsilon\}_c \tag{35}$$

$$[\varepsilon]_c = [T]^T \{\varepsilon\}_p \tag{36}$$

as short form. Using (10), (28), (30), (35), and (36) equations

$$[\sigma]_p = [T][\sigma]_c = [T][Q]_c\{\varepsilon\}_c = [T][Q]_c[T]^T \{\varepsilon\}_p = [Q]_p\{\varepsilon\}_p \tag{37}$$

equality is obtained. Here, $\boldsymbol{Q_c}$ is the matrix of elastic constants in the 6x6 material coordinates defined in the expression (14). **T** is the transformation matrix defined in (28) and (30).

Hooke's law in global coordinates expressed as:

$$[\sigma]_p = [Q]_p\{\varepsilon\}_p \tag{38}$$

In the expressions (37) and (38) $Q_p = \bar{Q}$ and $Q_c = Q$, the following expression can be written as

$$[\bar{Q}] = [T][Q][T]^T \tag{39}$$

Equation (39) is valid for general constitutive matrix [Q] (i.e., for orthotropic as well as anisotropic).

Carrying out the matrix multiplications in (39) for the general anisotropic case, we obtain

$$\begin{bmatrix} \bar{Q}_{11} \\ \bar{Q}_{12} \\ \bar{Q}_{22} \\ \bar{Q}_{16} \\ \bar{Q}_{26} \\ \bar{Q}_{66} \end{bmatrix} = \begin{bmatrix} c^4 & 2c^2s^2 & s^4 & 4c^2s^2 \\ c^2s^2 & c^4+s^4 & c^2s^2 & -4c^2s^2 \\ s^4 & 2c^2s^2 & c^4 & 4c^2s^2 \\ c^3s & cs^3-c^3s & -cs^3 & -2cs(c^2-s^2) \\ cs^3 & c^3s-cs^3 & -c^3s & 2cs(c^2-s^2) \\ c^2s^2 & -2c^2s^2 & c^2s^2 & (c^2-s^2)^2 \end{bmatrix} \begin{bmatrix} Q_{11} \\ Q_{12} \\ Q_{22} \\ Q_{66} \end{bmatrix} \tag{40}$$

For orthotropic and transversely isotropic materials, if the material coordinates do not coincide with the global coordinates, the constitutive equation is given by:

$$\begin{Bmatrix} \sigma_{xx} \\ \sigma_{yy} \\ \sigma_{yz} \\ \sigma_{xz} \\ \sigma_{xy} \end{Bmatrix} = \begin{bmatrix} \bar{Q}_{11} & \bar{Q}_{12} & 0 & 0 & \bar{Q}_{16} \\ \bar{Q}_{12} & \bar{Q}_{22} & 0 & 0 & \bar{Q}_{26} \\ 0 & 0 & \bar{Q}_{44} & \bar{Q}_{45} & 0 \\ 0 & 0 & \bar{Q}_{45} & \bar{Q}_{55} & 0 \\ \bar{Q}_{16} & \bar{Q}_{26} & 0 & 0 & \bar{Q}_{66} \end{bmatrix} \begin{Bmatrix} \varepsilon_{xx} \\ \varepsilon_{yy} \\ \varepsilon_{yz} \\ \varepsilon_{xz} \\ \varepsilon_{xy} \end{Bmatrix} \tag{41}$$

It is important to note that the shape will be similar to that of the monoclinic material. No strain in the Y direction was assumed, and the equations given in [$\sigma_{yy} = \sigma_{yz} = \sigma_{yy} = \varepsilon_{yz} = \varepsilon_{xy} = 0$ ve $\varepsilon_{yy} \neq 0$] were derived under plane strain assumptions (Reddy, 2003).

$$\begin{Bmatrix} \sigma_{xx} \\ \sigma_{xz} \end{Bmatrix} = \begin{bmatrix} \tilde{Q}_{11} & 0 \\ 0 & \tilde{Q}_{55} \end{bmatrix} \begin{Bmatrix} \varepsilon_{xx} \\ \varepsilon_{xz} \end{Bmatrix} \tag{42}$$

$$\tilde{Q}_{11} = \bar{Q}_{11} - \frac{(\bar{Q}_{12})^2}{\bar{Q}_{22}}, \tilde{Q}_{55} = \bar{Q}_{55} \tag{43}$$

$$\sigma_{xx} = \tilde{Q}_{11}\varepsilon_{xx} \text{ and } \sigma_{xz} = \tilde{Q}_{55}\varepsilon_{xz} \tag{44}$$

1.8. Langrange Formulation

Potential energy of the one beam member along x axis,

$$\mathrm{U} = \frac{1}{2}\int_0^{L_e} \int_{\mathrm{A}} (\sigma_{xx}\varepsilon_{xx} + \sigma_{xz}\varepsilon_{xz})\, \mathrm{dA\, dx} \tag{45}$$

Where, L_e, and A are the one beam member length and cross-sectional area (yz plane) of the beam. The kinetic energy for the beam as follows.

$$\mathrm{T} = \frac{1}{2}\int_{0}^{L_e} \int_{\mathrm{A}} \rho(\dot{u}^2 + \dot{w}^2)\,\mathrm{dA}\,\mathrm{dx} \tag{46}$$

Here ρ is the mass density. The upper dot represents the derivative with respect to time. Work done by the vertical (in y direction) q_0 distributed load acting on the beam along the axis (x).

$$\mathrm{V} = -\int_{0}^{\mathrm{L_e}} q_0 \mathrm{w}\,\mathrm{dx} \tag{47}$$

Work done by the axial force N_{cr} is represented by the formula.

$$R_p = \int_0^{L_e} N_{cr} \left(\frac{\partial w_0}{\partial x}\right)^2 dx \tag{48}$$

Obtained with the help of Lagrange equation and q and $\dot{q}_i$ represent the unknown displacement and velocity components. It can be defined as

$$\mathrm{L}=\mathrm{T}-(\mathrm{U}+\mathrm{V}+R_p) \tag{49}$$

Lagrange equation is expressed as

$$\frac{d}{dt}\left(\frac{\partial L}{\partial \dot{q}_i}\right) - \frac{\partial L}{\partial q_i} = 0 \tag{50}$$

In the expression, **T** indicates kinetic energy, **U** is deformation energy and **V** is the work done by the external load.

2. RESEARCH METHODOLOGY AND IMPLICATONS

2.1. Problem Definition and Formulation

The geometric properties and coordinate system of the beam are depicted in Figure 6. It is assumed that there is no displacement in the y-direction. The beam under a uniform load (q_0) on top and axial forces (N_{cr}) at both ends. Its total length and height are Lt and h, respectively.

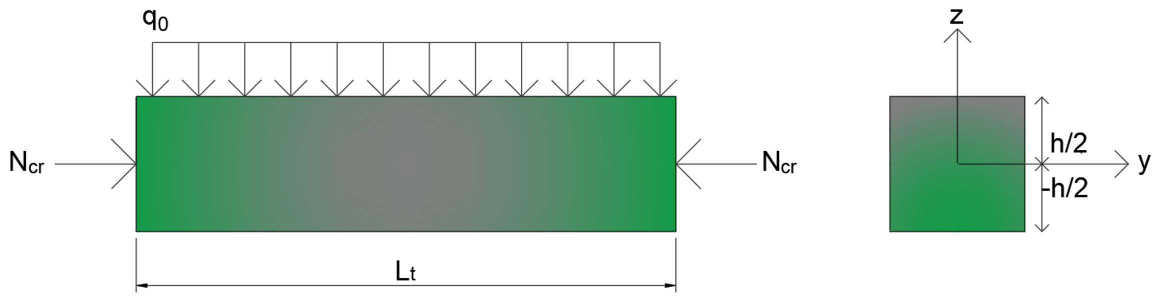

Figure 6. Geometric properties and coordinate system of the beam

The distributions of V_{CNT} are shown in Figure 4 and provided in their expanded form below.
For UD-CNT:

$$V_{CNT}(z) = V_{tcnt} \quad \left(\frac{-h}{2} \leq z \leq \frac{h}{2}\right) \tag{51}$$

For FGA-CNT:

$$V_{CNT}(z) = \left(1 - \frac{2z}{h}\right) V_{tcnt} \quad \left(\frac{-h}{2} \leq z \leq \frac{h}{2}\right) \tag{52}$$

For FGO-CNT:

$$V_{CNT}(z) = 2\left(1 - \frac{2|z|}{h}\right) V_{tcnt} \quad \left(\frac{-h}{2} \leq z \leq \frac{h}{2}\right) \tag{53}$$

For FGX-CNT

$$V_{CNT}(z) = \frac{4|z|}{h} V_{tcnt} \quad \left(\frac{-h}{2} \leq z \leq \frac{h}{2}\right) \tag{54}$$

The V_{cnt} and V_{tcnt} values are the volume fraction of the CNT and the total volume fraction, respectively.

2.2. Finite Element Formulation

The finite element method serves as a critical tool in engineering analysis and design for addressing physical problems involving real structures or components subjected to various loads. To facilitate mathematical representation, simplifying assumptions are often introduced, leading to a set of governing differential equations that constitute the mathematical model. Finite element analysis aims to solve this model numerically. However, due to the inherent nature of numerical solutions, an assessment of solution accuracy is crucial. If the established accuracy criteria are not met, refinement of the finite element solution, often involving adjustments to parameters such as mesh density, becomes necessary until an acceptable level of accuracy is attained (K.J. Bathe,2019).

It is important to recognize that the finite element solution pertains solely to the chosen mathematical model. Consequently, any assumptions inherent in the model will be reflected in the predicted response. The predictive capability for physical phenomena is therefore limited by the information encompassed within the mathematical model. This underscores the critical role of selecting an appropriate mathematical model, as it directly determines the level of insight gleaned from the analysis of the actual physical problem (K.J. Bathe,2019).

In finite element analysis, elements are characterized by a specific number of nodes. Each node within an element is associated with a degree of freedom, representing either a translation or a rotation. In the analysis conducted, for one beam element was shown using three nodes, resulting in a total of twelve degrees of freedom (Figure 7).

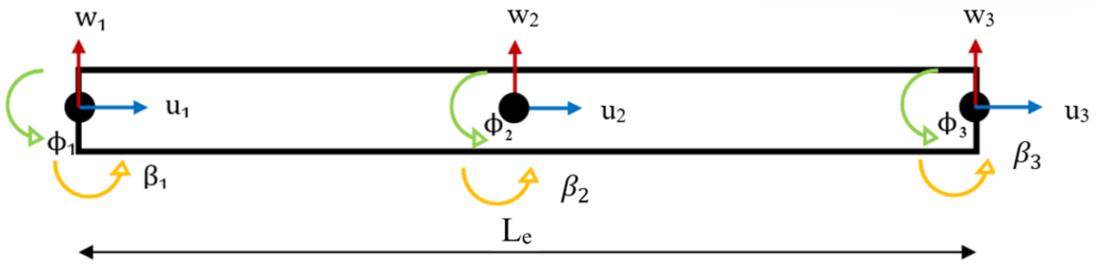

Figure 7. Finite Element Model

The variables u_1, u_2 *and* u_3 represent the axial displacements at each node along the length of the beam. w_1, w_2 *and* w_3 represent the vertical displacements at each node perpendicular to the length of the beam. $\beta_1, \beta_2, \beta_3$ represent the rotations of the cross-section at each node, indicating that the cross-section does not necessarily remain perpendicular to the beam's axis after shear deformation. $\phi_1, \phi_2, and\ \phi_3$ represent the higher-order rotations of the cross-section at each node. These rotations are dependent on the vertical displacements (w).

2.2.1. Shape Functions

For three degrees of freedom, we can use a square polynomial in x having three adjustable parameters, to define the displacement function u(x) as given below:

$$u(x) = \alpha_1 + \alpha_2 x + \alpha_3 x^2 \tag{55}$$

Here the parameters $\alpha_1, \alpha_2\ and\ \alpha_3$ are called "generalized coordinates" which can be expressed in terms of the three nodal displacements. In finite element method, the equations are based on nodal displacements; it is necessary to express u(x) in terms of u_1 u_2, and u_3 instead of α_1, α_2,and α_3. Thus, substituting $u(x = 0) = u_1, u(x = L\ /\ 2) = u_2$, $u(x = L) = u_3$ following equations can be obtained.

$$\alpha_1 = u_1 \tag{56}$$

$$u_2 = \alpha_1 \frac{L}{2} + \alpha_2 + \frac{L^2}{4}\alpha_3 \tag{57}$$

$$u_3 = \alpha_1 + L\alpha_2 + L^2\alpha_3 = u_3 \tag{58}$$

Therefore, solving Eqs. (56-58) in terms of $u_1, u_2\ and\ u_3$. α_1, α_2,and α_3 can be expressed as given below.

$$\alpha_1 = u_1,\ \alpha_2 = \frac{1}{2}(4u_2 - 3u_1 - u_3),\ \alpha_3 = \frac{2}{L^2}(u_1 - 2u_2 + u_3) \tag{59}$$

And substituting α parameters in the displacement function and rewriting u(x),

$$u(x) = N_1 u_1 + N_2 u_2 + N_3 u_3 \tag{60}$$

where

$$N_1 = \left(1 - \frac{3x}{L} + \frac{2x^2}{L^2}\right), N_2 = 4\left(\frac{x}{L} - \frac{x^2}{L^2}\right), N_3 = (-\frac{x}{L} + \frac{2x^2}{L^2}) \tag{61}$$

are the shape functions for the element. For β, a comparable procedure can be employed to derive the same shape function.

If we use displacement equation v(x) for w displacement and $\phi = \partial w/\partial x$ rotation, the shape functions formulation goes like:

$$v(x) = \alpha_1 + \alpha_2 x + \alpha_3 x^2 + \alpha_n x^3 + \alpha_5 x^4 + \alpha_6 x^5 \tag{62}$$

Then, if we make the necessary arrangements for the w displacement:

$$w_1 = v(x = 0) \rightarrow w_1 = \alpha_1 \tag{63}$$

$$w_2 = v(x = L\,/\,2) \rightarrow w_2 = \alpha_1 + \alpha_2 \frac{L}{2} + \frac{L^2}{4}\alpha_3 \frac{+L^3}{8}\alpha_n + \frac{L^4}{16}\alpha_5 + \alpha_6 \frac{L^5}{32} \tag{64}$$

$$w_3 = v(x) = L \rightarrow w_3 = \alpha_1 + \alpha_2 L + \alpha_3 L^2 + \alpha_4 L^3 + \alpha_5 L^4 + \alpha_6 L^5 \tag{65}$$

To calculate the displacements corresponding to the ϕ rotations, the derivative of the displacement equation is taken.

$$v'(x) = \alpha_2 + 2\alpha_3 x + 3\alpha_n x^2 + 4\alpha_5 x^3 + 5\alpha_6 x^4 \tag{66}$$

Then

$$\phi_1 = \left(v'(x = 0)\right) \rightarrow \phi_1 = \alpha_2 \tag{67}$$

$$\phi_2 = \left(v'(x = L\,/\,2)\right) \rightarrow \phi_2 = \alpha_2 + L\alpha_3 + \frac{3L^2}{4}\alpha_4 \frac{+L^3}{8}\alpha_n + \frac{L^3}{2}\alpha_5 + \frac{5L^4}{16}\alpha_6 \tag{68}$$

$$\phi_3 = (v'(x) = L) \rightarrow \phi_3 = \alpha_2 + 2\alpha_3 L + 3\alpha_4 L^2 + 4\alpha_5 L^3 + 5\alpha_6 L^4 \tag{69}$$

And substituting α parameters in the displacement function and rewriting v(x),

$$v(x) = M_1 w_1 + M_2 w_2 + M_3 w_3 + M_4 \phi_1 + M_5 \phi_2 + M_6 \phi_3 \tag{70}$$

where

$$M_1 = 1 + 24\frac{x^5}{L^5} - 68\frac{x^4}{L^4} - 23\frac{x^2}{L^2} + 66\frac{x^3}{L^3} \tag{71}$$

$$M_2 = 16\frac{x^4}{L^4} - 32\frac{x^3}{L^3} + 16\frac{x^2}{L^2} \tag{72}$$

$$M_3 = 7\frac{x^2}{L^2} - 34\frac{x^3}{L^3} + 52\frac{x^4}{L^4} - 24\frac{x^5}{L^5} \tag{73}$$

$$M_4 = x - 6\frac{x^2}{L} + 13\frac{x^3}{L^2} - 12\frac{x^4}{L^3} + 4\frac{x^5}{L^4} \tag{74}$$

$$M_5 = 32\frac{x^3}{L^2} - 8\frac{x^2}{L} - 40\frac{x^4}{L^3} + 16\frac{x^5}{L^4} \tag{75}$$

$$M_6 = 5\frac{x^3}{L^2} - \frac{x^2}{L} - 8\frac{x^4}{L^3} + 4\frac{x^5}{L^4} \tag{76}$$

are the shape functions for the element.

2.3. Displacement Field

The nodal displacements for the finite element model are presented below.

$$u_0 = N_1u_1 + N_2u_2 + N_3u_3 \tag{77}$$

$$w_0 = M_1w_1 + M_2w_2 + M_3w_3 + M_4\phi_1 + M_5\phi_2 + M_6\phi_3 \tag{78}$$

$$\beta_0 = N_1\beta_1 + N_2\beta_2 + N_3\beta_3 \tag{79}$$

$$\phi_0 = \frac{\partial w_0}{\partial x} \tag{80}$$

Here, u and w stand for displacement components in the y and z directions, respectively, at any point of the beam. u_0 and w_0 are the displacements along the x and z directions in the midplane of the beam and β_0, ϕ_0 correspond to the rotations of the section.

$$u = u_0(x) - z\phi(x) + f(z)\beta(x) \tag{81}$$

$$w = w_0(x) \tag{82}$$

In addition, f(z) is a shear function defined to reflect the distortion in the cross section and Reddy's (Reddy, 2003) shear function is used in this study.

$$f(z) = z - \frac{4z^3}{3h^2} \tag{83}$$

2.4. Strain-Displacement Relations

Upon substituting the derived expressions for u and w into equations 8 and 9, the resulting equations take the following form.

$$\varepsilon_{xx} = \frac{\partial u_0}{\partial x} - z\frac{\partial \phi_x}{\partial x} + f(z)\frac{\partial \beta_x}{\partial x} \tag{84}$$

$$\varepsilon_{xz} = -\phi(x) + f(z)\beta_x + \frac{\partial w_0}{\partial x} \tag{85}$$

2.5. Energy Formulation

The potential energy and kinetic energy expressions for a one beam element length (L_e) are obtained as follows by substituting the expressions (42), (81), (82), (84), and (85) into equations (45) and (46) for each material state considered:

$$\begin{aligned} U = \frac{1}{2}\int_0^{Le} & A_0\left(\frac{\partial u_0}{\partial x}\right)^2 - 2A_{11}\left(\frac{\partial u}{\partial x}\frac{\partial \phi}{\partial x}\right) + A_{12}\left(\frac{\partial \phi}{\partial x}\right)^2 + 2A_{11}f(z)\left(\frac{\partial \phi}{\partial x}\frac{\partial \beta}{\partial x}\right) \\ & + \big(f(z)\big)^2\left(\frac{\partial \beta}{0x}\right)^2 \\ & + B_0\left(\left(1-4\frac{z^2}{h^2}\right)B^2 + \phi^2 + \left(\frac{\partial w_0}{\partial x}\right)^2 - 2\left(1-\frac{4t^2}{h^2}\right)\beta\phi \right. \\ & \left. + 2\left(1-\frac{4z^2}{h^2}\right)\beta\frac{\partial w_0}{\partial x} - 2\phi\frac{\partial w_0}{\partial x}\right) \end{aligned} \tag{86}$$

$$\begin{aligned} T = \frac{1}{2}\int_0^{Le} & A_0\left(\frac{\partial u_0}{\partial t}\right)^2 - 2A_{11}\left(\frac{\partial u}{\partial t}\frac{\partial \phi}{\partial t}\right) + A_{12}\left(\frac{\partial \phi}{\partial t}\right)^2 + 2A_{11}f(z)\left(\frac{\partial \phi}{\partial t}\frac{\partial \beta}{\partial t}\right) \\ & + \big(f(z)\big)^2\left(\frac{\partial \beta}{\partial t}\right)^2 \\ & + B_0\left(\left(1-4\frac{z^2}{h^2}\right)B^2 + \phi^2 + \left(\frac{\partial w_0}{\partial t}\right)^2 - 2\left(1-\frac{4t^2}{h^2}\right)\beta\phi \right. \\ & \left. + 2\left(1-\frac{4z^2}{h^2}\right)\beta\frac{\partial w_0}{\partial t} - 2\phi\frac{\partial w_0}{\partial t}\right) \end{aligned} \tag{87}$$

Here A_0, A_{11}, A_{12} and B_0 expressions can be given as

$$[A_0, A_{11}, A_{12}] = \int_A \widetilde{Q}_{11}(1, z, z^2)\, dA \qquad [B_0] = \int_A \widetilde{Q}_{55}\, dA \tag{88}$$

The general-purpose equation of motion can be formulated by substituting the necessary equations into Eq. (50),

$$M\ddot{u} + (K - N_{cr}K_G)u = F \tag{89}$$

where M is the element mass matrix, K is the element stiffness matrix, K_G is the geometric stiffness matrix, F is the force matrix. For a beam of length L, the equation of motion of the system is obtained by the finite element method as follows.
For free vibration analysis, if $K_G = 0$ and F=0 and $u = u_0 e^{i\omega t}$ are taken in Eq. (89), the free vibration equation obtain as follows.

$$(K - \omega^2 M)u = 0 \tag{90}$$

For buckling analysis, if M=F=0 is taken in Eq. (89), the buckling equation is obtained

$$(K - N_{cr}K_G)u = 0 \tag{91}$$

For bending analysis, if M=0 is taken in Eq. (89), the bending equation obtain as follows

$$Ku = F \tag{92}$$

2.5.1. Stiffness Matrix for One Element

A beam element has three nodes and twelve degrees of freedom as shown below.

$$u = \{u_1 \quad u_2 \quad u_3 \quad w_1 \quad w_2 \quad w_3 \quad \phi_1 \quad \phi_2 \quad \phi_3 \quad \beta_1 \quad \beta_2 \quad \beta_3\} \tag{93}$$

The stiffness matrix for a single element within a finite element model is acquired by compiling the constants derived from the potential energy calculation. This matrix is 12x12 and is given below.

$$[K]=\begin{bmatrix} K_{11} & K_{12} & K_{13} & 0 & 0 & 0 & 0 & 0 & 0 & 0 & 0 & 0 \\ K_{21} & K_{22} & K_{23} & 0 & 0 & 0 & 0 & 0 & 0 & 0 & 0 & 0 \\ K_{31} & K_{32} & K_{33} & 0 & 0 & 0 & 0 & 0 & 0 & 0 & 0 & 0 \\ 0 & 0 & 0 & K_{44} & K_{45} & K_{46} & K_{47} & K_{48} & K_{49} & K_{410} & K_{411} & K_{412} \\ 0 & 0 & 0 & K_{54} & K_{55} & K_{56} & K_{57} & K_{58} & K_{59} & K_{510} & K_{511} & K_{512} \\ 0 & 0 & 0 & K_{64} & K_{65} & K_{66} & K_{67} & K_{68} & K_{69} & K_{610} & K_{611} & K_{612} \\ 0 & 0 & 0 & K_{74} & K_{75} & K_{76} & K_{77} & K_{78} & K_{79} & K_{710} & K_{711} & K_{712} \\ 0 & 0 & 0 & K_{84} & K_{85} & K_{86} & K_{87} & K_{88} & K_{89} & K_{810} & K_{811} & K_{812} \\ 0 & 0 & 0 & K_{94} & K_{95} & K_{96} & K_{97} & K_{98} & K_{99} & K_{910} & K_{911} & K_{912} \\ 0 & 0 & 0 & K_{104} & K_{105} & K_{106} & K_{107} & K_{108} & K_{109} & K_{1010} & K_{1011} & K_{1012} \\ 0 & 0 & 0 & K_{114} & K_{115} & K_{116} & K_{117} & K_{118} & K_{119} & K_{1110} & K_{1111} & K_{1112} \\ 0 & 0 & 0 & K_{124} & K_{125} & K_{126} & K_{127} & K_{128} & K_{129} & K_{1210} & K_{1211} & K_{1212} \end{bmatrix}$$

The matrix is symmetric about the diagonal, implying that $K_{ij} = K_{ji}$. The values are given. The values of the matrix elements are specified for the case when the $\theta = 0$.

$$\begin{aligned} K_{11} = -(7bh(&(E^m)^2V_{cnt} - (E^m)^2(V_{cnt})^2 + E_{22}^{CNT}E^m - 2E_{22}^{CNT}E^mV_{cnt} \\ &+ E_{22}^{CNT}E^m(V_{cnt})^2 - E_{11}^{CNT}E_{22}^{CNT}(V_{cnt})^2\eta_1 + E_{11}^{CNT}E^m(V_{cnt})^2\eta_1 \\ &- E_{22}^{CNT}E^m\eta_2(\upsilon^m)^2 + E_{11}^{CNT}E_{22}^{CNT}V_{cnt}\eta_1 \\ &+ 2E_{22}^{CNT}E^mV_{cnt}\eta_2(\upsilon^m)^2 - E_{22}^{CNT}E^m(V_{cnt})^2\eta_2(\upsilon_{12}^{CNT})^2 \\ &- E_{22}^{CNT}E^m(V_{cnt})^2\eta_2(\upsilon^m)^2 - 2E_{22}^{CNT}E^mV_{cnt}\eta_2\upsilon_{12}^{CNT}\upsilon^m \\ &+ 2E_{22}^{CNT}E^m(V_{cnt})^2\eta_2\upsilon_{12}^{CNT}\upsilon^m))/(L(E_{22}^{CNT} - E_{22}^{CNT}V_{cnt} \\ &+ E^mV_{cnt})((V_{cnt})^2(\upsilon_{12}^{CNT})^2 - 2(V_{cnt})^2\upsilon_{12}^{CNT}\upsilon^m + (V_{cnt})^2(\upsilon^m)^2 \\ &+ 2V_{cnt}\upsilon_{12}^{CNT}\upsilon^m - 2V_{cnt}(\upsilon^m)^2 + (\upsilon^m)^2 - 1)) \end{aligned} \tag{94}$$

$$\begin{aligned} K_{21} = (8bh(&(E^m)^2V_{cnt} - (E^m)^2(V_{cnt})^2 + E_{22}^{CNT}E^m - 2E_{22}^{CNT}E^mV_{cnt} \\ &+ E_{22}^{CNT}E^m(V_{cnt})^2 - E_{11}^{CNT}E_{22}^{CNT}(V_{cnt})^2\eta_1 + E_{11}^{CNT}E^m(V_{cnt})^2\eta_1 \\ &- E_{22}^{CNT}E^m\eta_2(\upsilon^m)^2 + E_{11}^{CNT}E_{22}^{CNT}V_{cnt}\eta_1 \\ &+ 2E_{22}^{CNT}E^mV_{cnt}\eta_2(\upsilon^m)^2 - E_{22}^{CNT}E^m(V_{cnt})^2\eta_2(\upsilon_{12}^{CNT})^2 \\ &- E_{22}^{CNT}E^m(V_{cnt})^2\eta_2(\upsilon^m)^2 - 2E_{22}^{CNT}E^mV_{cnt}\eta_2\upsilon_{12}^{CNT}\upsilon^m \\ &+ 2E_{22}^{CNT}E^m(V_{cnt})^2\eta_2\upsilon_{12}^{CN}\upsilon^m))/(L(E_{22}^{CNT} - E_{22}^{CNT}V_{cnt} \\ &+ E^mV_{cnt})((V_{cnt})^2(\upsilon_{12}^{CNT})^2 - 2(V_{cnt})^2\upsilon_{12}^{CNT}\upsilon^m + (V_{cnt})^2(\upsilon^m)^2 \\ &+ 2V_{cnt}\upsilon_{12}^{CNT}\upsilon^m - 2V_{cnt}(\upsilon^m)^2 + (\upsilon^m)^2 - 1)) \end{aligned} \tag{95}$$

$$\begin{aligned}K_{22} = -(16bh((E^m)^2V_{cnt} - (E^m)^2(V_{cnt})^2 + E_{22}^{CNT}E^m - 2E_{22}^{CNT}E^mV_{cnt} \\ + E_{22}^{CNT}E^m(V_{cnt})^2 - E_{11}^{CNT}E_{22}^{CNT}(V_{cnt})^2\eta_1 + E_{11}^{CNT}E^m(V_{cnt})^2\eta_1 \\ - E_{22}^{CNT}E^m\eta_2(\upsilon^m)^2 + E_{11}^{CNT}E_{22}^{CNT}V_{cnt}\eta_1 \\ + 2E_{22}^{CNT}E^mV_{cnt}\eta_2(\upsilon^m)^2 - E_{22}^{CNT}E^m(V_{cnt})^2\eta_2(\upsilon_{12}^{CNT})^2 \\ - E_{22}^{CNT}E^m(V_{cnt})^2\eta_2(\upsilon^m)^2 - 2E_{22}^{CNT}E^mV_{cnt}\eta_2\upsilon_{12}^{CNT}\upsilon^m \\ + 2E_{22}^{CNT}E^m(V_{cnt})^2\eta_2\upsilon_{12}^{CNT}\upsilon^m))/(L(E_{22}^{CNT} - E_{22}^{CNT}V_{cnt} \\ + E^mV_{cnt})((V_{cnt})^2(\upsilon_{12}^{CNT})^2 - 2(V_{cnt})^2\upsilon_{12}^{CNT}\upsilon^m + (V_{cnt})^2(\upsilon^m)^2 \\ + 2V_{cnt}\upsilon_{12}^{CNT}\upsilon^m - 2V_{cnt}(\upsilon^m)^2 + (\upsilon^m)^2 - 1))\end{aligned} \tag{96}$$

$$\begin{aligned}K_{31} = -(bh((E^m)^2V_{cnt} - (E^m)^2(V_{cnt})^2 + E_{22}^{CNT}E^m - 2E_{22}^{CNT}E^mV_{cnt} \\ + E_{22}^{CNT}E^m(V_{cnt})^2 - E_{11}^{CNT}E_{22}^{CNT}(V_{cnt})^2\eta_1 + E_{11}^{CNT}E^m(V_{cnt})^2\eta_1 \\ - E_{22}^{CNT}E^m\eta_2(\upsilon^m)^2 + E_{11}^{CNT}E_{22}^{CNT}V_{cnt}\eta_1 \\ + 2E_{22}^{CNT}E^mV_{cnt}\eta_2(\upsilon^m)^2 - E_{22}^{CNT}E^m(V_{cnt})^2\eta_2(\upsilon_{12}^{CNT})^2 \\ - E_{22}^{CNT}E^m(V_{cnt})^2\eta_2(\upsilon^m)^2 - 2E_{22}^{CNT}E^mV_{cnt}\eta_2\upsilon_{12}^{CNT}\upsilon^m \\ + 2E_{22}^{CNT}E^m(V_{cnt})^2\eta_2\upsilon_{12}^{CNT}\upsilon^m))/(L(E_{22}^{CNT} - E_{22}^{CNT}V_{cnt} \\ + E^mV_{cnt})((V_{cnt})^2(\upsilon_{12}^{CNT})^2 - 2(V_{cnt})^2\upsilon_{12}^{CNT}\upsilon^m + (V_{cnt})^2(\upsilon^m)^2 \\ + 2V_{cnt}\upsilon_{12}^{CNT}\upsilon^m - 2V_{cnt}(\upsilon^m)^2 + (\upsilon^m)^2 - 1))\end{aligned} \tag{97}$$

$$\begin{aligned}K_{44} = -(327bh^3((E^m)^2V_{cnt} - (E^m)^2(V_{cnt})^2 + E_{22}^{CNT}E^m - 2E_{22}^{CNT}E^mV_{cnt} \\ + E_{22}^{CNT}E^m(V_{cnt})^2 - E_{11}^{CNT}E_{22}^{CNT}(V_{cnt})^2\eta_1 + E_{11}^{CNT}E^m(V_{cnt})^2\eta_1 \\ - E_{22}^{CNT}E^m\eta_2(\upsilon^m)^2 + E_{11}^{CNT}E_{22}^{CNT}V_{cnt}\eta_1 \\ + 2E_{22}^{CNT}E^mV_{cnt}\eta_2(\upsilon^m)^2 - E_{22}^{CNT}E^m(V_{cnt})^2\eta_2(\upsilon_{12}^{CNT})^2 \\ - E_{22}^{CNT}E^m(V_{cnt})^2\eta_2(\upsilon^m)^2 - 2E_{22}^{CNT}E^mV_{cnt}\eta_2\upsilon_{12}^{CNT}\upsilon^m \\ + 2E_{22}^{CNT}E^m(V_{cnt})^2\eta_2\upsilon_{12}^{CNT}\upsilon_{12}^{CNT}\upsilon^m))/(L^3(E_{22}^{CNT} - E_{22}^{CNT}V_{cnt} \\ + E^mV_{cnt})((V_{cnt})^2(\upsilon_{12}^{CNT})^2 - 2(V_{cnt})^2\upsilon_{12}^{CNT}\upsilon^m + (V_{cnt})^2(\upsilon^m)^2 \\ + 2V_{cnt}\upsilon_{12}^{CNT}\upsilon^m - 2V_{cnt}(\upsilon^m)^2 + (\upsilon^m)^2 - 1))\end{aligned} \tag{98}$$

$$
\begin{aligned}
K_{54} = (230{,}4bh^3(&(E^m)^2V_{cnt} - (E^m)^2(V_{cnt})^2 + E_{22}^{CNT}E^m - 2E_{22}^{CNT}E^mV_{cnt} \\
&+ E_{22}^{CNT}E^m(V_{cnt})^2 - E_{11}^{CNT}E_{22}^{CNT}(V_{cnt})^2\eta_1 + E_{11}^{CNT}E^m(V_{cnt})^2\eta_1 \\
&- E_{22}^{CNT}E^m\eta_2(\upsilon^m)^2 + E_{11}^{CNT}E_{22}^{CNT}V_{cnt}\eta_1 \\
&+ 2E_{22}^{CNT}E^mV_{cnt}\eta_2(\upsilon^m)^2 - E_{22}^{CNT}E^m(V_{cnt})^2\eta_2(\upsilon_{12}^{CNT})^2 \\
&- E_{22}^{CNT}E^m(V_{cnt})^2\eta_2(\upsilon^m)^2 - 2E_{22}^{CNT}E^mV_{cnt}\eta_2\upsilon_{12}^{CNT}\upsilon^m \\
&+ 2E_{22}^{CNT}E^m(V_{cnt})^2\eta_2\upsilon_{12}^{CNT}\upsilon^m))/(L^3(E_{22}^{CNT} - E_{22}^{CNT}V_{cnt} \\
&+ E^mV_{cnt})((V_{cnt})^2(\upsilon_{12}^{CNT})^2 - 2(V_{cnt})^2\upsilon_{12}^{CNT}\upsilon^m + (V_{cnt})^2(\upsilon^m)^2 \\
&+ 2V_{cnt}\upsilon_{12}^{CNT}\upsilon^m - 2V_{cnt}(\upsilon^m)^2 + (\upsilon^m)^2 - 1))
\end{aligned}
\tag{99}
$$

$$
\begin{aligned}
K_{64} = (97bh^3(&(E^m)^2V_{cnt} - (E^m)^2(V_{cnt})^2 + E_{22}^{CNT}E^m - 2E_{22}^{CNT}E^mV_{cnt} \\
&+ E_{22}^{CNT}E^m(V_{cnt})^2 - E_{11}^{CNT}E_{22}^{CNT}(V_{cnt})^2\eta_1 + E_{11}^{CNT}E^m(V_{cnt})^2\eta_1 \\
&- E_{22}^{CNT}E^m\eta_2(\upsilon^m)^2 + E_{11}^{CNT}E_{22}^{CNT}V_{cnt}\eta_1 \\
&+ 2E_{22}^{CNT}E^mV_{cnt}\eta_2(\upsilon^m)^2 - E_{22}^{CNT}E^m(V_{cnt})^2\eta_2(\upsilon_{12}^{CNT})^2 \\
&- E_{22}^{CNT}E^m(V_{cnt})^2\eta_2(\upsilon^m)^2 - 2E_{22}^{CNT}E^mV_{cnt}\eta_2\upsilon_{12}^{CNT}\upsilon^m \\
&+ 2E_{22}^{CNT}E^m(V_{cnt})^2\eta_2\upsilon_{12}^{CNT}\upsilon^m))/(L^3(E_{22}^{CNT} - E_{22}^{CNT}V_{cnt} \\
&+ E^mV_{cnt})((V_{cnt})^2(\upsilon_{12}^{CNT})^2 - 2(V_{cnt})^2\upsilon_{12}^{CNT}\upsilon^m + (V_{cnt})^2(\upsilon^m)^2 \\
&+ 2V_{cnt}\upsilon_{12}^{CNT}\upsilon^m - 2V_{cnt}(\upsilon^m)^2 + (\upsilon^m)^2 - 1))
\end{aligned}
\tag{100}
$$

$$
\begin{aligned}
K_{74} = -(24{,}4bh^3(&(E^m)^2V_{cnt} - (E^m)^2(V_{cnt})^2 + E_{22}^{CNT}E^m - 2E_{22}^{CNT}E^mV_{cnt} \\
&+ E_{22}^{CNT}E^m(V_{cnt})^2 - E_{11}^{CNT}E_{22}^{CNT}(V_{cnt})^2\eta_1 + E_{11}^{CNT}E^m(V_{cnt})^2\eta_1 \\
&- E_{22}^{CNT}E^m\eta_2(\upsilon^m)^2 + E_{11}^{CNT}E_{22}^{CNT}V_{cnt}\eta_1 \\
&+ 2E_{22}^{CNT}E^mV_{cnt}\eta_2(\upsilon^m)^2 - E_{22}^{CNT}E^m(V_{cnt})^2\eta_2(\upsilon_{12}^{CNT})^2 \\
&- E_{22}^{CNT}E^m(V_{cnt})^2\eta_2(\upsilon^m)^2 - 2E_{22}^{CNT}E^mV_{cnt}\eta_2\upsilon_{12}^{CNT}\upsilon^m \\
&+ 2E_{22}^{CNT}E^m(V_{cnt})^2\eta_2\upsilon_{12}^{CNT}\upsilon^m))/(L^2(E_{22}^{CNT} - E_{22}^{CNT}V_{cnt} \\
&+ E^mV_{cnt})((V_{cnt})^2(\upsilon_{12}^{CNT})^2 - 2(V_{cnt})^2\upsilon_{12}^{CNT}\upsilon^m + (V_{cnt})^2(\upsilon^m)^2 \\
&+ 2V_{cnt}\upsilon_{12}^{CNT}\upsilon^m - 2V_{cnt}(\upsilon^m)^2 + (\upsilon^m)^2 - 1))
\end{aligned}
\tag{101}
$$

$$
\begin{aligned}
K_{84} = -(41{,}14bh^3((E^m)^2V_{cnt} - (E^m)^2(V_{cnt})^2 + E_{22}^{CNT}E^m - 2E_{22}^{CNT}E^mV_{cnt} \\
+ E_{22}^{CNT}E^m(V_{cnt})^2 - E_{11}^{CNT}E_{22}^{CNT}(V_{cnt})^2\eta_1 + E_{11}^{CNT}E^m(V_{cnt})^2\eta_1 \\
- E_{22}^{CNT}E^m\eta_2(\upsilon^m)^2 + E_{11}^{CNT}E_{22}^{CNT}V_{cnt}\eta_1 \\
+ 2E_{22}^{CNT}E^mV_{cnt}\eta_2(\upsilon^m)^2 - E_{22}^{CNT}E^m(V_{cnt})^2\eta_2(\upsilon_{12}^{CNT})^2 \\
- E_{22}^{CNT}E^m(V_{cnt})^2\eta_2(\upsilon^m)^2 - 2E_{22}^{CNT}E^mV_{cnt}\eta_2\upsilon_{12}^{CNT}\upsilon^m \\
+ 2E_{22}^{CNT}E^m(V_{cnt})^2\eta_2\upsilon_{12}^{CNT}\upsilon^m))/(L^2(E_{22}^{CNT} - E_{22}^{CNT}V_{cnt} \\
+ E^mV_{cnt})((V_{cnt})^2(\upsilon_{12}^{CNT})^2 - 2(V_{cnt})^2\upsilon_{12}^{CNT}\upsilon^m + (V_{cnt})^2(\upsilon^m)^2 \\
+ 2V_{cnt}\upsilon_{12}^{CNT}\upsilon^m - 2V_{cnt}(\upsilon^m)^2 + (\upsilon^m)^2 - 1))
\end{aligned}
\tag{102}
$$

$$
\begin{aligned}
K_{94} = -(5{,}19bh^3((E^m)^2V_{cnt} - (E^m)^2(V_{cnt})^2 + E_{22}^{CNT}E^m - 2E_{22}^{CNT}E^mV_{cnt} \\
+ E_{22}^{CNT}E^m(V_{cnt})^2 - E_{11}^{CNT}E_{22}^{CNT}(V_{cnt})^2\eta_1 + E_{11}^{CNT}E^m(V_{cnt})^2\eta_1 \\
- E_{22}^{CNT}E^m\eta_2(\upsilon^m)^2 + E_{11}^{CNT}E_{22}^{CNT}V_{cnt}\eta_1 \\
+ 2E_{22}^{CNT}E^mV_{cnt}\eta_2(\upsilon^m)^2 - E_{22}^{CNT}E^m(V_{cnt})^2\eta_2(\upsilon_{12}^{CNT})^2 \\
- E_{22}^{CNT}E^m(V_{cnt})^2\eta_2(\upsilon^m)^2 - 2E_{22}^{CNT}E^mV_{cnt}\eta_2\upsilon_{12}^{CNT}\upsilon^m \\
+ 2E_{22}^{CNT}E^m(V_{cnt})^2\eta_2\upsilon_{12}^{CNT}\upsilon^m))/(L^2(E_{22}^{CNT} - E_{22}^{CNT}V_{cnt} \\
+ E^mV_{cnt})((V_{cnt})^2(\upsilon_{12}^{CNT})^2 - 2(V_{cnt})^2\upsilon_{12}^{CNT}\upsilon^m + (V_{cnt})^2(\upsilon^m)^2 \\
+ 2V_{cnt}\upsilon_{12}^{CNT}\upsilon^m - 2V_{cnt}(\upsilon^m)^2 + (\upsilon^m)^2 - 1))
\end{aligned}
\tag{103}
$$

$$
\begin{aligned}
K_{104} = (2{,}4bh^3((E^m)^2V_{cnt} - (E^m)^2(V_{cnt})^2 + E_{22}^{CNT}E^m - 2E_{22}^{CNT}E^mV_{cnt} \\
+ E_{22}^{CNT}E^m(V_{cnt})^2 - E_{11}^{CNT}E_{22}^{CNT}(V_{cnt})^2\eta_1 + E_{11}^{CNT}E^m(V_{cnt})^2\eta_1 \\
- E_{22}^{CNT}E^m\eta_2(\upsilon^m)^2 + E_{11}^{CNT}E_{22}^{CNT}V_{cnt}\eta_1 \\
+ 2E_{22}^{CNT}E^mV_{cnt}\eta_2(\upsilon^m)^2 - E_{22}^{CNT}E^m(V_{cnt})^2\eta_2(\upsilon_{12}^{CNT})^2 \\
- E_{22}^{CNT}E^m(V_{cnt})^2\eta_2(\upsilon^m)^2 - 2E_{22}^{CNT}E^mV_{cnt}\eta_2\upsilon_{12}^{CNT}\upsilon^m \\
+ 2E_{22}^{CNT}E^m(V_{cnt})^2\eta_2\upsilon_{12}^{CNT}\upsilon^m))/(L^2(E_{22}^{CNT} - E_{22}^{CNT}V_{cnt} \\
+ E^mV_{cnt})((V_{cnt})^2(\upsilon_{12}^{CNT})^2 - 2(V_{cnt})^2\upsilon_{12}^{CNT}\upsilon^m + (V_{cnt})^2(\upsilon^m)^2 \\
+ 2V_{cnt}\upsilon_{12}^{CNT}\upsilon^m - 2V_{cnt}(\upsilon^m)^2 + (\upsilon^m)^2 - 1))
\end{aligned}
\tag{104}
$$

$$
\begin{aligned}
K_{55} = -(460{,}8bh^3((E^m)^2V_{cnt} - (E^m)^2(V_{cnt})^2 + E_{22}^{CNT}E^m - 2E_{22}^{CNT}E^mV_{cnt} \\
+ E_{22}^{CNT}E^m(V_{cnt})^2 - E_{11}^{CNT}E_{22}^{CNT}(V_{cnt})^2\eta_1 + E_{11}^{CNT}E^m(V_{cnt})^2\eta_1 \\
- E_{22}^{CNT}E^m\eta_2(\upsilon^m)^2 + E_{11}^{CNT}E_{22}^{CNT}V_{cnt}\eta_1 \\
+ 2E_{22}^{CNT}E^mV_{cnt}\eta_2(\upsilon^m)^2 - E_{22}^{CNT}E^m(V_{cnt})^2\eta_2(\upsilon_{12}^{CNT})^2 \\
- E_{22}^{CNT}E^m(V_{cnt})^2\eta_2(\upsilon^m)^2 - 2E_{22}^{CNT}E^mV_{cnt}\eta_2\upsilon_{12}^{CNT}\upsilon^m \\
+ 2E_{22}^{CNT}E^m(V_{cnt})^2\eta_2\upsilon_{12}^{CNT}\upsilon^m))/(L^3(E_{22}^{CNT} - E_{22}^{CNT}V_{cnt} \\
+ E^mV_{cnt})((V_{cnt})^2(\upsilon_{12}^{CNT})^2 - 2(V_{cnt})^2\upsilon_{12}^{CNT}\upsilon^m + (V_{cnt})^2(\upsilon^m)^2 \\
+ 2V_{cnt}\upsilon_{12}^{CNT}\upsilon^m - 2V_{cnt}(\upsilon^m)^2 + (\upsilon^m)^2 - 1))
\end{aligned}
\tag{105}
$$

$$
\begin{aligned}
K_{75} = (19{,}2bh^3((E^m)^2V_{cnt} - (E^m)^2(V_{cnt})^2 + E_{22}^{CNT}E^m - 2E_{22}^{CNT}E^mV_{cnt} \\
+ E_{22}^{CNT}E^m(V_{cnt})^2 - E_{11}^{CNT}E_{22}^{CNT}(V_{cnt})^2\eta_1 + E_{11}^{CNT}E^m(V_{cnt})^2\eta_1 \\
- E_{22}^{CNT}E^m\eta_2(\upsilon^m)^2 + E_{11}^{CNT}E_{22}^{CNT}V_{cnt}\eta_1 \\
+ 2E_{22}^{CNT}E^mV_{cnt}\eta_2(\upsilon^m)^2 - E_{22}^{CNT}E^m(V_{cnt})^2\eta_2(\upsilon_{12}^{CNT})^2 \\
- E_{22}^{CNT}E^m(V_{cnt})^2\eta_2(\upsilon^m)^2 - 2E_{22}^{CNT}E^mV_{cnt}\eta_2\upsilon_{12}^{CNT}\upsilon^m \\
+ 2E_{22}^{CNT}E^m(V_{cnt})^2\eta_2\upsilon_{12}^{CNT}\upsilon^m))/(L^2(E_{22}^{CNT} - E_{22}^{CNT}V_{cnt} \\
+ E^mV_{cnt})((V_{cnt})^2(\upsilon_{12}^{CNT})^2 - 2(V_{cnt})^2\upsilon_{12}^{CNT}\upsilon^m + (V_{cnt})^2(\upsilon^m)^2 \\
+ 2V_{cnt}\upsilon_{12}^{CNT}\upsilon^m - 2V_{cnt}(\upsilon^m)^2 + (\upsilon^m)^2 - 1))
\end{aligned}
\tag{106}
$$

$$
\begin{aligned}
K_{77} = -(2{,}4bh^3((E^m)^2V_{cnt} - (E^m)^2(V_{cnt})^2 + E_{22}^{CNT}E^m - 2E_{22}^{CNT}E^mV_{cnt} \\
+ E_{22}^{CNT}E^m(V_{cnt})^2 - E_{11}^{CNT}E_{22}^{CNT}(V_{cnt})^2\eta_1 + E_{11}^{CNT}E^m(V_{cnt})^2\eta_1 \\
- E_{22}^{CNT}E^m\eta_2(\upsilon^m)^2 + E_{11}^{CNT}E_{22}^{CNT}V_{cnt}\eta_1 \\
+ 2E_{22}^{CNT}E^mV_{cnt}\eta_2(\upsilon^m)^2 - E_{22}^{CNT}E^m(V_{cnt})^2\eta_2(\upsilon_{12}^{CNT})^2 \\
- E_{22}^{CNT}E^m(V_{cnt})^2\eta_2(\upsilon^m)^2 - 2E_{22}^{CNT}E^mV_{cnt}\eta_2\upsilon_{12}^{CNT}\upsilon^m \\
+ 2E_{22}^{CNT}E^m(V_{cnt})^2\eta_2\upsilon_{12}^{CNT}\upsilon^m))/(L(E_{22}^{CNT} - E_{22}^{CNT}V_{cnt} \\
+ E^mV_{cnt})((V_{cnt})^2(\upsilon_{12}^{CNT})^2 - 2(V_{cnt})^2\upsilon_{12}^{CNT}\upsilon^m + (V_{cnt})^2(\upsilon^m)^2 \\
+ 2V_{cnt}\upsilon_{12}^{CNT}\upsilon^m - 2V_{cnt}(\upsilon^m)^2 + (\upsilon^m)^2 - 1))
\end{aligned}
\tag{107}
$$

$$K_{87} = -(2{,}28bh^3((E^m)^2V_{cnt} - (E^m)^2(V_{cnt})^2 + E_{22}^{CNT}E^m - 2E_{22}^{CNT}E^mV_{cnt} + E_{22}^{CNT}E^m(V_{cnt})^2 - E_{11}^{CNT}E_{22}^{CNT}(V_{cnt})^2\eta_1 + E_{11}^{CNT}E^m(V_{cnt})^2\eta_1 - E_{22}^{CNT}E^m\eta_2(\upsilon^m)^2 + E_{11}^{CNT}E_{22}^{CNT}V_{cnt}\eta_1 + 2E_{22}^{CNT}E^mV_{cnt}\eta_2(\upsilon^m)^2 - E_{22}^{CNT}E^m(V_{cnt})^2\eta_2(\upsilon_{12}^{CNT})^2 - E_{22}^{CNT}E^m(V_{cnt})^2\eta_2(\upsilon^m)^2 - 2E_{22}^{CNT}E^mV_{cnt}\eta_2\upsilon_{12}^{CNT}\upsilon^m + 2E_{22}^{CNT}E^m(V_{cnt})^2\eta_2\upsilon_{12}^{CNT}\upsilon^m))/(L(E_{22}^{CNT} - E_{22}^{CNT}V_{cnt} + E^mV_{cnt})((V_{cnt})^2(\upsilon_{12}^{CNT})^2 - 2(V_{cnt})^2\upsilon_{12}^{CNT}\upsilon^m + (V_{cnt})^2(\upsilon^m)^2 + 2V_{cnt}\upsilon_{12}^{CNT}\upsilon^m - 2V_{cnt}(\upsilon^m)^2 + (\upsilon^m)^2 - 1)) \tag{108}$$

$$K_{97} = -(0{,}27bh^3((E^m)^2V_{cnt} - (E^m)^2(V_{cnt})^2 + E_{22}^{CNT}E^m - 2E_{22}^{CNT}E^mV_{cnt} + E_{22}^{CNT}E^m(V_{cnt})^2 - E_{11}^{CNT}E_{22}^{CNT}(V_{cnt})^2\eta_1 + E_{11}^{CNT}E^m(V_{cnt})^2\eta_1 - E_{22}^{CNT}E^m\eta_2(\upsilon^m)^2 + E_{11}^{CNT}E_{22}^{CNT}V_{cnt}\eta_1 + 2E_{22}^{CNT}E^mV_{cnt}\eta_2(\upsilon^m)^2 - E_{22}^{CNT}E^m(V_{cnt})^2\eta_2(\upsilon_{12}^{CNT})^2 - E_{22}^{CNT}E^m(V_{cnt})^2\eta_2(\upsilon^m)^2 - 2E_{22}^{CNT}E^mV_{cnt}\eta_2\upsilon_{12}^{CNT}\upsilon^m + 2E_{22}^{CNT}E^m(V_{cnt})^2\eta_2\upsilon_{12}^{CNT}\upsilon^m))/(L(E_{22}^{CNT} - E_{22}^{CNT}V_{cnt} + E^mV_{cnt})((V_{cnt})^2(\upsilon_{12}^{CNT})^2 - 2(V_{cnt})^2\upsilon_{12}^{CNT}\upsilon^m + (V_{cnt})^2(\upsilon^m)^2 + 2V_{cnt}\upsilon_{12}^{CNT}\upsilon^m - 2V_{cnt}(\upsilon^m)^2 + (\upsilon^m)^2 - 1)) \tag{109}$$

$$K_{107} = (0{,}6bh^3((E^m)^2V_{cnt} - (E^m)^2(V_{cnt})^2 + E_{22}^{CNT}E^m - 2E_{22}^{CNT}E^mV_{cnt} + E_{22}^{CNT}E^m(V_{cnt})^2 - E_{11}^{CNT}E_{22}^{CNT}(V_{cnt})^2\eta_1 + E_{11}^{CNT}E^m(V_{cnt})^2\eta_1 - E_{22}^{CNT}E^m\eta_2(\upsilon^m)^2 + E_{11}^{CNT}E_{22}^{CNT}V_{cnt}\eta_1 + 2E_{22}^{CNT}E^mV_{cnt}\eta_2(\upsilon^m)^2 - E_{22}^{CNT}E^m(V_{cnt})^2\eta_2(\upsilon_{12}^{CNT})^2 - E_{22}^{CNT}E^m(V_{cnt})^2\eta_2(\upsilon^m)^2 - 2E_{22}^{CNT}E^mV_{cnt}\eta_2\upsilon_{12}^{CNT}\upsilon^m + 2E_{22}^{CNT}E^m(V_{cnt})^2\eta_2\upsilon_{12}^{CNT}\upsilon^m))/(L(E_{22}^{CNT} - E_{22}^{CNT}V_{cnt} + E^mV_{cnt})((V_{cnt})^2(\upsilon_{12}^{CNT})^2 - 2(V_{cnt})^2\upsilon_{12}^{CNT}\upsilon^m + (V_{cnt})^2(\upsilon^m)^2 + 2V_{cnt}\upsilon_{12}^{CNT}\upsilon^m - 2V_{cnt}(\upsilon^m)^2 + (\upsilon^m)^2 - 1)) \tag{110}$$

$$\begin{aligned}K_{117} = -(&0{,}8bh^3((E^m)^2V_{cnt} - (E^m)^2(V_{cnt})^2 + E_{22}^{CNT}E^m - 2E_{22}^{CNT}E^mV_{cnt}\\&+ E_{22}^{CNT}E^m(V_{cnt})^2 - E_{11}^{CNT}E_{22}^{CNT}(V_{cnt})^2\eta_1 + E_{11}^{CNT}E^m(V_{cnt})^2\eta_1\\&- E_{22}^{CNT}E^m\eta_2(\upsilon^m)^2 + E_{11}^{CNT}E_{22}^{CNT}V_{cnt}\eta_1\\&+ 2E_{22}^{CNT}E^mV_{cnt}\eta_2(\upsilon^m)^2 - E_{22}^{CNT}E^m(V_{cnt})^2\eta_2(\upsilon_{12}^{CNT})^2\\&- E_{22}^{CNT}E^m(V_{cnt})^2\eta_2(\upsilon^m)^2 - 2E_{22}^{CNT}E^mV_{cnt}\eta_2\upsilon_{12}^{CNT}\upsilon^m\\&+ 2E_{22}^{CNT}E^m(V_{cnt})^2\eta_2\upsilon_{12}^{CNT}\upsilon^m))/(L(E_{22}^{CNT} - E_{22}^{CNT}V_{cnt}\\&+ E^mV_{cnt})((V_{cnt})^2(\upsilon_{12}^{CNT})^2 - 2(V_{cnt})^2\upsilon_{12}^{CNT}\upsilon^m + (V_{cnt})^2(\upsilon^m)^2\\&+ 2V_{cnt}\upsilon_{12}^{CNT}\upsilon^m - 2V_{cnt}(\upsilon^m)^2 + (\upsilon^m)^2 - 1))\end{aligned} \tag{111}$$

$$\begin{aligned}K_{127} = (&0{,}2bh^3((E^m)^2V_{cnt} - (E^m)^2(V_{cnt})^2 + E_{22}^{CNT}E^m - 2E_{22}^{CNT}E^mV_{cnt}\\&+ E_{22}^{CNT}E^m(V_{cnt})^2 - E_{11}^{CNT}E_{22}^{CNT}(V_{cnt})^2\eta_1 + E_{11}^{CNT}E^m(V_{cnt})^2\eta_1\\&- E_{22}^{CNT}E^m\eta_2(\upsilon^m)^2 + E_{11}^{CNT}E_{22}^{CNT}V_{cnt}\eta_1\\&+ 2E_{22}^{CNT}E^mV_{cnt}\eta_2(\upsilon^m)^2 - E_{22}^{CNT}E^m(V_{cnt})^2\eta_2(\upsilon_{12}^{CNT})^2\\&- E_{22}^{CNT}E^m(V_{cnt})^2\eta_2(\upsilon^m)^2 - 2E_{22}^{CNT}E^mV_{cnt}\eta_2\upsilon_{12}^{CNT}\upsilon^m\\&+ 2E_{22}^{CNT}E^m(V_{cnt})^2\eta_2\upsilon_{12}^{CNT}\upsilon^m))/(L(E_{22}^{CNT} - E_{22}^{CNT}V_{cnt}\\&+ E^mV_{cnt})((V_{cnt})^2(\upsilon_{12}^{CNT})^2 - 2(V_{cnt})^2\upsilon_{12}^{CNT}\upsilon^m + (V_{cnt})^2(\upsilon^m)^2\\&+ 2V_{cnt}\upsilon_{12}^{CNT}\upsilon^m - 2V_{cnt}(\upsilon^m)^2 + (\upsilon^m)^2 - 1))\end{aligned} \tag{112}$$

$$\begin{aligned}K_{88} = -(&9{,}14bh^3((E^m)^2V_{cnt} - (E^m)^2(V_{cnt})^2 + E_{22}^{CNT}E^m - 2E_{22}^{CNT}E^mV_{cnt}\\&+ E_{22}^{CNT}E^m(V_{cnt})^2 - E_{11}^{CNT}E_{22}^{CNT}(V_{cnt})^2\eta_1 + E_{11}^{CNT}E^m(V_{cnt})^2\eta_1\\&- E_{22}^{CNT}E^m\eta_2(\upsilon^m)^2 + E_{11}^{CNT}E_{22}^{CNT}V_{cnt}\eta_1\\&+ 2E_{22}^{CNT}E^mV_{cnt}\eta_2(\upsilon^m)^2 - E_{22}^{CNT}E^m(V_{cnt})^2\eta_2(\upsilon_{12}^{CNT})^2\\&- E_{22}^{CNT}E^m(V_{cnt})^2\eta_2(\upsilon^m)^2 - 2E_{22}^{CNT}E^mV_{cnt}\eta_2\upsilon_{12}^{CNT}\upsilon^m\\&+ 2E_{22}^{CNT}E^m(V_{cnt})^2\eta_2\upsilon_{12}^{CNT}\upsilon^m))/(L(E_{22}^{CNT} - E_{22}^{CNT}V_{cnt}\\&+ E^mV_{cnt})((V_{cnt})^2(\upsilon_{12}^{CNT})^2 - 2(V_{cnt})^2\upsilon_{12}^{CNT}\upsilon^m + (V_{cnt})^2(\upsilon^m)^2\\&+ 2V_{cnt}\upsilon_{12}^{CNT}\upsilon^m - 2V_{cnt}(\upsilon^m)^2 + (\upsilon^m)^2 - 1))\end{aligned} \tag{113}$$

$$K_{99} = -(2{,}37bh^3((E^m)^2V_{cnt} - (E^m)^2(V_{cnt})^2 + E_{22}^{CNT}E^m - 2E_{22}^{CNT}E^mV_{cnt} + E_{22}^{CNT}E^m(V_{cnt})^2 - E_{11}^{CNT}E_{22}^{CNT}(V_{cnt})^2\eta_1 + E_{11}^{CNT}E^m(V_{cnt})^2\eta_1 - E_{22}^{CNT}E^m\eta_2(\upsilon^m)^2 + E_{11}^{CNT}E_{22}^{CNT}V_{cnt}\eta_1 + 2E_{22}^{CNT}E^mV_{cnt}\eta_2(\upsilon^m)^2 - E_{22}^{CNT}E^m(V_{cnt})^2\eta_2(\upsilon_{12}^{CNT})^2 - E_{22}^{CNT}E^m(V_{cnt})^2\eta_2(\upsilon^m)^2 - 2E_{22}^{CNT}E^mV_{cnt}\eta_2\upsilon_{12}^{CNT}\upsilon^m + 2E_{22}^{CNT}E^m(V_{cnt})^2\eta_2\upsilon_{12}^{CNT}\upsilon^m))/(L(E_{22}^{CNT} - E_{22}^{CNT}V_{cnt} + E^mV_{cnt})((V_{cnt})^2(\upsilon_{12}^{CNT})^2 - 2(V_{cnt})^2\upsilon_{12}^{CNT}\upsilon^m + (V_{cnt})^2(\upsilon^m)^2 + 2V_{cnt}\upsilon_{12}^{CNT}\upsilon^m - 2V_{cnt}(\upsilon^m)^2 + (\upsilon^m)^2 - 1)) \tag{114}$$

$$K_{1010} = -(bh(E^m)^2G_{12}^{CNT}V_{cnt}\,h^2\,(0{,}378E^mV_{cnt}(1 - V_{cnt}) + 0{,}756(1 - V_{cnt}) + 0{,}378E^mV_{cnt}^2(4\,\eta_1 - 2\,\eta_2(\upsilon_{12}^{CNT})^2 + (\upsilon^m)^2) - 2\eta_2(\upsilon^m)^2) + 0{,}756\,\eta_2((\upsilon^m)^2 + (\upsilon^m)^3) - 4{,}08e^{34}V_{cnt}\,(1 + \upsilon^m) - 0{,}024V_{cnt}\eta_3(1 + (\upsilon^m)^2) + 6{,}12e^{34}V_{cnt}\,(\upsilon^m - 1) + 1{,}28e^33V_{cnt}\eta_3\upsilon_{12}^{CNT}(\upsilon^m - 1) + 0{,}756\eta_2\upsilon_{12}^{CNT}\upsilon^m(V_{cnt} - 1) + 1{,}92e^{33}V_{cnt}\eta_3(\upsilon^m)^2 - 4{,}08e^{34}\eta_1\upsilon^m + 1{,}28e^{33}V_{cnt}\eta_3\,(\upsilon^m)^2 + 0{,}756\eta_1\upsilon^m + 6{,}12e^{34}V_{cnt}\eta_2((\upsilon^m)^2 + (\upsilon^m)^3) - 0{,}024V_{cnt}^2\eta_3(\upsilon_{12}^{CNT})^2 + 1{,}92e^{33}(V_{cnt})^2\,\eta_3(\upsilon^m)^2 + 0{,}756\eta_2(\upsilon_{12}^{CNT})^2(V_{cnt} - 1) - 6{,}12e^{34}(V_{cnt})^2\eta_2((\upsilon^m)^2 + (\upsilon^m)^3) + 0{,}756\eta_2(\upsilon^m)^2(V_{cnt} + 1) - 4{,}08e^{34}V_{cnt}\eta_2\upsilon_{12}^{CNT}(\upsilon^m)^2 + 3{,}02(V_{cnt})^2\eta_2\upsilon_{12}^{CNT}(\upsilon^m - 1) + 3{,}02(V_{cnt})^2\,\eta_2\upsilon_{12}^{CNT}(\upsilon^m)^2 - 0{,}756(V_{cnt})^2\,\eta_2\upsilon_{12}^{CNT}\upsilon^m - 4{,}08e^{34}(V_{cnt})^3\,\eta_2\upsilon_{12}^{CNT}(\upsilon^m)^2 + 1{,}28e^{33}V_{cnt}\eta_3\upsilon_{12}^{CNT}\upsilon^m - 4{,}08e^{34}V_{cnt}\eta_2\upsilon_{12}^{CNT}\upsilon^m + 2{,}56e^{33}(V_{cnt})^2\,\eta_3\upsilon_{12}^{CNT}\upsilon^m - 1{,}28e^{33}(V_{cnt})^3\,\eta_3\upsilon_{12}^{CNT}\upsilon^m))\,/\,(L(E_{22}^{CNT} - E_{22}^{CNT}V_{cnt} + E^mV_{cnt})(2G_{12}^{CNT} + 2G_{12}^{CNT}\upsilon^m + E^mV_{cnt} - 2G_{12}^{CNT}V_{cnt} - 2G_{12}^{CNT}V_{cnt}\upsilon^m)\,((V_{cnt})^2(\upsilon_{12}^{CNT})^2 - 2(V_{cnt})^2\upsilon_{12}^{CNT}\upsilon^m + (V_{cnt})^2(\upsilon^m)^2 + 2V_{cnt}\upsilon_{12}^{CNT}\upsilon^m - 2V_{cnt}(\upsilon^m)^2 + ((\upsilon^m)^2 - 1{,}0)) \tag{115}$$

$$\begin{aligned}
K_{1110} = -(bh(E^m)^2\, G_{12}^{CNT} V_{cnt} h^2 (8{,}16e^{33} E^m V_{cnt}(1 - V_{cnt}) \\
&+ 8{,}16e^{33} E_{22}^{CNT} V_{cnt} + 1{,}632e^{34}(1 - V_{cnt}) \\
&+ 8{,}16e^{33}(V_{cnt})^2)(1 + E^m \eta_1 - 2\eta_2 (v_{12}^{CNT})^2 + (v^m)^2) \\
&- 2\,\eta_2 (v^m)^2 + \eta_1 - 2\eta_2 (v_{12}^{CNT})^2 + \eta_1) + 1{,}632e^{34} E_{22}^{CNT} \\
&+ 0{,}756\eta_2 (v^m)^2 + (v^m)^3) - 4{,}08e^{34} V_{cnt}(1 + v^m) \\
&- 2{,}24e^{33} E_{22}^{CNT} L^2 (\eta_3 + \eta_3 (v^m)^2) - 4{,}90e^{34} V_{cnt}(1 + v^m) \\
&+ 1{,}632e^{34} * (v^m + \eta_1) + 2{,}24e^{33} L^2 V_{cnt}(\eta_3 + \eta_3 (v^m)^2) \\
&- 8{,}16e^{33} E^m (V_{cnt})^2 \eta_2 (v_{12}^{CNT})^2 + (v^m)^2 + 1{,}632e^{34}\eta_1 \\
&- 8{,}16e^{33}\eta_2 (v^m)^2 + 6{,}12e^{34} V_{cnt}\eta_2((v^m)^2 + (v^m)^3) \\
&- 2{,}24e^{33} L^2 (V_{cnt})^2 \eta_3((v_{12}^{CNT})^2 + (v^m)^2) \qquad (116) \\
&- 1{,}632e^{34}\eta_2((v_{12}^{CNT})^2 + (v^m)^2) + 1{,}632e^{34}\eta_2 (v^m)^2 (V_{cnt} \\
&+ 1) - 3{,}26e^{34}\eta_2\, v_{12}^{CNT}((v^m)^2 - v^m) \\
&- 3{,}26e^{34}\,\eta_2\, v_{12}^{CNT}(v^m)^2 + 1{,}632e^{34}\eta_2 (v_{12}^{CNT})^2 (v^m + 1) \\
&+ 4{,}48e^{33}\, L^2\, V_{cnt}\,\eta_3 v_{12}^{CNT}(v^m - 1) \\
&- 8{,}96e^{33} L^2 (V_{cnt})^2 \eta_3 v_{12}^{CNT} v^m \\
&+ 4{,}48e^{33}\, L^2 (V_{cnt})^3 \eta_3 v_{12}^{CNT} v^m)) \,/\, (L(E_{22}^{CNT} - E_{22}^{CNT} V_{cnt} \\
&+ E^m V_{cnt})(2G_{12}^{CNT} + 2G_{12}^{CNT} v^m + E^m V_{cnt} - 2G_{12}^{CNT} V_{cnt} \\
&- 2G_{12}^{CNT} V_{cnt} v^m) * ((V_{cnt})^2 (v_{12}^{CNT})^2 - 2(V_{cnt})^2 v_{12}^{CNT} v^m \\
&+ (V_{cnt})^2 (v^m)^2 + 2V_{cnt} v_{12}^{CNT} v^m - 2V_{cnt}(v^m)^2 + (v^m)^2 \\
&- 1))
\end{aligned}$$

$$
\begin{aligned}
K_{1111} = -1{,}06e^{34}bh\ &(8{,}16e^{33}(E^m)^2 G_{12}^{CNT} V_{cnt} h^2 (E^m(1-V_{cnt})) + E_{22}^{CNT} \\
&+ 2\ (1-V_{cnt}) + V_{cnt}(5\eta_1 - 4\eta_2((v_{12}^{CNT})^2\ +\ (v^m)^2) \\
&- 2\eta_2(v^m)^2) + 1{,}632e^{34}E_{22}^{CNT} + 0{,}756\eta_2((v^m)^2 + (v^m)^3) \\
&-\ 4{,}08e^{34}\ (1\ + v^m) - 8{,}96e^{33}\ L^2\ (E_{22}^{CNT}\ + V_{cnt})\ (\eta_3 \\
&+ \eta_3(v^m)^2) - 8{,}16e^{33}\ E^m\ (V_{cnt})^2\ \eta_2((v_{12}^{CNT})^2 + (v^m)^2) \\
&+ 1{,}632e^{34}\eta_1 - 8{,}16e^{33}\ \eta_2(v^m)^2 +\ 6{,}12e^{34}\ V_{cnt}\ \eta_2\ ((v^m)^2 \\
&+ (v^m)^3) - 8{,}96e^{33}\ L^2\ (V_{cnt})^2\ \eta_3\ ((v_{12}^{CNT})^2 + (v^m)^2) \\
&- 1{,}632e^{34}\ \eta_2\ ((v_{12}^{CNT})^2 + (v^m)^2)\ + 1{,}632e^{34}\eta_2\ (v^m)^2\ (V_{cnt} \\
&+ 1) - 3{,}26e^{34}\ \eta_2\ v_{12}^{CNT}\ ((v^m)^2 - v^m) \\
&- 3{,}26e^{34}\ \eta_2\ v_{12}^{CNT}(v^m)^2 + 1{,}632e^{34}\ \eta_2\ (v_{12}^{CNT})^2\ (v^m + 1) \\
&+ 4{,}48e^{33}\ L^2\ V_{cnt}\ ita\_3\ v_{12}^{CNT}\ (v^m - 1) \\
&- 8{,}96e^{33}\ L^2\ (V_{cnt})^2\ \eta_3\ v_{12}^{CNT} v^m \\
&+ 4{,}48e^{33}\ L^2\ (V_{cnt})^3\ \eta_3\ v_{12}^{CNT}\ v^m)/(L(E_{22}^{CNT} - E_{22}^{CNT} V_{cnt} \\
&+ E^m V_{cnt})(2G_{12}^{CNT}\ + 2G_{12}^{CNT} v^m\ +\ E^m V_{cnt} - 2G_{12}^{CNT} V_{cnt} \\
&- 2G_{12}^{CNT} V_{cnt} v^m) * ((V_{cnt})^2\ (v_{12}^{CNT})^2\ - 2(V_{cnt})^2 v_{12}^{CNT}\ v^m \\
&+ (V_{cnt})^2 (v^m)^2 + 2V_{cnt} v_{12}^{CNT} v^m - 2V_{cnt}(v^m)^2 + (v^m)^2\ - 1))
\end{aligned}
\tag{117}
$$

The remaining elements of the matrix are defined as follows:

$$
\begin{gathered}
K_{11} = K_{33}, K_{104} = K_{124}, K_{114} = -2K_{104}, K_{124} = -K_{104}, K_{95} = -K_{75} \\
K_{46} = K_{65}, K_{66} = K_{44} \\
K_{76} = K_{94}, K_{85} = K_{105} = K_{115} =\ K_{125} = K_{108} = K_{118} = K_{128} = 0 \\
K_{86} = -K_{84}, K_{96} = -K_{74}, K_{106} = -K_{104} = K_{126}\ , K_{116} = -2K_{106}, \\
K_{57} = K_{54},, K_{78} = K_{98}\ ,, K_{109} = K_{127}, K_{129} = K_{107} \\
K_{1210} = -K_{1110},\ K_{1211} = K_{1110}, K_{1212} = K_{1210}
\end{gathered}
\tag{118}
$$

2.5.2. Mass Matrix for One Element

The mass matrix for one element of a finite element model is obtained by enclosing the data obtained by calculating the kinetic energy in a common parenthesis. This matrix is 12x12 and is given.

$$[M]=\begin{bmatrix} M_{11} & M_{12} & M_{13} & 0 & 0 & 0 & 0 & 0 & 0 & 0 & 0 & 0 \\ M_{21} & M_{22} & M_{23} & 0 & 0 & 0 & 0 & 0 & 0 & 0 & 0 & 0 \\ M_{31} & M_{32} & M_{33} & 0 & 0 & 0 & 0 & 0 & 0 & 0 & 0 & 0 \\ 0 & 0 & 0 & M_{44} & M_{45} & M_{46} & M_{47} & M_{48} & M_{49} & M_{410} & M_{411} & M_{412} \\ 0 & 0 & 0 & M_{54} & M_{55} & M_{56} & M_{57} & M_{58} & M_{59} & M_{510} & M_{511} & M_{512} \\ 0 & 0 & 0 & M_{64} & M_{65} & M_{66} & M_{67} & M_{68} & M_{69} & M_{610} & M_{611} & M_{612} \\ 0 & 0 & 0 & M_{74} & M_{75} & M_{76} & M_{77} & M_{78} & M_{79} & M_{710} & M_{711} & M_{712} \\ 0 & 0 & 0 & M_{84} & M_{85} & M_{86} & M_{87} & M_{88} & M_{89} & M_{810} & M_{811} & M_{812} \\ 0 & 0 & 0 & M_{94} & M_{95} & M_{96} & M_{97} & M_{98} & M_{99} & M_{910} & M_{911} & M_{912} \\ 0 & 0 & 0 & M_{104} & M_{105} & M_{106} & M_{107} & M_{108} & M_{109} & M_{1010} & M_{1011} & M_{1012} \\ 0 & 0 & 0 & M_{114} & M_{115} & M_{116} & M_{117} & M_{118} & M_{119} & M_{1110} & M_{1111} & M_{1112} \\ 0 & 0 & 0 & M_{124} & M_{125} & M_{126} & M_{127} & M_{128} & M_{129} & M_{1210} & M_{1211} & M_{1212} \end{bmatrix}$$

The mass matrix variables for one element are shown.

$$M_{11} = \left(\frac{2Lbh(\rho^m + V_{cnt}\rho^{CNT} - V_{cnt}\rho^m)}{45}\right) \tag{119}$$

$$M_{44} = \left(\frac{bh((1046L^2 + 13761h^2)(\rho^m + V_{cnt}\rho^{CNT} - V_{cnt}\rho^m)}{20790L}\right) \tag{120}$$

$$M_{54} = \left(\frac{4bh((5L^2 - 144h^2)(\rho^m + V_{cnt}\rho^{CNT} - V_{cnt}\rho^m)}{945L}\right) \tag{121}$$

$$M_{64} = \left(\frac{bh((131L^2 - 1089h^2)(\rho^m + V_{cnt}\rho^{CNT} - V_{cnt}\rho^m)}{20790L}\right) \tag{122}$$

$$M_{74} = \left(\frac{bh((76L^2 + 429h^2)(\rho^m + V_{cnt}\rho^{CNT} - V_{cnt}\rho^m)}{83160}\right) \tag{123}$$

$$M_{84} = -\left(\frac{2bh(4L^2 - 99h^2)(\rho^m + V_{cnt}\rho^{CNT} - V_{cnt}\rho^m)}{6237}\right) \tag{124}$$

$$M_{94} = -\left(\frac{bh(58L^2 + 297h^2)(\rho^m + V_{cnt}\rho^{CNT} - V_{cnt}\rho^m)}{249480}\right) \tag{125}$$

$$M_{104} = \left(\frac{101bh^3(\rho^m + V_{cnt}\rho^{CNT} - V_{cnt}\rho^m)}{3150}\right) \tag{126}$$

$$M_{114} = \left(\frac{4bh^3(\rho^m + V_{cnt}\rho^{CNT} - V_{cnt}\rho^m)}{150}\right) \tag{127}$$

$$M_{124} = -\left(\frac{11bh^3(\rho^m + V_{cnt}\rho^{CNT} - V_{cnt}\rho^m)}{3150}\right) \tag{128}$$

$$M_{55} = \left(\frac{128bh(L^2 + 9h^2)(\rho^m + V_{cnt}\rho^{CNT} - V_{cnt}\rho^m)}{945L}\right) \quad (129)$$

$$M_{75} = \left(\frac{2bh(L^2 - 9h^2)(\rho^m + V_{cnt}\rho^{CNT} - V_{cnt}\rho^m)}{2835}\right) \quad (130)$$

$$M_{105} = \left(\frac{-8bh^3(\rho^m + V_{cnt}\rho^{CNT} - V_{cnt}\rho^m)}{225}\right) \quad (131)$$

$$M_{106} = \left(\frac{11bh^3(\rho^m + V_{cnt}\rho^{CNT} - V_{cnt}\rho^m)}{3150}\right) \quad (132)$$

$$M_{116} = \left(\frac{-4bh^3(\rho^m + V_{cnt}\rho^{CNT} - V_{cnt}\rho^m)}{105}\right) \quad (133)$$

$$M_{77} = \left(\frac{Lbh^3(4L^2 + 231h^2)(\rho^m + V_{cnt}\rho^{CNT} - V_{cnt}\rho^m)}{187110}\right) \quad (134)$$

$$M_{87} = -\left(\frac{Lbh^3(L^2 + 11h^2)(\rho^m + V_{cnt}\rho^{CNT} - V_{cnt}\rho^m)}{31185}\right) \quad (135)$$

$$M_{97} = -\left(\frac{Lbh(2L^2 + 55h^2)(\rho^m + V_{cnt}\rho^{CNT} - V_{cnt}\rho^m)}{249480}\right) \quad (136)$$

$$M_{107} = -\left(\frac{13Lbh^3(\rho^m + V_{cnt}\rho^{CNT} - V_{cnt}\rho^m)}{18900}\right) \quad (137)$$

$$M_{117} = \left(\frac{Lbh^3(\rho^m + V_{cnt}\rho^{CNT} - V_{cnt}\rho^m)}{1575}\right) \quad (138)$$

$$M_{127} = \left(\frac{Lbh^3(\rho^m + V_{cnt}\rho^{CNT} - V_{cnt}\rho^m)}{18900}\right) \quad (139)$$

$$M_{88} = \left(\frac{32Lbh^3(L^2 + 33h^2)(\rho^m + V_{cnt}\rho^{CNT} - V_{cnt}\rho^m)}{93555}\right) \quad (140)$$

$$M_{98} = -\left(\frac{Lbh(L^2 + 11h^2)(\rho^m + V_{cnt}\rho^{CNT} - V_{cnt}\rho^m)}{31185}\right) \quad (141)$$

$$M_{108} = \left(\frac{8Lbh^3(\rho^m + V_{cnt}\rho^{CNT} - V_{cnt}\rho^m)}{4725}\right) \quad (142)$$

$$M_{99} = -\left(\frac{Lbh(4L^2 + 231h^2)(\rho^m + V_{cnt}\rho^{CNT} - V_{cnt}\rho^m)}{187110}\right) \quad (143)$$

$$M_{1010} = \left(\frac{34Lbh^3(\rho^m + V_{cnt}\rho^{CNT} - V_{cnt}\rho^m)}{14175}\right) \quad (144)$$

The remaining elements of the matrix are defined as follows:

$$
\begin{gathered}
M_{31} = M_{13} = \frac{-M_{11}}{4},\ M_{21} = \frac{M_{11}}{2},\ M_{22} = 4M_{11}, M_{33} = M_{11}, M_{45} = M_{65} \\
M_{58} = 0, M_{95} = -M_{75}, M_{125} = -M_{105}, M_{44} = M_{66}, M_{76} = -M_{94}, M_{86} = -M_{84} \\
M_{96} = -M_{74}, M_{126} = -M_{104},, M_{67} = -M_{49},, M_{118} = -2M_{108}, M_{128} = M_{108} \\
M_{109} = M_{127}, M_{410} = M_{104}, M_{510} = M_{105}, M_{610} = M_{106}, M_{710} = M_{107} \\
M_{810} = M_{108}, M_{910} = M_{109}, M_{119} = M_{117}, M_{129} = M_{107}, M_{1110} = \frac{M_{1010}}{2} \\
M_{1210} = -\frac{M_{1010}}{4}, M_{1111} = 4M_{1010}, M_{1211} = M_{1110}, M_{1212} = M_{1010}
\end{gathered}
\tag{145}
$$

2.6. Geometric Stiffness Matrix for One Element

The geometric stiffness matrix for one element of a finite element model is obtained by enclosing the data obtained by calculating the work done by N_{cr} in a common parenthesis. This matrix is 12x12 and is given.

$$
K_G = \frac{b}{L}\begin{bmatrix}
0 & 0 & 0 & 0 & 0 & 0 & 0 & 0 & 0 & 0 & 0 & 0 \\
0 & 0 & 0 & 0 & 0 & 0 & 0 & 0 & 0 & 0 & 0 & 0 \\
0 & 0 & 0 & 0 & 0 & 0 & 0 & 0 & 0 & 0 & 0 & 0 \\
0 & 0 & 0 & 7{,}94 & -7{,}31 & -0{,}63 & 0{,}06L & 0{,}38L & 0 & 0 & 0 & 0 \\
0 & 0 & 0 & -7{,}31 & 14{,}63 & -7{,}31 & -0{,}07L & 0 & 0 & 0 & 0 & 0 \\
0 & 0 & 0 & -0{,}63 & -7{,}31 & 7{,}94 & 0{,}01L & -0{,}38L & 0 & 0 & 0 & 0 \\
0 & 0 & 0 & 0{,}06L & -0{,}076L & 0{,}01L & 0{,}01L^2 & -0{,}04L^2 & 0 & 0 & 0 & 0 \\
0 & 0 & 0 & 0{,}38L & 0 & -0{,}38L & -0{,}004L^2 & 0{,}135L^2 & 0 & 0 & 0 & 0 \\
0 & 0 & 0 & -0{,}014L & 0{,}076L & -0{,}06L & -0{,}002L^2 & -0{,}04 & 0 & 0 & 0 & 0 \\
0 & 0 & 0 & 0 & 0 & 0 & 0 & 0 & 0 & 0 & 0 & 0 \\
0 & 0 & 0 & 0 & 0 & 0 & 0 & 0 & 0 & 0 & 0 & 0 \\
0 & 0 & 0 & 0 & 0 & 0 & 0 & 0 & 0 & 0 & 0 & 0
\end{bmatrix}
$$

2.7. Force Matrix for One Element

The force matrix for one element of a finite element model is obtained by enclosing the data obtained by calculating the work done by q_0 in a common parenthesis. This matrix is 1x12 and is given.

$$F = q_0 \begin{bmatrix} 0 \\ 0 \\ 0 \\ -0,078L \\ -0,178L \\ -0,078L \\ -0,00185L^2 \\ 0 \\ 0,00185L^2 \\ 0 \\ 0 \\ 0 \end{bmatrix}$$

3. NUMERICAL RESULTS

3.1. General Information and Formulation

This study investigates the free vibration, buckling, and bending behavior of an FG-CNTRC beam using FEM and HSDT. A convergence study was handled to ensure the finite element model's accuracy. Free vibration analysis was then performed using two unique dimensionless equations. After initial comparisons with existing literature, a series of parametric studies were conducted. Subsequently, a bending analysis was carried out, assessing dimensionless deflection and stresses ($w,\ \sigma_{xx}\ and\ \sigma_{xz}$) against those obtained from other studies, and the effect of bending on the beam was examined in detail. Finally, a buckling analysis was undertaken, comparing the dimensionless data to findings from different beam theories. This in-depth investigation, with its rigorous validation and detailed analyses, provides valuable insights into the FG-CNTRC beam's response under various loading conditions, contributing to the existing scientific discourse.

The system's natural frequencies are yielded by Eq. (90). Eqs. (146) and (147) are subsequently utilized to calculate the non-dimensional forms of these frequencies.

$$\bar{\omega}_i = \omega_i \frac{L^2}{h}\sqrt{\frac{\rho^m}{E^m}} \tag{146}$$

Here $\bar{\omega}_i$ presents non-dimensional natural frequencies.

$$\bar{\omega}_i = \omega_i L\sqrt{\frac{I_0^m}{A_{11}^m}} \tag{147}$$

$I_0^m\ and\ A_{11}^m$ are given below:

$$I_0^m = \int_{-h}^{h} \rho^m (1-(\nu^m)^2) dz \text{ and } A_{11}^m = \int_{-h}^{h} E^m dz \tag{148a,b}$$

Eq. (92) enables the computation of variables relevant to bending analysis. Subsequently, the following equations are the non-dimensional formulas.

$$\bar{w} = \frac{100E_m h^3 w(L/2)}{q_0 L^4}, \bar{\sigma}_{xx} = \frac{h}{q_0 L}\sigma_{xx}\left(\frac{L}{2},\frac{h}{2}\right), \bar{\sigma}_{xz} = \frac{h}{q_0 L}\sigma_{xz}(0,0) \qquad \text{(149a,b,c)}$$

When Eq. (91) computed, the critical buckling load (N_{cr}) can be further utilized to derive its non-dimensional form via Eq. (149). The dimensionless critical buckling loads ($\overline{N}_{cr}$) is obtained.

$$\overline{N}_{cr} = \frac{N_{cr}}{A_{11}^m} \qquad (150)$$

3.1.1. Material Properties

When the studies conducted in literature are examined, it is seen that they divide the studies on material properties into two. To provide a comprehensive analysis, this study combines comparisons with previous studies and investigates two different material properties.

Tables 4 and 5 present data for Material Property A, while Tables 6 and 7 present data for Material Property B. To simplify references in calculations and analyses, these datasets will be designated as Material Property A and Material Property B, respectively.

Table 4. Material properties for (10,10) SWCNT (length = 9.26 nm, radius = 0.68 nm, thickness = 0.067 nm) and matrix

Property	CNT	Unit	Property	Matrix	Unit
$\mathbf{E_{11}^{cnt}}$	5,6466	TPa	E^m	2,5	GPa
$\mathbf{E_{22}^{cnt}}$	7,08	TPa	G^m	0,93	GPa
$\mathbf{G_{12}^{cnt}}$	1,9445	GPa	ρ^m	1150	kg/m^3
$\boldsymbol{\rho}^{\mathbf{cnt}}$	1400	kg/m^3	ν^m	0,34	
$\boldsymbol{\nu}_{\mathbf{12}}^{\mathbf{cnt}}$	0,175				

Table 5. Total volume fractions and efficiency parameters of CNTs

V_{tcnt}	η_1	η_2	η_3
0,12	0,137	1,022	0,715
0,17	0,142	1,626	1,138
0,28	0,141	1,585	1,109

Table 6. Material properties for SWCNT and matrix (Yas and Samadi 2012)

Property	CNT	UNIT	PROPERTY	MATRIX	UNIT
$\mathbf{E_{11}^{cnt}}$	600	GPa	E^m	2,5	GPa
$\mathbf{E_{22}^{cnt}}$	10	GPa	G^m	0,962	GPa
$\mathbf{G_{12}^{cnt}}$	17,2	GPa	ρ^m	1190	kg/m^3
$\boldsymbol{\rho^{cnt}}$	1400	kg/m^3	ν^m	0,3	
$\boldsymbol{\nu_{12}^{cnt}}$	0,19				

Table 7. Total volume fractions and efficiency parameters of CNTs

V_{tcnt}	η_1	η_2	η_3
0,12	1,2833	1,0556	1,0556
0,17	1,3414	1,7101	1,7101
0,28	1,3238	1,7380	1,7380

In the calculations, Material Property A was used in a few specific cases, while Material Property B was used for the remaining calculations. If no group is specified, Material Property B is used by default.

3.1.2. Boundary Conditions

The analyses encompass four distinct boundary conditions, derived from the classical boundary conditions of clamped (C), simply supported (S), and free (F) (Figure 8). This allows for the evaluation of structural responses under diverse constraints, facilitating a comprehensive understanding of the behavior of the systems under investigation.

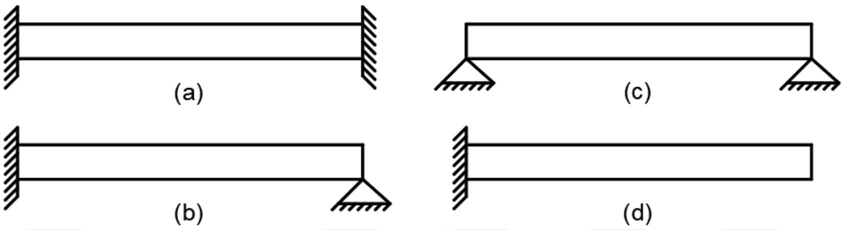

Figure 8. (a) Clamped-Clamped, (b) Clamped-Simply Supported, (c) Simply S.-Simply S., (d) Clamped-Free support types

These boundaries can be defined as

Clamped-Clamped(C-C): $u(0)=u(L)=w(0)=w(L)=\beta(0)=\beta(L)=\phi(0)=\phi(L)=0$

Clamped-Simply Supported (C-S): $u(0)=w(0)=w(L)=\beta(0)= \phi(0)=0$

Simply Supported-Simply Supported (S-S): $u(0)=w(0)=w(L)=0$

Clamped-Free(C-F): $u(0)=w(0)=w(L)=0$

3.2. Convergence Analysis

Convergence analyses were conducted for free vibration, bending, and buckling to determine the optimal number of finite elements needed. For the free vibration analysis, the convergence was assessed using material properties A. In the case of buckling and bending analyses, material properties B were implemented.

The figure 9 shows the convergence of the finite element model for free vibration analysis of a beam with different boundary conditions (C-F, C-S, S-S, and C-C). The Table 8 shows that the results converge to a constant value as the number of elements increases. The element number of approximately 20 elements is sufficient to obtain accurate results for all support types.

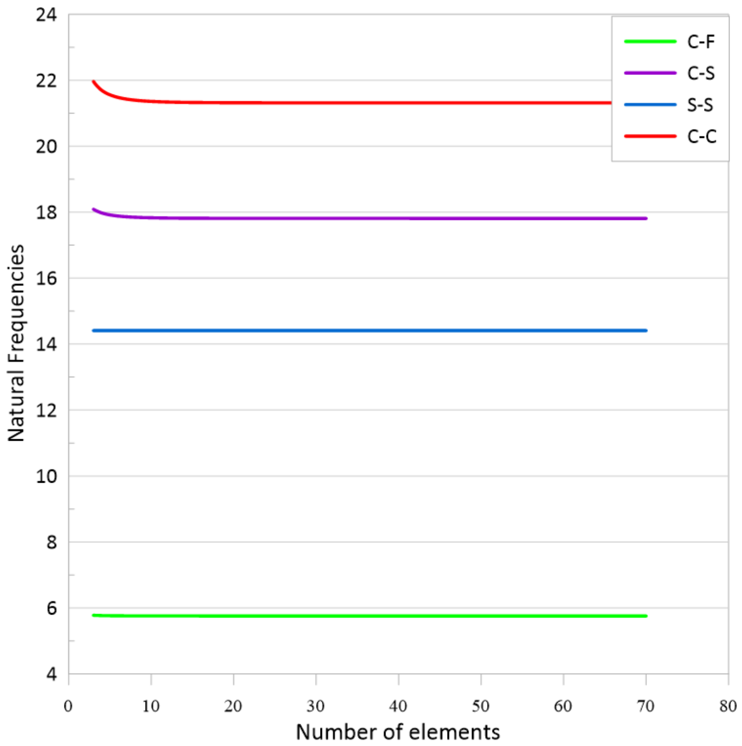

Figure 9. Convergence analysis in case of free vibration for boundary conditions (UD, L_t/h=15 and $V_{tcnt} = 0{,}12$)

Table 8. Convergence analysis values in case of free vibration

No	$\bar{\omega}$ C-C	$\bar{\omega}$ S-S	$\bar{\omega}$ C-S	$\bar{\omega}$ C-F
3	21,96297	14,4090	18,08839	5,77776
5	21,55848	14,4090	17,91784	5,76435
10	21,36004	14,4090	17,83093	5,75744
20	21,31893	14,4090	17,81282	5,75600
30	21,31491	14,4090	17,81105	5,75586

Figure 10 and Table 9 show the convergence analysis for bending of a beam with different support types. The four support types are C-F, C-S, S-S, C-C. The convergence analysis shows that a mesh size of approximately 20 elements is sufficient to obtain accurate results for all support types.

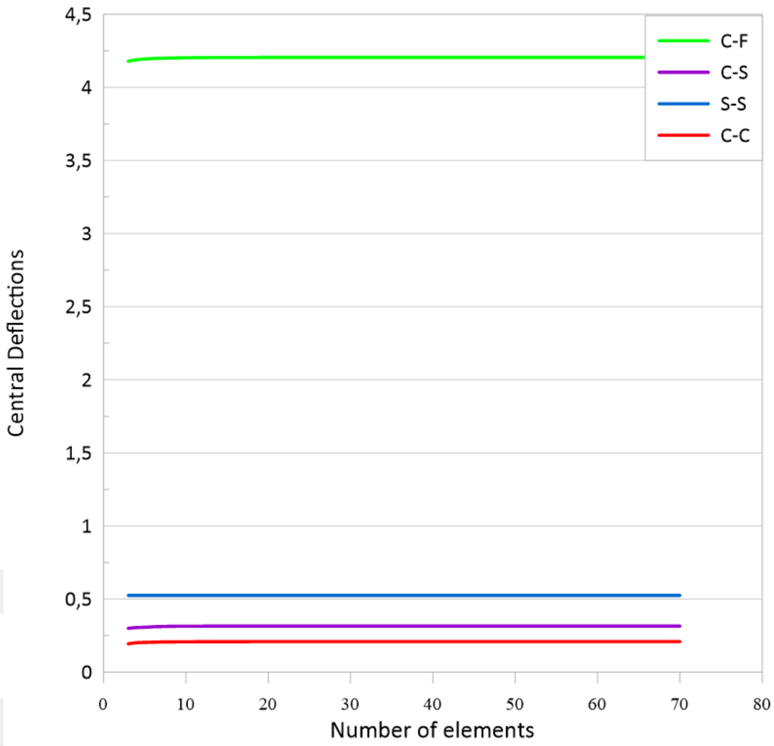

Figure 10. Convergence analysis in case of bending for boundary conditions (UD, L_t/h =15 and $V_{tcnt} = 0{,}12$)

Table 9. Convergence analysis values in case of bending

No	$\overline{w}$ C-C	$\overline{w}$ S-S	$\overline{w}$ C-S	$\overline{w}$ C-F
3	0,1940	0,5250	0,2996	3,3521
5	0,2034	0,5250	0,3069	3,7013
10	0,2077	0,5250	0,3141	3,9573
20	0,2087	0,5250	0,3149	4,0822
30	0,2089	0,5250	0,3150	4,1233

It is noteworthy that the convergence behavior observed in the bending analysis differs from that of the free vibration. Specifically, while the natural frequencies converged from higher to lower values with increasing element number, the central deflection exhibited convergence from lower to higher values.

Figure 11 and Table 10 show the convergence analysis for buckling of a beam with different support types. The four support types are C-F, C-S, S-S, C-C. The convergence analysis shows that a mesh size of approximately 5 elements is sufficient to obtain accurate results for all support types. This is faster convergence than others.

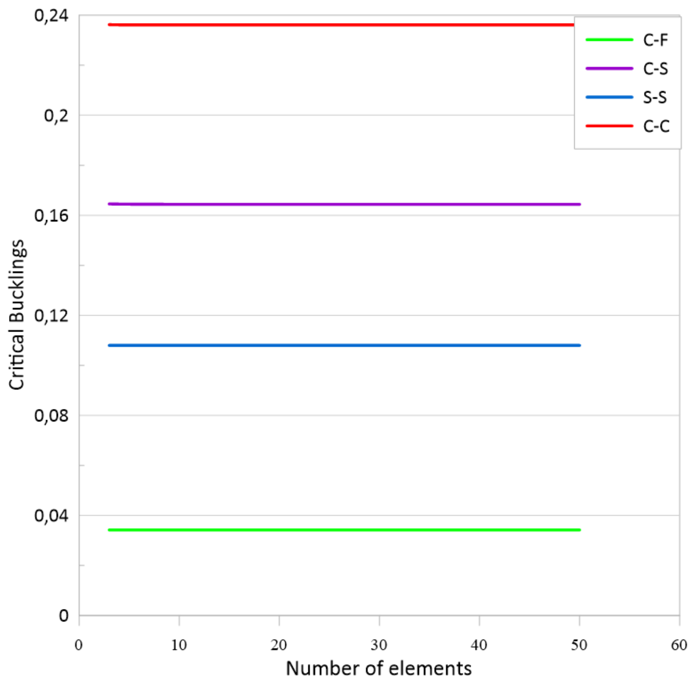

Figure 11. Convergence Analysis in case of Buckling for boundary conditions (UD, L_t/h=15 and $V_{tcnt} = 0{,}12$)

Table 10. Convergence analysis values in case of buckling

No	$\bar{N}_{cr}$ C-C	$\bar{N}_{cr}$ S-S	$\bar{N}_{cr}$ C-S	$\bar{N}_{cr}$ C-F
3	0,2362	0,1079	0,1644	0,0342
5	0,2361	0,1079	0,1644	0,0342
10	0,2361	0,1079	0,1644	0,0342
20	0,2361	0,1079	0,1644	0,0342
30	0,2361	0,1079	0,1644	0,0342

The convergence analysis revealed that a maximum of 20 elements were sufficient for accurate results in both free vibration and bending analyses. Although buckling analysis achieved convergence with only 5 elements, a consistent mesh density of 20 elements was employed across all analyses to ensure accuracy and comparability of results.

3.3. Literature Verifications and Parametric Studies

3.3.1. Free Vibration Analysis

Free vibration analysis of beams is crucial for understanding the dynamic behavior of beams subjected to self-induced vibrations. By concluding natural frequencies and evaluating mode shapes, engineers can optimize structural designs to minimize vibrations and ensure their stability and integrity. Two different dimensionless equations were used for the analysis of free vibration. This made it easier to compare study with the work done in literature.

Table 11 presents a comparison of the first three dimensionless frequency values obtained using the present method with those from previous studies by El-Ashmawy and Xu (2021) uses the Timoshenko Beam Theory to analyze FG-CNTRC beams, considering the combined effects of CNT distribution and orientation.

Shen and Xiang (2013) examine the nonlinear behavior of CNTRC beams under thermal loads and resting on elastic foundations. They use a HSDT, incorporating von Kármán-type nonlinear strain-displacement relationships and temperature-dependent material properties, to accurately model the beam's behavior.

While HSDT theories provide consistent results, those obtained using Timoshenko beam theory differ because Timoshenko beam theory makes simplifying assumptions about shear deformation. The most significant difference between the results of the current study and those of Ashmawy and Xu was observed for the FGX distribution, with a discrepancy of approximately 3%. However, the difference compared to Shen and Xiang was only 0.25%. Additionally, the dimensionless frequency values ($\overline{\omega}$) increase with increasing V_{cnt}. This is because the addition of CNTs to a material increases its overall stiffness, which in turn increases its natural frequency. Under simply supported boundary conditions and different volume participation rates, the highest frequency value fits to the FGX type, respected by UD, FGA, and FGO. The FGX beam concentrates the CNTs at the bottom and top surfaces, which increases the stiffness of the beam in the direction of vibration. This results in the highest $\overline{\omega}$ among the various distribution forms. In contrast, UD beam distributes the CNTs evenly throughout the beam, leading to a lower overall stiffness and consequently a lower $\overline{\omega}$. FGA and FGO beams, with CNTs concentrated at the bottom and top surfaces, respectively, exhibit stiffness values intermediate between those of UD and FGX beams, resulting in $\overline{\omega}$ that are also intermediate.

Table 11. First three ϖ of a simply supported CNTRC beam under different volume fraction (Material Properties A, L_t/h =25, $\theta = 0$)

V_{tcnt}	Mode	UD			FGA		
		Present	**Ashmawy and Xu**	**Shen and Xiang**	**Present**	**Ashmawy and Xu**	**Shen and Xiang**
0,12	**1**	15,8392	15,8148	15,8363	13,4499	13,4511	13,4544
	2	51,8757	51,6607	51,8139	46,1950	46,1618	46,1920
	3	94,0644	93,3683	93,8709	86,9513	86,6553	86,8513
0,17	**1**	19,2008	19,2010	19,2279	16,2046	16,2280	16,2286
	2	63,9377	63,9514	64,1381	56,4901	56,6928	56,6836
	3	117,3307	117,2675	117,8051	107,6941	108,1098	108,1428
0.28	**1**	23,4822	23,4464	23,4774	19,9525	19,9925	19,9556
	2	74,5538	74,2254	74,4687	67,0470	67,3244	66,9973
	3	132,4392	131,3010	132,2442	124,0637	124,4254	123,8009
		FGX			**FGO**		
		Present	**Ashmawy and Xu**	**Shen and Xiang**	**Present**	**Ashmawy and Xu**	**Shen and Xiang**
0,12	**1**	18,6027	18,5920	18,5983	12,3429	-	-
	2	57,6024	57,4009	57,5277	42,7818	-	-
	3	100,8452	99,9028	100,6202	81,0416	-	-
0,17	**1**	22,6113	22,7147	22,6562	14,8457	-	-
	2	71,1065	71,7838	71,3956	52,3711	-	-
	3	125,6061	126,7454	126,2215	100,7911	-	-
0.28	**1**	27,1931	27,5868	27,1821	18,3527	-	-
	2	80,4656	82,7892	80,3436	63,1911	-	-
	3	137,6125	141,7860	137,3035	119,0170	-	-

Table 12 compares the first dimensionless frequency values for a beam with L_t/h = 12, obtained using Eq. (147) in case of different support types (C-C, S-S, C-S, C-F). A comparison with Ashmawy and Xu showed that the effect of support was applied correctly. When the table is examined, the highest natural frequency values are observed for the C-C type support, regardless of the support type. The highest frequency value is 1.9914 at a participation rate of 0.28 in the FGX beam. The dimensionless natural frequency value increases as the V_{cnt} increases regardless of the support type. The ϖ values of the FGX beam are higher than the others. The $\bar{\omega}$ of a beam in free vibration analysis is affected by the beam's stiffness, which is in turn influenced by the support type. When the support types are compared, C-C beams exhibit the highest stiffness and consequently the highest $\bar{\omega}$, followed by C-S, S-S, and C-F beams. This ordering arises from the varying levels of constraint imposed by the different support types, with C-C providing the most constraint and C-F the least. A stiffer beam can resist deformation more efficiently, lead to in a higher $\bar{\omega}$.

Table 12. The first $\bar{\omega}$ values of CNTRC beams under different support and volume fractions (Material Properties A, L_t/h=12, $\theta = 0$)

Boundary Condition	V_{tcnt}	**UD**		**FGA**		**FGX**		**FGO**	
		Present	**Xu**	**Present**	**Xu**	**Present**	**Xu**	**Present**	**Xu**
C-C	**0,12**	1,4035	1,3258	1,3420	1,2765	1,4713	1,3715	1,2407	-
	0,17	1,7634	1,6886	1,6789	1,6208	1,8399	1,7605	1,5652	-
	0.28	1,9554	1,8287	1,8919	1,8034	1,9914	1,9225	1,8124	-
S-S	**0,12**	0,9981	0,9933	0,8921	0,8911	1,1040	1,0998	0,8266	-
	0,17	1,2317	1,2315	1,0922	1,0960	1,3642	1,3777	1,0134	-
	0,28	1,4315	1,4240	1,2925	1,2976	1,5380	1,5831	1,2203	-
C-S	**0,12**	1,1936	1,1538	1,1136	1,0852	1,2749	1,2236	1,0320	-
	0,17	1,4904	1,4556	1,3824	1,3622	1,5878	1,5570	1,2883	-
	0,28	1,6793	1,6135	1,5848	1,5492	1,7424	1,7319	1,5134	-
C-F	**0,12**	0,4105	-	0,3557	-	0,4706	-	0,3269	-
	0,17	0,5010	-	0,4310	-	0,5758	-	0,3959	-
	0,28	0,6009	-	0,5233	-	0,6745	-	0,4848	-

Table 13 presents a comparison of the first three $\bar{\omega}$ for CNTRC beams attained in the present study with those reported by Yas and Samadi (2012), who employed Hamilton's principle and Timoshenko beam theory in their free vibration analysis. The frequencies were calculated using Material Property B for a S-S boundary condition with various volume fractions. Furthermore, FGX distribution yields the highest $\bar{\omega}$ at a participation rate of 0,28, followed by UD, FGA, and FGO in descending rank. FGX distributions have higher $\bar{\omega}$ than other CNT distributions because they concentrate the CNTs at the bottom and top surfaces of the beam, which are the regions that experience the most stress during vibration. The highest one is attained with the FGX distribution, a S-S support type, and a participation rate of 0,28. The maximum discrepancy between results is observed for the FGX distribution at a volume fraction of 0,28, exhibiting a difference of approximately 3,36%.

Table 13. First three ϖ of a CNTRC beam under different volume fraction (S-S, Material Properties B, L_t/h =15, $\theta = 0$)

V_{tcnt}	Mode		UD	FGA	FGX	FGO
0,12	1	Present	0,9736	0,9431	1,1146	0,7438
		Yas and Samadi (2012)	0,9753	0,9453	1,1150	0,7527
	2	Present	2,8787	2,6419	3,1002	2,3927
		Yas and Samadi (2012)	2,8728	2,6424	3,0814	2,4562
	3	Present	4,9275	4,7080	5,1683	4,2854
		Yas and Samadi (2012)	4,8704	4,6675	5,0695	4,4320
0,17	1	Present	1,1971	1,1568	1,3752	0,9067
		Yas and Samadi (2012)	1,1999	1,1609	1,3830	0,9155
	2	Present	3,6269	3,2977	3,9084	2,9937
		Yas and Samadi (2012)	3,6276	3,3084	3,9293	3,0577
	3	Present	6,2827	5,9676	6,5691	5,4590
		Yas and Samadi (2012)	6,2363	5,9498	6,5447	5,6139
0,28	1	Present	1,4352	1,3919	1,6107	1,1134
		Yas and Samadi (2012)	1,4401	1,4027	1,6493	1,1202
	2	Present	4,1327	3,8269	4,3246	3,5628
		Yas and Samadi (2012)	4,1362	3,8639	4,4752	3,6056
	3	Present	6,9927	6,7416	7,1262	6,3589
		Yas and Samadi (2012)	6,9245	6,7618	7,3068	6,4434

Table 14 presents the dimensionless frequency parameters for UD, FGA, FGX and FGO beams under different slenderness ratios, boundary conditions, and volume fractions. The results show that the ϖ decrease as the slenderness ratio increases. Similarly, the ϖ decrease as the boundary conditions become looser, progressing from C-C to C-S, then S-S, and finally C-F. Conversely, the ϖ increase as the V_{cnt} increases. However, the frequency parameters for FGX and FGO beams increase as the volume fraction increases. The analysis reveals that beams with the FGX beams exhibit the highest ϖ, followed by UD and FGA beams, while FGO beams consistently have the lowest ϖ. The C-F, S-S, and C-S boundaries exhibit decreasing rates, with the smallest change observed in the C-C support type.

Table 14. The first $\overline{\omega}$ values of UD, FGA, FGX and FGO beams under various L_t/h, boundary conditions and V_{tcnt}

L_t/h	V_{tcnt}	UD				FGA			
		C-C	**S-S**	**C-S**	**C-F**	**C-C**	**S-S**	**C-S**	**C-F**
10	**0,12**	1,4880	1,1197	1,2896	0,4814	1,4402	1,0982	1,2219	0,4242
	0,17	1,8727	1,3895	1,6154	0,5897	1,8065	1,3603	1,5230	0,5154
	0,28	2,0628	1,5815	1,7988	0,6936	2,0161	1,5601	1,7217	0,6156
15	**0,12**	1,3366	0,9034	1,1168	0,3609	1,2615	0,8780	1,0263	0,3089
	0,17	1,6730	1,1070	1,3873	0,4377	1,5697	1,0734	1,2657	0,3720
	0,28	1,8653	1,3008	1,5757	0,5286	1,7802	1,2682	1,4633	0,4535
20	**0,12**	1,2065	0,7413	0,9729	0,2844	1,1116	0,7165	0,8716	0,2401
	0,17	1,4999	0,9014	1,1989	0,3433	1,3716	0,8691	1,0654	0,2880
	0,28	1,6998	1,0812	1,3891	0,4202	1,5834	1,0460	1,2557	0,3545
25	**0,12**	1,0899	0,6223	0,8529	0,2333	0,9838	0,5995	0,7496	0,1955
	0,17	1,3464	0,7531	1,0443	0,2808	1,2054	0,7237	0,9104	0,2340
	0,28	1,5502	0,9149	1,2300	0,3464	1,4131	0,8808	1,0885	0,2895
30	**0,12**	0,9868	0,5335	0,7539	0,1972	0,8760	0,5128	0,6533	0,1646
	0,17	1,2124	0,6437	0,9185	0,2370	1,0675	0,6173	0,7900	0,1967
	0,28	1,4154	0,7884	1,0958	0,2936	1,2669	0,7566	0,9542	0,2441
35	**0,12**	0,8967	0,4655	0,6723	0,1705	0,7857	0,4469	0,5768	0,1419
	0,17	1,0968	0,5606	0,8162	0,2047	0,9534	0,5369	0,6952	0,1695
	0,28	1,2953	0,6903	0,9831	0,2544	1,1424	0,6611	0,8458	0,2107
40	**0,12**	0,8186	0,4123	0,6048	0,1501	0,7100	0,3953	0,5150	0,1247
	0,17	0,9977	0,4958	0,7322	0,1801	0,8586	0,4743	0,6193	0,1489
	0,28	1,1893	0,6128	0,8884	0,2241	1,0366	0,5860	0,7575	0,1852
45	**0,12**	0,7509	0,3695	0,5484	0,1340	0,6460	0,3541	0,4644	0,1111
	0,17	0,9125	0,4440	0,6626	0,1606	0,7794	0,4245	0,5576	0,1326
	0,28	1,0961	0,5503	0,8085	0,2002	0,9463	0,5256	0,6847	0,1652
50	**0,12**	0,6921	0,3346	0,5010	0,1209	0,5917	0,3205	0,4224	0,1002
	0,17	0,8392	0,4018	0,6044	0,1449	0,7125	0,3839	0,5065	0,1196
	0,28	1,0143	0,4989	0,7406	0,1808	0,8690	0,4762	0,6238	0,1490

Table 14. Continues

L_t/h	V_{tcnt}	FGX				FGO			
		C-C	**S-S**	**C-S**	**C-F**	**C-C**	**S-S**	**C-S**	**C-F**
10	**0,12**	1,5475	1,2107	1,3599	0,5398	1,3078	0,9238	1,1106	0,3764
	0,17	1,9350	1,5013	1,6955	0,6622	1,6575	1,1405	1,3947	0,4581
	0,28	2,0860	1,6563	1,8424	0,7575	1,9072	1,3603	1,6252	0,5571
15	**0,12**	1,4106	1,0130	1,2043	0,4180	1,1459	0,7073	0,9261	0,2714
	0,17	1,7590	1,2432	1,4935	0,5079	1,4353	0,8606	1,1466	0,3272
	0,28	1,9091	1,4192	1,6491	0,6003	1,6784	1,0471	1,3621	0,4033
20	**0,12**	1,2969	0,8519	1,0730	0,3352	1,0034	0,5631	0,7795	0,2100
	0,17	1,6100	1,0378	1,3227	0,4051	1,2432	0,6800	0,9549	0,2520
	0,28	1,7714	1,2153	1,4886	0,4882	1,4755	0,8359	1,1510	0,3125
25	**0,12**	1,1930	0,7265	0,9588	0,2776	0,8820	0,4643	0,6656	0,1706
	0,17	1,4739	0,8807	1,1756	0,3345	1,0834	0,5585	0,8095	0,2043
	0,28	1,6466	1,0494	1,3470	0,4077	1,3010	0,6904	0,9855	0,2541
30	**0,12**	1,0976	0,6292	0,8605	0,2361	0,7807	0,3937	0,5772	0,1433
	0,17	1,3500	0,7603	1,0503	0,2839	0,9529	0,4723	0,6985	0,1714
	0,28	1,5305	0,9167	1,2220	0,3485	1,1544	0,5859	0,8561	0,2136
35	**0,12**	1,0111	0,5529	0,7765	0,2049	0,6969	0,3411	0,5076	0,1235
	0,17	1,2387	0,6666	0,9444	0,2461	0,8466	0,4086	0,6122	0,1476
	0,28	1,4230	0,8104	1,1125	0,3035	1,0323	0,5079	0,7539	0,1841
40	**0,12**	0,9335	0,4920	0,7049	0,1808	0,6273	0,3006	0,4520	0,1084
	0,17	1,1398	0,5922	0,8549	0,2170	0,7594	0,3597	0,5439	0,1295
	0,28	1,3245	0,7242	1,0171	0,2684	0,9304	0,4478	0,6719	0,1617
45	**0,12**	0,8643	0,4425	0,6437	0,1616	0,5691	0,2685	0,4067	0,0966
	0,17	1,0523	0,5321	0,7790	0,1939	0,6871	0,3211	0,4886	0,1154
	0,28	1,2349	0,6535	0,9342	0,2403	0,8450	0,4001	0,6051	0,1441
50	**0,12**	0,8028	0,4017	0,5912	0,1461	0,5201	0,2425	0,3694	0,0871
	0,17	0,9751	0,4827	0,7143	0,1751	0,6266	0,2898	0,4432	0,1040
	0,28	1,1538	0,5947	0,8621	0,2175	0,7728	0,3614	0,5498	0,1299

Tables 15 present the dimensionless frequency values for UD, FGA, FGX, and FGO beams with a slenderness ratio of $L_t/h = 5$, under different boundary conditions and volume fractions, and with varying CNT orientation angles (θ).

The results show that, for all beam types and support conditions, the dimensionless frequency values generally decrease as the CNT orientation angle (θ) increases from 0° to 90°, with the influence of CNT distributions diminishing as the angle approaches 45° and 90°. This convergence at higher angles suggests that altering the distribution of carbon nanotubes within the beam has a diminishing effect on the overall behavior.

The FGX beam consistently exhibits the highest $\overline{\omega}$ values, followed by the UD, FGA, and FGO beams in descending order. This is because the FGX distribution features a concentration of CNTs at the top and bottom surfaces of the beam, creating a gradient from the bottom to the top and forming a sandwich-like structure with stronger, stiffer outer layers. This results in a higher overall stiffness for the FGX beam.

The C-C support type consistently exhibits the highest $\overline{\omega}$ values, respected by the C-S, S-S, and C-F support types, due to the increased stiffness resulting from the greater constraint imposed by the C-C boundary condition.

Tables 16 present the dimensionless frequency values for UD, FGA, FGX, and FGO beams with a slenderness ratio of $L_t/h = 20$, under different boundary conditions and volume fractions, and with varying CNT orientation angles (θ).

The results show that, the dimensionless vertical displacement generally increases as the CNT orientation angle increases from 0° to 90°. This is because the stiffness of the beam in the vertical direction decreases as the CNTs become more aligned with the beam axis.

The FGX beam consistently exhibits the highest $\overline{\omega}$ values, followed by the UD, FGA, and FGO beams in descending order. This is because the FGX distribution features a concentration of CNTs at the top and bottom surfaces of the beam, creating a gradient from the bottom to the top and forming a sandwich-like structure with stronger, stiffer outer layers. This results in a higher overall stiffness for the FGX beam.

The C-C support type consistently exhibits the highest $\overline{\omega}$ values, respected by the C-S, S-S, and C-F support types, due to the increased stiffness resulting from the greater constraint imposed by the C-C boundary condition.

Table 15. Effect of CNT orientation angle on the first ϖ of UD, FGA, FGX and FGO beam with various boundary conditions and V_{tcnt} (L_t/h=5)

Boundary Condition	V_{tcnt}	**UD**			**FGA**		
		0°	**45°**	**90°**	**0°**	**45°**	**90°**
C-C	**0,12**	2,0738	1,1395	1,1188	2,0409	1,1393	1,1205
	0,17	2,6506	1,4803	1,4522	2,6044	1,4828	1,4573
	0,28	2,9432	1,5706	1,5362	2,9154	1,5901	1,5565
S-S	**0,12**	1,6425	0,5805	0,5656	1,6263	0,5813	0,5673
	0,17	2,0942	0,7536	0,7334	2,0719	0,7575	0,7384
	0,28	2,3309	0,7981	0,7740	2,3227	0,8189	0,7933
C-S	**0,12**	1,8268	0,8455	0,8271	1,7711	0,8452	0,8283
	0,17	2,3333	1,0980	1,0730	2,2551	1,0996	1,0768
	0,28	2,5918	1,1640	1,1337	2,5313	1,1783	1,1487
C-F	**0,12**	0,7725	0,2133	0,2076	0,7100	0,2132	0,2079
	0,17	0,9712	0,2769	0,2691	0,8848	0,2772	0,2701
	0,28	1,1120	0,2932	0,2839	1,0305	0,2968	0,2877
		FGX			**FGO**		
		0°	**45°**	**90°**	**0°**	**45°**	**90°**
C-C	**0,12**	2,1567	1,1569	1,1349	1,8131	1,1231	1,1058
	0,17	2,7348	1,5161	1,4854	2,3461	1,4514	1,4285
	0,28	2,9965	1,6531	1,6131	2,6797	1,5256	1,4965
S-S	**0,12**	1,7228	0,5958	0,5795	1,4285	0,5661	0,5537
	0,17	2,1897	0,7844	0,7615	1,8197	0,7273	0,7113
	0,28	2,3754	0,8671	0,8364	2,1196	0,7535	0,7344
C-S	**0,12**	1,9070	0,8629	0,8431	1,5976	0,8291	0,8136
	0,17	2,4209	1,1333	1,1055	2,0561	1,0683	1,0481
	0,28	2,6403	1,2438	1,2071	2,3649	1,1149	1,0901
C-F	**0,12**	0,8351	0,2194	0,2131	0,6365	0,2076	0,2028
	0,17	1,0500	0,2892	0,2802	0,7960	0,2664	0,2603
	0,28	1,1709	0,3205	0,3085	0,9476	0,2753	0,2680

Table 16. Effect of CNT orientation angle on the first ϖ of UD and FGA beam with various boundary conditions and V_{tcnt} (L_t/h=20)

Boundary Condition	V_{tcnt}	**UD**			**FGA**		
		0	**45**	**90**	**0**	**45**	**90**
C-C	**0,12**	1,3645	0,3440	0,3345	1,2323	0,3438	0,3350
	0,17	1,7062	0,4464	0,4336	1,5264	0,4470	0,4352
	0,28	1,9747	0,4726	0,4573	1,7965	0,4786	0,4635
S-S	**0,12**	0,7799	0,1536	0,1492	0,7521	0,1538	0,1497
	0,17	0,9518	0,1993	0,1934	0,9158	0,2004	0,1948
	0,28	1,1597	0,2110	0,2039	1,1179	0,2167	0,2092
C-S	**0,12**	1,0682	0,2386	0,2319	0,9393	0,2385	0,2323
	0,17	1,3217	0,3097	0,3007	1,1517	0,3101	0,3018
	0,28	1,5636	0,3278	0,3170	1,3813	0,3320	0,3214
C-F	**0,12**	0,2925	0,0548	0,0533	0,2453	0,0548	0,0534
	0,17	0,3547	0,0712	0,0691	0,2956	0,0712	0,0693
	0,28	0,4384	0,0753	0,0728	0,3663	0,0763	0,0738
		FGX			**FGO**		
		0	**45**	**90**	**0**	**45**	**90**
C-C	**0,12**	1,4954	0,3541	0,3436	1,1035	0,3345	0,3226
	0,17	1,8733	0,4667	0,4520	1,3691	0,4291	0,4190
	0,28	2,1075	0,5178	0,4980	1,6459	0-4430	0,4311
S-S	**0,12**	0,9117	0,1583	0,1535	0,5817	0,1492	0,1456
	0,17	1,1160	0,2087	0,2019	0,7047	0,1913	0,1866
	0,28	1,3362	0,2319	0,2228	0,8719	0,1972	0,1918
C-S	**0,12**	1,2024	0,2458	0,2384	0,8333	0,2319	0,2264
	0,17	1,4923	0,3241	0,3137	1,0222	0,2974	0,2903
	0,28	1,7206	0,3599	0,3458	1,2458	0,3068	0,2985
C-F	**0,12**	0,3486	0,0565	0,0548	0,2138	0,0533	0,0520
	0,17	0,4236	0,0745	0,0721	0,2577	0,0683	0,0666
	0,28	0,5182	0,0828	0,0796	0,3208	0,0704	0,0684

Figure 12 illustrates the variation in dimensionless frequency parameters of beams with respect to slenderness ratio, CNT distribution, and support type.

The outcomes indicate that the $\overline{\omega}$ decrease as the slenderness ratio increases. This is because a longer beam is less stiff than a shorter beam, and therefore it will vibrate at a lower frequency. The FGX beam consistently exhibits the highest $\overline{\omega}$, followed by the UD, FGA, and FGO beams in descending order. This is because the FGX distribution concentrates the CNTs at the bottom and top surfaces of the beam.

The C-C support type demonstrates the highest $\overline{\omega}$ values, respected by the C-S, S-S, and C-F support types. This is because the C-C support type provides the most constraint, which increases the stiffness and therefore the $\overline{\omega}$ values.

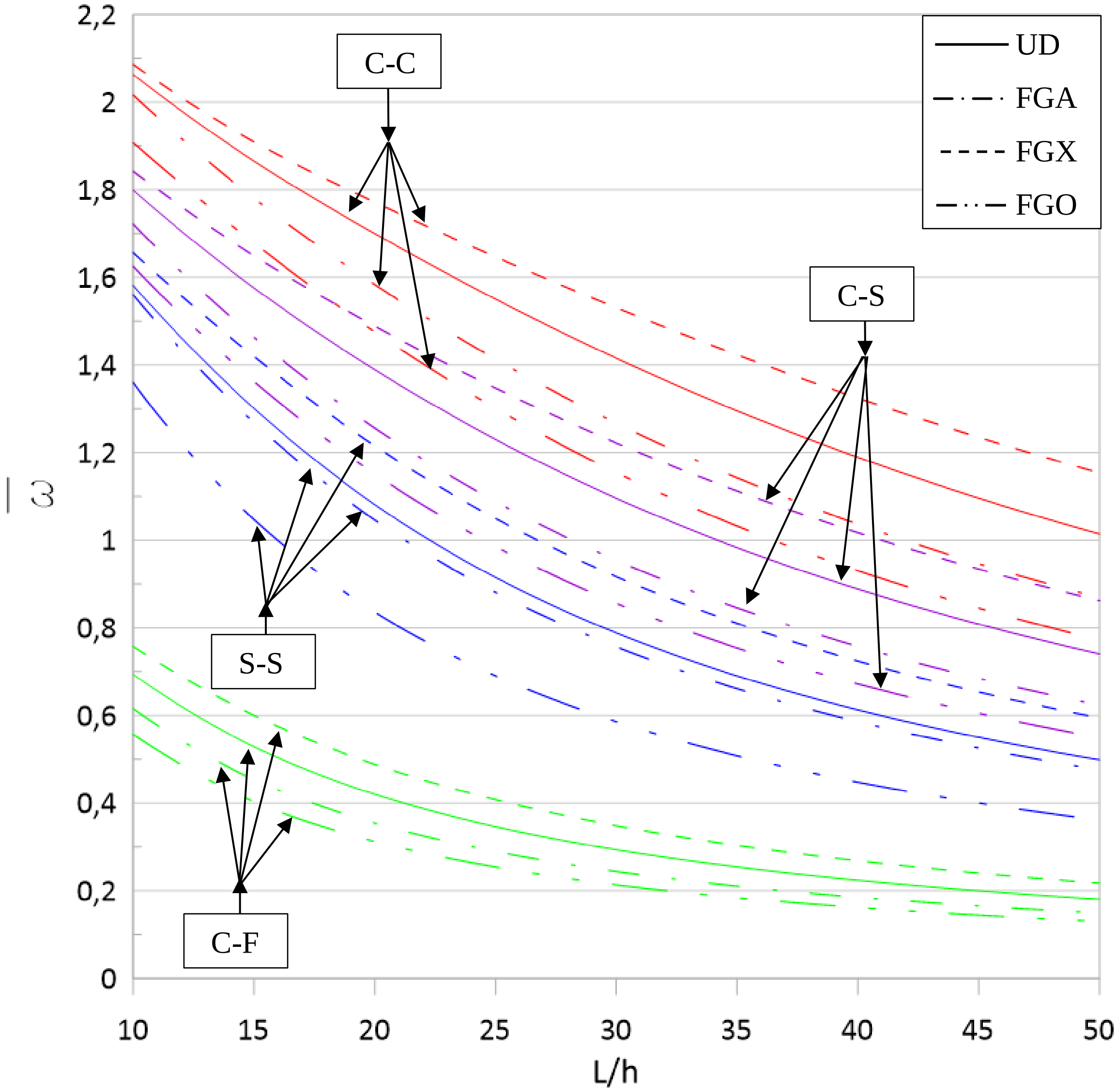

Figure 12. Dimensionless frequency parameters of beams with different slenderness ratios

Figures 13 to 16 depict the first mode shapes of UD, FGA, FGX, and FGO beams under free vibration analysis. In free vibration analysis, no external loading is applied; instead, the beam is subjected to a small initial displacement. The figures illustrate the effect of various boundary conditions and CNT distribution models on the modal behavior of the beams.

For all beam types, the C-C boundary condition exhibits the highest amplitude in the first mode shape, respected by C-S, S-S, and C-F boundary conditions. A stiffer beam, resulting from greater constraint, will vibrate with a larger amplitude in its first mode. It is noteworthy that the C-F beam does not exhibit zero deflection at the right end, as would be expected for a free end. This is because the free end is unconstrained and can therefore vibrate with a non-zero amplitude. In contrast, the other support types constrain the beam at both ends, forcing the amplitude to be zero at the boundaries.

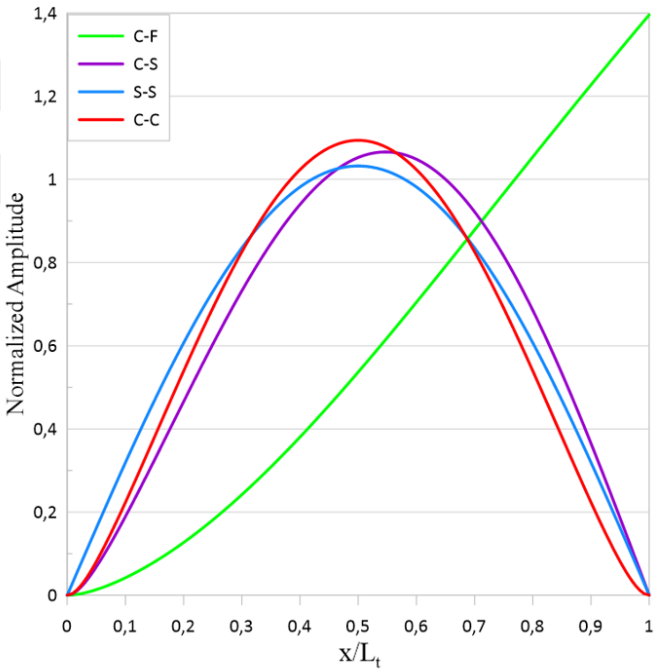

Figure 13. The dimensionless natural frequency first modes for UD beams under different boundary conditions ($V_{tcnt} = 0{,}28$)

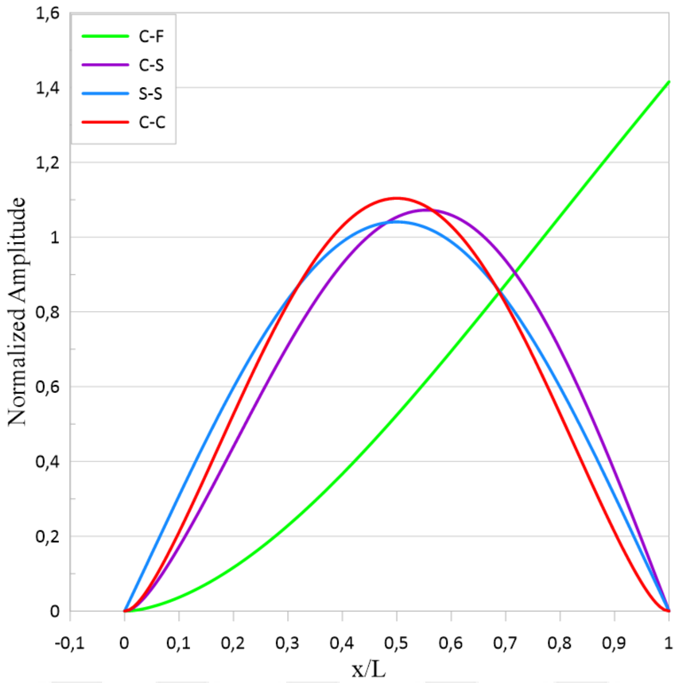

Figure 14. The dimensionless natural frequency first modes for FGA beams under different boundary conditions ($V_{tcnt} = 0{,}28$)

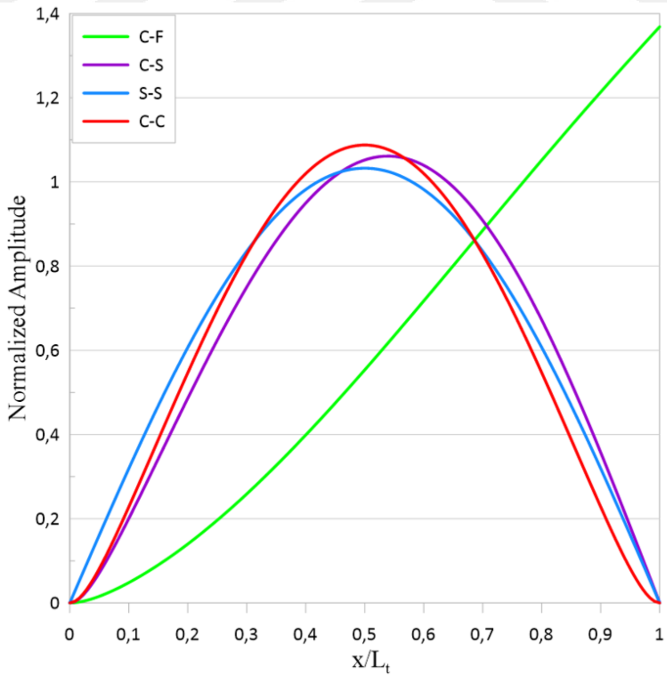

Figure 15. The dimensionless natural frequency first modes for FGX beams under different boundary conditions ($V_{tcnt} = 0{,}28$)

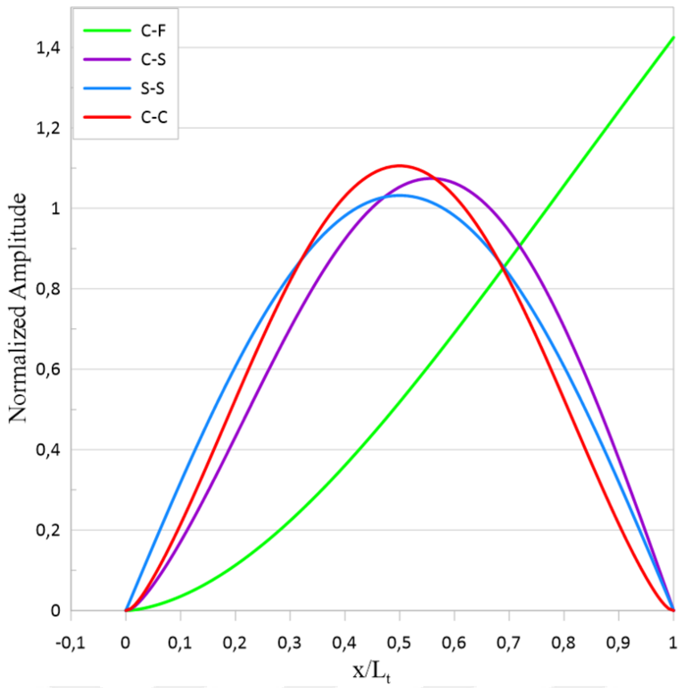

Figure 16. The dimensionless natural frequency first modes for FGO beams under different boundary conditions ($V_{tcnt} = 0{,}28$)

Figures 17 to 20 depict the first five non-dimensional free vibration mode shapes for UD, FGA, FGX, and FGO beams, respectively, under different boundary conditions and a constant $V_{cnt} = 0{,}12$. Each figure illustrates the effect of boundary condition on the modal behavior of a single beam.

The first mode shape, which corresponds to the lowest natural frequency, typically exhibits the entire beam vibrating in the same direction. However, the higher mode shapes can differ depending on the boundary condition and CNT distribution pattern.

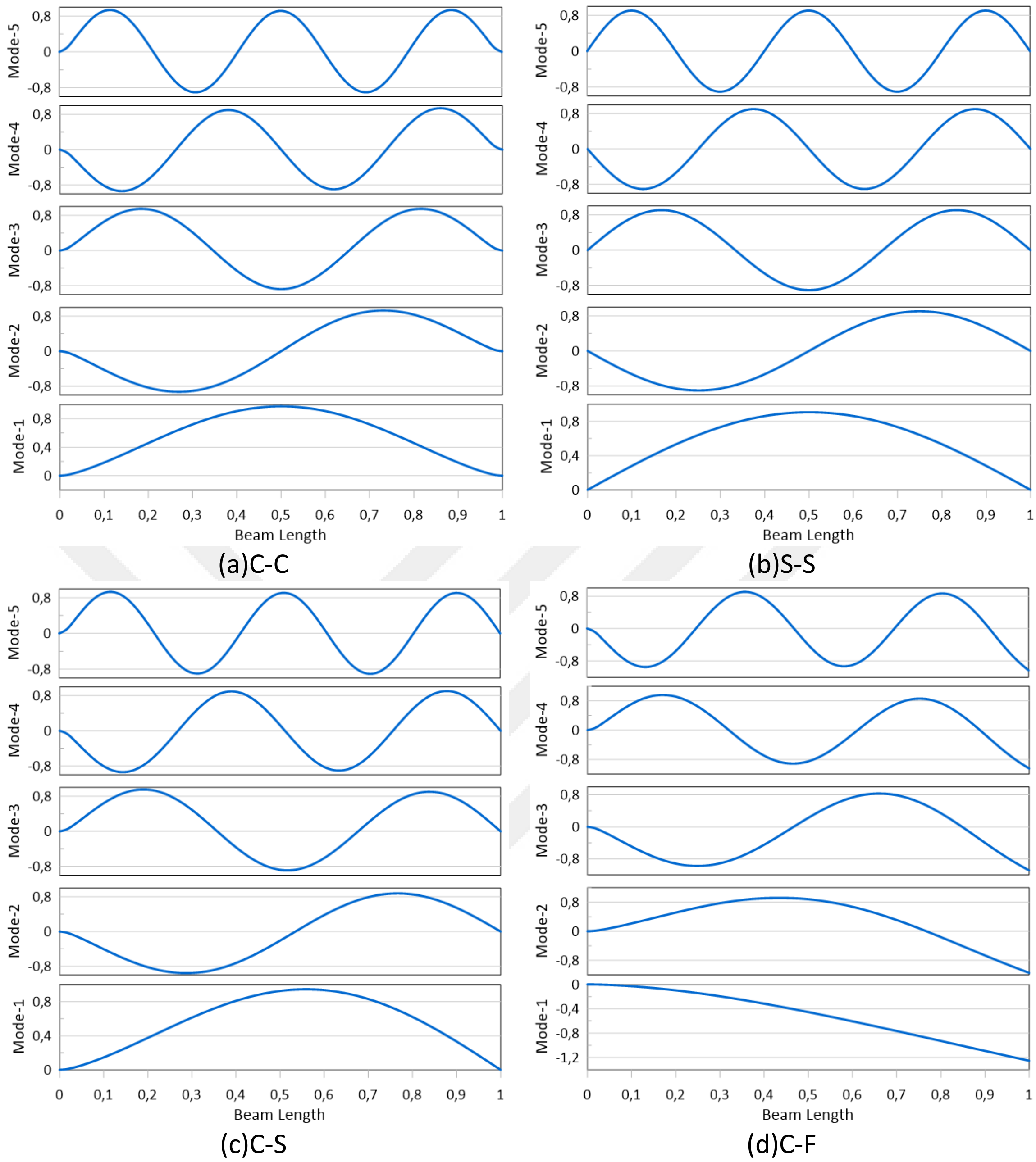

Figure 17. First five free vibration modes for UD beam different boundary condition type (L_t/h=20 and $V_{tcnt} = 0{,}12$)

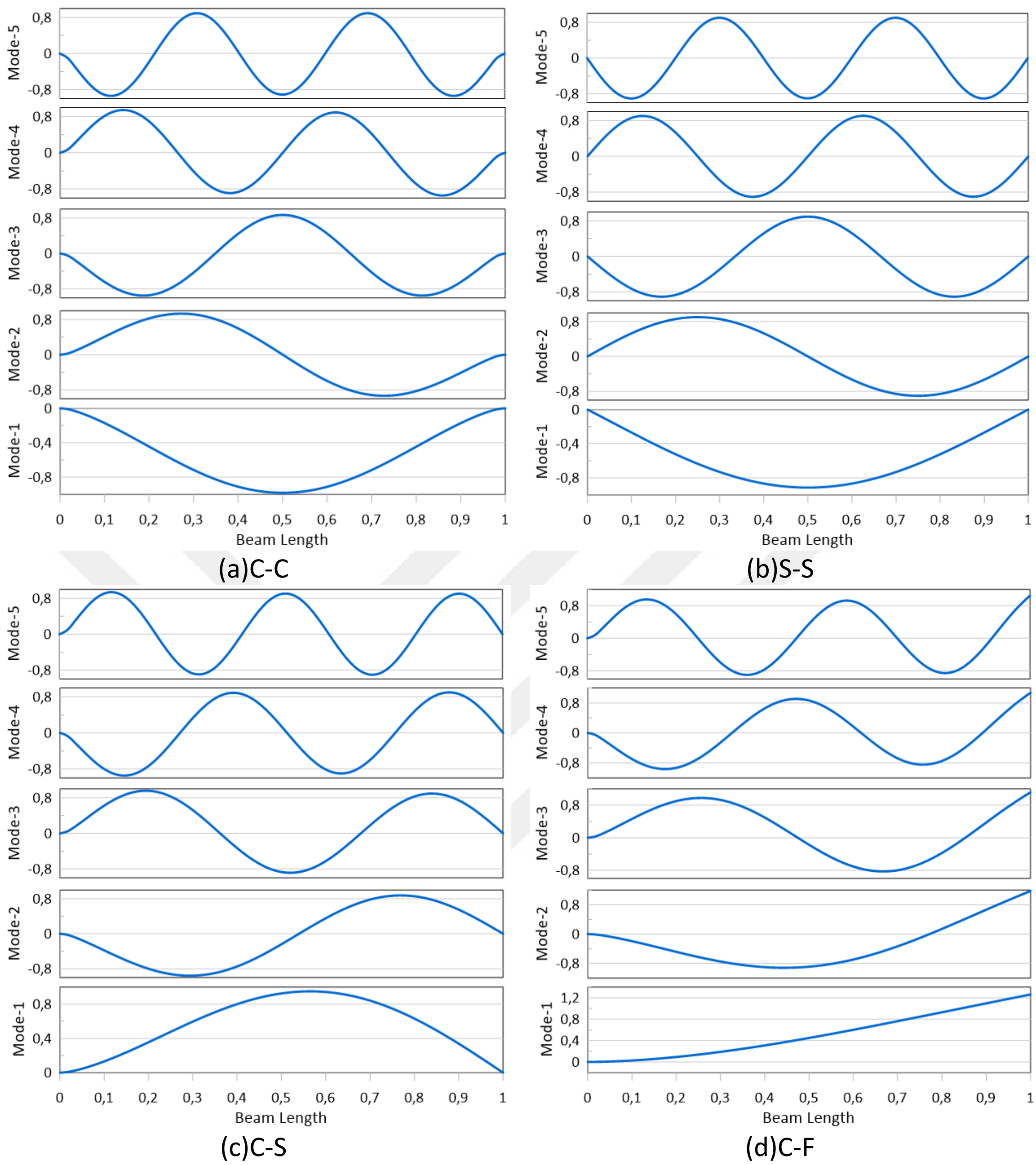

Figure 18. First five free vibration modes for FGA beam different boundary condition (L_t/h=20 and $V_{tcnt} = 0{,}12$)

For example, Figure 19 shows the first five buckling modes for a UD beam under C-C, C-S, S-S, and C-F boundary conditions. The first mode shape for all boundary conditions is a single half-sine wave, with the maximum deflection occurring at the midpoint of the beam. However, the higher mode shapes differ depending on the boundary condition. For example, the second mode shape for the C-C beam is a full sine wave, while the second mode shape for the C-F beam is a single half-sine wave with the maximum deflection occurring at the free end.

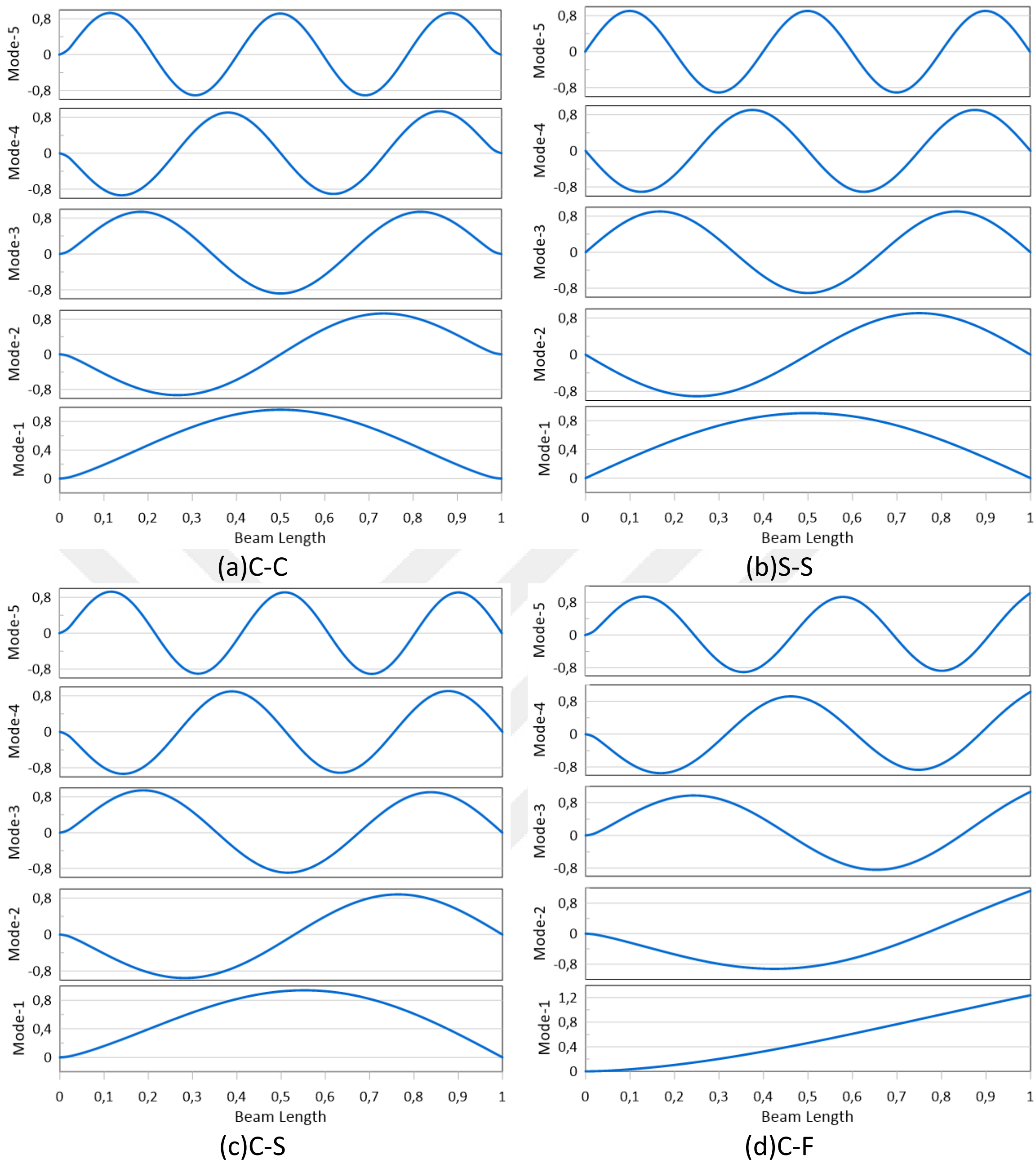

Figure 19. First five free vibration modes for FGX beam different boundary condition (L_t/h=20 and $V_{tcnt} = 0{,}12$)

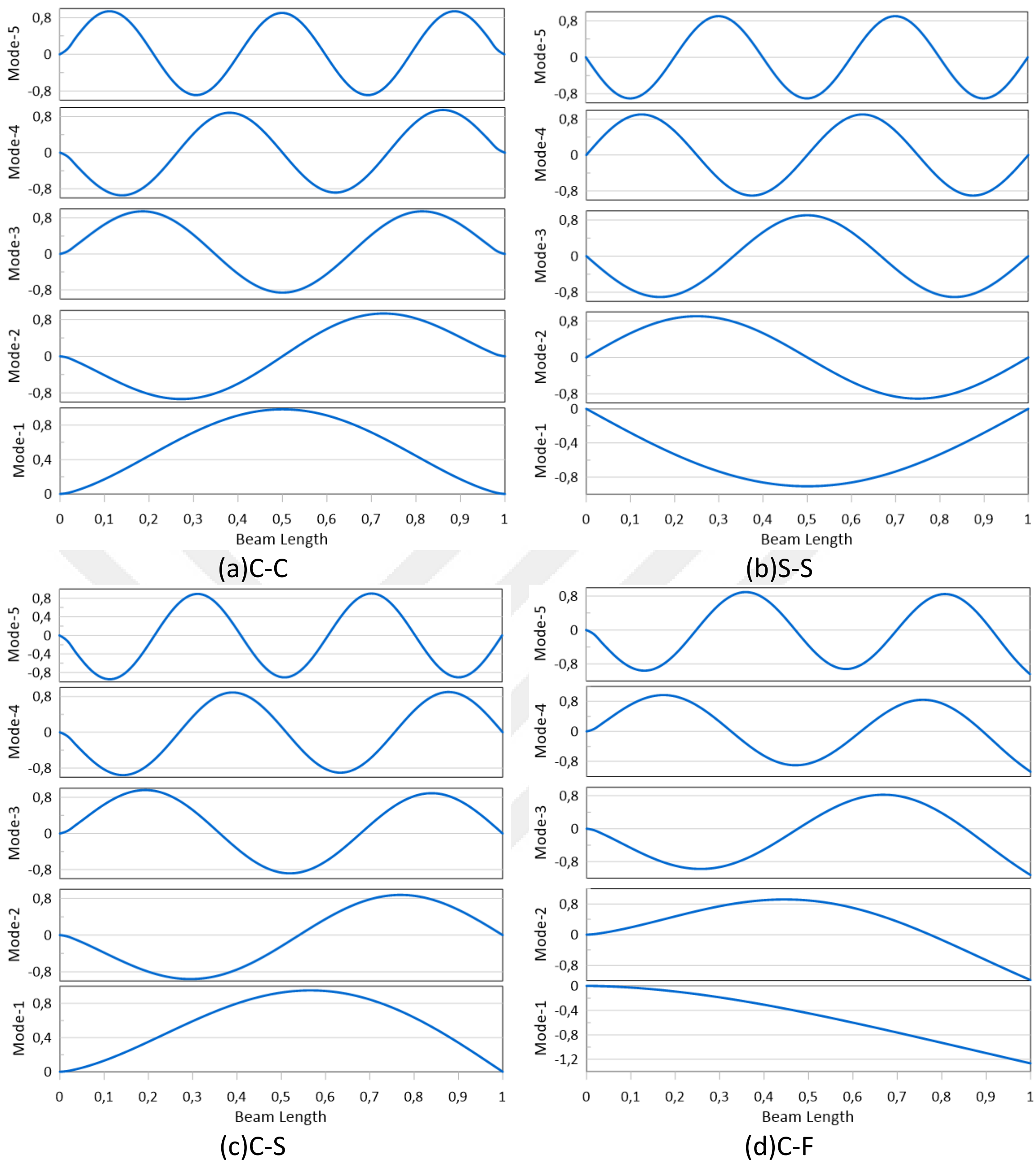

Figure 20. First five free vibration modes for FGO beam different boundary condition (L_t/h=20 and $V_{tcnt} = 0{,}12$)

3.3.2. Bending Analysis

Bending analysis of beams is crucial for structural engineering, enabling engineers to predict and optimize beam behavior under various loading conditions. By understanding bending stresses and deflections, engineers ensure structures can safely withstand applied loads. Key reasons for conducting bending analysis include ensuring structural safety, optimizing material usage, predicting and mitigating structural vibrations, understanding composite beam behavior, evaluating boundary condition effects, and informing design decisions.

Table 17 compares the mid deflections attained from the present study with the outcomes reported by Kumar and Srinivas (2017b) (K. & S.), who employed TBT and the principle of virtual work to derive the governing equations of motion for the beams and subsequently utilized the FEM to solve the equations and acquire numerical results for the bending deflections. The analysis specifically focused on the C-C boundary condition. As a result, it was observed that the calculations converged successfully. The FGX beam had the highest deflection value, while it was also observed that the deflection decreases as the slenderness of the beam increases. Notably, the FGX beam demonstrated the greatest reduction in deflection.

Table 17. Comparison dimensionless mid deflection of FG-CNTRC beam (Material Properties B and C-C at $\theta = 0$)

L_t/h	V_{tcnt}	UD		FGA		FGX		FGO	
		K. & S.	**Present**	**K. & S.**	**Present**	**K. & S.**	**Present**	**K. & S.**	**Present**
15	**0,12**	0,2184	0,2087	0,2513	0,2440	0,1941	0,1811	0,2864	0,2997
	0,17	0,1349	0,1301	0,1574	0,1546	0,1177	0,1129	0,1815	0,1887
	0,28	0,1044	0,0987	0,1162	0,1134	0,0911	0,0906	0,1312	0,1317
20	**0,12**	0,1548	0,1524	0,1879	0,1876	0,1307	0,1262	0,2231	0,2344
	0,17	0,0976	0,0968	0,1206	0,1214	0,0809	0,0799	0,1448	0,1513
	0,28	0,0723	0,0706	0,0855	0,0857	0,0604	0,0619	0,1006	0,1025
30	**0,12**	0,1092	0,1106	0,1427	0,1460	0,0855	0,0854	0,1778	0,1869
	0,17	0,0710	0,0723	0,0944	0,0970	0,0546	0,0554	0,1185	0,1242
	0,28	0,0494	0,0498	0,0636	0,0653	0,0385	0,0400	0,0787	0,0813

Table 18 presents a comparison of the beam's displacement, normal stress, and shear stress in the homogeneous state with previously published Table 20. The findings demonstrate that the results are similar and comparable to those from prior studies. Wattanasakulpong and Ungbhakorn (2013) (W. & U.) employed various shear deformation theories to model the deformation of the beam and the Navier solution method to obtain analytical solutions for the deflections and stresses.

Table 19 compares the dimensionless displacements and stresses for isotropic and FG beams subjected to a uniform load. The table shows that the different shear deformation theories yield similar results for the vertical displacement ($\bar{w}$) and normal stress ($\bar{\sigma}_{xx}$). However, the shear stress ($\bar{\sigma}_{xz}$) values predicted by the different theories vary more significantly. The ESDT predicts the highest shear stress, while the HSDT predicts the lowest shear stress. The results from the two studies are in good agreement, which validates the accuracy of the present study.

Table 18. Comparisons of displacements and stresses for isotropic and FG beams subjected to uniform load (L_t/h = 20 and $\theta = 0$)

	$\bar{w}$	$\bar{\sigma}_{xx}$	$\bar{\sigma}_{xz}$
Present Study	2,8963	15,0130	0.7482
W. & U.	2,8963	15,0133	0.7427
W. & U. (TSDT)	2,8962	15,0148	0.7896
W. & U. (ESDT)	2,8962	15,0131	0.7402
W. & U. (HSDT)	2,8962	15,0139	0.7660
W. & U. (TSDT)	2,8962	15,0129	0.7451

Table 19 compares the displacement and stress results obtained in the present study with those reported by Wattanasakulpong and Ungbhakorn (2013), whose work is widely referenced as pioneering in this field. The evaluation of $\bar{w}, \bar{\sigma}_{xx}, and\ \bar{\sigma}_{xz}$ was conducted using the S-S support system, and consequently, the present results are expected to exhibit proximity to their findings. Comparison reveals a high level of agreement between the measured values, demonstrating a minimal margin of error. It is once again observed that the values decrease as the slenderness of the beam increases because a more slender beam is less stiff and therefore more prone to deformation.

Table 19. Dimensionless displacements and stresses of UD beams $\bar{w}, \bar{\sigma}_{xx}, and\ \bar{\sigma}_{xz}$ under uniform loads (S-S and $\theta = 0$)

L_t/h	V_{tcnt}	$\bar{w}$		$\bar{\sigma}_{xx}$		$\bar{\sigma}_{xz}$	
		W. & U.	**Present**	**W. & U.**	**Present**	**W. & U.**	**Present**
15	**0,12**	0,7040	0,7040	8,3990	8,3982	0,7010	0,7011
	0,17	0,5240	0,5240	11,8490	11,8488	0,7160	0,7177
	0,28	0,4610	0,4610	15,4480	15,4491	0,7250	0,7262
20	**0,12**	0,4490	0,4490	8,2670	8,2679	0,7040	0,7048
	0,17	0,3440	0,3440	11,7620	11,7619	0,7190	0,7202
	0,28	0,3070	0,3070	15,3840	15,3839	0,7260	0,7281
30	**0,12**	0,3250	0,3250	8,5620	8,56215	0,6970	0,6967
	0,17	0,2350	0,2350	11,9590	11,9581	0,7140	0,7147
	0,28	0,2030	0,2030	15,5300	15,5310	0,7230	0,7239

Tables 20 present the maximum dimensionless vertical displacement ($\bar{w}$) for beams with different slenderness ratios, boundary conditions, and CNT distributions. As the slenderness ratio increases, the maximum displacement values decrease for all beam types and boundary conditions.

The peak displacement value of $\bar{w}$ is observed for the C-F boundary condition, followed by the S-S, C-S, and C-C boundary conditions in descending order. This is because the C-F boundary condition provides the least constraint, which results in the lowest stiffness and therefore the highest displacement.

Among the different CNT distributions, the FGO beam consistently exhibits the highest maximum displacement values, followed by the FGA, UD, and FGX beams in descending order. This can be explained by the distribution of CNTs within the beam. The FGO distribution concentrates the CNTs at the top surface of the beam, while the FGA distribution concentrates the CNTs at the bottom surface. This results in a lower overall stiffness compared to the UD and FGX distributions, which distribute the CNTs more evenly throughout the beam or concentrate them at the top and bottom surfaces, respectively. The FGX distribution, with its concentration of CNTs at the top and bottom surfaces, provides the highest stiffness and therefore the lowest displacement.

Table 20. The maximum displacement ($\overline{\mathrm{w}}$) values of UD ,FGA,FGX and FGO beams under different slenderness ratios, boundary and volume fractions ($\theta = 0$)

L_t/h	V_{tcnt}	UD				FGA			
		C-C	**S-S**	**C-S**	**C-F**	**C-C**	**S-S**	**C-S**	**C-F**
10	**0,12**	0,3606	0,7047	0,4963	4,7506	0,3957	0,7410	0,5714	6,3911
	0,17	0,2201	0,4498	0,3076	3,1295	0,2444	0,4751	0,3596	4,2793
	0,28	0,1739	0,3253	0,2358	2,116	0,1875	0,3395	0,2670	2,8374
15	**0,12**	0,2087	0,525	0,3149	4,0822	0,2439	0,5615	0,3885	5,7237
	0,17	0,1301	0,3445	0,2002	2,7363	0,1546	0,3703	0,2516	3,8877
	0,28	0,0987	0,2349	0,1458	1,7817	0,1134	0,2507	0,1775	2,5085
20	**0,12**	0,1524	0,4617	0,2478	3,8421	0,1876	0,4983	0,3211	5,4839
	0,17	0,0968	0,3075	0,1606	2,5954	0,1215	0,3335	0,2120	3,7473
	0,28	0,0706	0,2031	0,1124	1,6614	0,0858	0,2194	0,1444	2,3901
25	**0,12**	0,1255	0,4323	0,2159	3,7294	0,1608	0,4690	0,2895	5,3714
	0,17	0,0810	0,2903	0,1419	2,5293	0,1057	0,3164	0,1935	3,6816
	0,28	0,0572	0,1883	0,0964	1,6048	0,0726	0,2048	0,1287	2,3346
30	**0,12**	0,1106	0,4163	0,1985	3,6677	0,0854	0,2925	0,1465	2,5211
	0,17	0,0723	0,281	0,1317	2,4932	0,0554	0,1966	0,0966	1,7093
	0,28	0,0498	0,1802	0,0877	1,5738	0,0401	0,1287	0,0668	1,0900
35	**0,12**	0,1016	0,4067	0,1879	3,6303	0,0765	0,2830	0,1361	2,4842
	0,17	0,0669	0,2753	0,1255	2,4713	0,0501	0,1909	0,0904	1,6873
	0,28	0,0452	0,1754	0,0823	1,555	0,0353	0,1235	0,0612	1,0703
40	**0,12**	0,0957	0,4004	0,1809	3,606	0,0707	0,2768	0,1293	2,4602
	0,17	0,0635	0,2717	0,1214	2,457	0,0466	0,1872	0,0863	1,6729
	0,28	0,0423	0,1722	0,0789	1,5428	0,0322	0,1202	0,0576	1,0574
45	**0,12**	0,0916	0,3961	0,1762	3,5892	0,0667	0,2726	0,1246	2,4436
	0,17	0,0611	0,2692	0,1186	2,4472	0,0442	0,1847	0,0835	1,6631
	0,28	0,0402	0,17	0,0765	1,5343	0,0301	0,1180	0,0551	1,0486
50	**0,12**	0,0886	0,393	0,1728	3,5772	0,0638	0,2695	0,1213	2,4318
	0,17	0,0593	0,2674	0,1166	2,4402	0,0425	0,1829	0,0815	1,6560
	0,28	0,0387	0,1685	0,0747	1,5283	0,0286	0,1163	0,0533	1,0423

Table 20. Continues

L_t/h	V_{tcnt}	FGX				FGO			
		C-C	**S-S**	**C-S**	**C-F**	**C-C**	**S-S**	**C-S**	**C-F**
10	**0,12**	0,3277	0,5771	0,4349	3,5826	0,4797	1,1015	0,6983	8,2604
	0,17	0,2015	0,3664	0,2704	2,3450	0,2923	0,7157	0,4359	5,5276
	0,28	0,1670	0,2808	0,2181	1,6536	0,2122	0,4810	0,3074	3,5854
15	**0,12**	0,1811	0,3999	0,2600	2,9284	0,2997	0,9014	0,4856	7,4984
	0,17	0,1129	0,2606	0,1648	1,9529	0,1887	0,6017	0,3136	5,0919
	0,28	0,0906	0,1861	0,1267	1,3068	0,1317	0,3914	0,2123	3,2444
20	**0,12**	0,1262	0,3374	0,1949	2,6926	0,2345	0,8311	0,4086	7,2273
	0,17	0,0799	0,2233	0,1256	1,8118	0,1514	0,5618	0,2696	4,9372
	0,28	0,0617	0,1527	0,0924	1,1814	0,1025	0,3600	0,1779	3,1231
25	**0,12**	0,1000	0,3083	0,1638	2,5818	0,2038	0,7986	0,3729	7,1008
	0,17	0,0641	0,2060	0,1069	1,7456	0,1338	0,5433	0,2492	4,8650
	0,28	0,0478	0,1371	0,0759	1,1224	0,0888	0,3454	0,1619	3,0665
30	**0,12**	0,0854	0,2925	0,1465	2,5211	0,1870	0,7809	0,3532	7,0318
	0,17	0,0554	0,1966	0,0966	1,7093	0,1242	0,5332	0,2380	4,8257
	0,28	0,0401	0,1287	0,0668	1,0900	0,0813	0,3375	0,1531	3,0357
35	**0,12**	0,0765	0,2830	0,1361	2,4842	0,1767	0,7703	0,3413	6,9900
	0,17	0,0501	0,1909	0,0904	1,6873	0,1184	0,5271	0,2312	4,8019
	0,28	0,0353	0,1235	0,0612	1,0703	0,0767	0,3327	0,1478	3,0170
40	**0,12**	0,0707	0,2768	0,1293	2,4602	0,1701	0,7633	0,3336	6,9629
	0,17	0,0466	0,1872	0,0863	1,6729	0,1146	0,5232	0,2268	4,7865
	0,28	0,0322	0,1202	0,0576	1,0574	0,0737	0,3296	0,1443	3,0048
45	**0,12**	0,0667	0,2726	0,1246	2,4436	0,1655	0,7586	0,3283	6,9442
	0,17	0,0442	0,1847	0,0835	1,6631	0,1119	0,5205	0,2237	4,7758
	0,28	0,0301	0,1180	0,0551	1,0486	0,0717	0,3275	0,1419	2,9965
50	**0,12**	0,0638	0,2695	0,1213	2,4318	0,1622	0,7552	0,3244	6,9309
	0,17	0,0425	0,1829	0,0815	1,6560	0,1101	0,5186	0,2216	4,7682
	0,28	0,0286	0,1163	0,0533	1,0423	0,0702	0,3260	0,1402	2,9905

Table 21 presents the maximum dimensionless normal stress ($\bar{\sigma}_{xx}$) for beams with different slenderness ratios, boundary conditions, and CNT distributions. As the slenderness ratio increases, the maximum normal stress values increase for all beam types and boundary conditions. This is because a slenderer beam is less stiff and therefore more prone to deformation, which results in higher stresses.

The peak normal stress value of $\bar{\sigma}_{xx}$ is observed for the C-F boundary condition, followed by the S-S, C-S, and C-C boundary conditions in descending order. This is because the C-F boundary condition provides the least constraint, which results in the lowest stiffness and therefore the highest stresses.

Among the different CNT distributions, the FGX beam consistently exhibits the lowest maximum normal stress values, followed by the UD, FGO, and FGA beams in ascending order. This can be explained by the distribution of CNTs within the beam. The FGX distribution concentrates the CNTs at the top and bottom surfaces of the beam, which are the regions that experience the most stress during bending. This increases the stiffness of the beam in the direction of bending, which in turn reduces the stresses. In contrast, the FGO and FGA distributions concentrate the CNTs at the top and bottom surfaces of the beam, respectively, which results in a lower overall stiffness and therefore higher stresses. The UD distribution, which distributes the CNTs evenly throughout the beam, has an intermediate stiffness and therefore intermediate stress values.

Table 21. The maximum normal stress ($\overline{\sigma}_{xx}$) values of UD,FGA,FGX and FGO beams under different slenderness ratios, boundary and volume fractions ($\theta = 0$)

L_t/h	V_{tcnt}	UD				FGA			
		C-C	**S-S**	**C-S**	**C-F**	**C-C**	**S-S**	**C-S**	**C-F**
10	**0,12**	16,3078	8,3982	19,9545	53,5138	0,5086	0,2607	0,6439	1,9775
	0,17	15,3467	8,2679	18,9694	51,4613	0,3117	0,1655	0,3993	1,2412
	0,28	17,4073	8,5622	21,0711	55,8768	0,2137	0,1060	0,2680	0,8165
15	**0,12**	17,9614	11,8488	23,1340	66,5215	0,6051	0,3730	0,8079	2,6325
	0,17	16,9606	11,7619	22,0516	64,4331	0,3735	0,2384	0,5036	1,6637
	0,28	19,1183	11,9581	24,3721	68,9447	0,2532	0,1507	0,3354	1,0816
20	**0,12**	19,5243	15,4491	26,0032	79,4977	0,6995	0,4889	0,9637	3,2868
	0,17	18,5330	15,3840	24,8951	77,4499	0,4346	0,3133	0,6037	2,0870
	0,28	20,6819	15,5311	27,2862	81,8949	0,2914	0,1970	0,3987	1,3457
25	**0,12**	21,1460	19,1093	28,8377	92,6513	0,7952	0,6063	1,1181	3,9454
	0,17	20,1886	19,0572	27,7466	90,6844	0,4971	0,3889	0,7037	2,5137
	0,28	22,2743	19,1749	30,1154	94,9735	0,3299	0,2439	0,4611	1,6111
30	**0,12**	22,8644	22,7994	31,7336	106,0282	0,8934	0,7243	1,2739	4,6095
	0,17	21,9519	22,7560	30,6808	104,1598	0,5613	0,4650	0,8049	2,9442
	0,28	23,9484	22,8541	32,9780	108,2509	0,3692	0,2913	0,5238	1,8786
35	**0,12**	24,6814	26,5066	34,7175	119,6194	0,9939	0,8428	1,4316	5,2789
	0,17	23,8175	26,4694	33,7126	117,8545	0,6271	0,5412	0,9076	3,3782
	0,28	25,7147	26,5535	35,9146	121,7329	0,4094	0,3388	0,5872	2,1480
40	**0,12**	26,5876	30,2246	37,7907	133,3998	1,0967	0,9616	1,5914	5,9528
	0,17	25,7723	30,1920	36,8368	131,7366	0,6942	0,6176	1,0116	3,8150
	0,28	27,5686	30,2655	38,9346	135,4027	0,4505	0,3864	0,6513	2,4193
45	**0,12**	28,5711	33,9496	40,9456	147,3417	1,2013	1,0805	1,7531	6,6307
	0,17	27,8024	33,9206	40,0425	145,7754	0,7626	0,6941	1,1168	4,2543
	0,28	29,5006	33,9860	42,0347	149,2372	0,4923	0,4341	0,7162	2,6921
50	**0,12**	30,6202	37,6796	44,1724	161,4201	1,3075	1,1995	1,9164	7,3118
	0,17	29,8953	37,6536	43,3180	159,9443	0,8319	0,7707	1,2231	4,6957
	0,28	31,5006	37,7124	45,2076	163,2137	0,5348	0,4819	0,7818	2,9664

Table 21. Continues

L_t/h	V_{tcnt}	FGX				FGO			
		C-C	**S-S**	**C-S**	**C-F**	**C-C**	**S-S**	**C-S**	**C-F**
10	**0,12**	23,6184	11,4272	28,1117	75,2105	0,8294	0,3864	1,0430	2,6345
	0,17	22,4019	11,2388	26,9107	72,5942	0,4925	0,2453	0,6257	1,6099
	0,28	25,8136	11,8028	30,2662	79,9614	0,3433	0,1559	0,4306	1,0794
15	**0,12**	25,9199	15,8914	32,6050	92,5509	0,8643	0,5522	1,1350	3,1648
	0,17	24,6327	15,7684	31,2687	89,8613	0,5156	0,3533	0,6837	1,9540
	0,28	28,2635	16,1342	35,0045	97,4582	0,3561	0,2224	0,4665	1,2900
20	**0,12**	27,9957	20,6054	36,5508	109,6898	0,9115	0,7236	1,2328	3,7251
	0,17	26,7015	20,5159	35,1533	107,0223	0,5486	0,4643	0,7488	2,3207
	0,28	30,3731	20,7796	39,0850	114,5885	0,3739	0,2912	0,5046	1,5130
25	**0,12**	30,0928	25,4194	40,3428	126,9712	0,9722	0,8971	1,3436	4,3149
	0,17	28,8262	25,3506	38,9403	124,3822	0,5909	0,5764	0,8234	2,7071
	0,28	32,4397	25,5506	42,9135	131,7583	0,3975	0,3609	0,5481	1,7482
30	**0,12**	32,2889	30,2834	44,1514	144,5007	1,1250	1,2469	1,5994	5,5596
	0,17	31,0680	30,2290	42,7773	142,0200	0,6950	0,8021	0,9947	3,5207
	0,28	34,5689	30,3844	46,6940	149,1160	0,4575	0,5015	0,6493	2,2459
35	**0,12**	34,6027	35,1760	48,0413	162,2940	1,1250	1,2469	1,5994	5,5596
	0,17	33,4359	35,1322	46,7136	159,9349	0,6950	0,8021	0,9947	3,5207
	0,28	36,7964	35,2540	50,5180	166,7065	0,4575	0,5015	0,6493	2,2459
40	**0,12**	37,0308	40,0864	52,0316	180,3338	1,2125	1,4225	1,7399	6,2048
	0,17	35,9210	40,0510	50,7591	178,0997	0,7538	0,9154	1,0881	3,9414
	0,28	39,1296	40,1461	54,4217	184,5305	0,4922	0,5721	0,7052	2,5043
45	**0,12**	39,5622	45,0087	56,1226	198,5922	1,3052	1,5984	1,8865	6,8607
	0,17	38,5092	44,9802	54,9085	196,4811	0,8157	1,0288	1,1850	4,3682
	0,28	41,5637	45,0532	58,4159	202,5714	0,5290	0,6428	0,7637	2,7671
50	**0,12**	42,1844	49,9393	60,3069	217,0404	1,4019	1,7745	2,0379	7,5248
	0,17	41,1862	49,9166	59,1514	215,0474	0,8798	1,1423	1,2848	4,7998
	0,28	44,0897	49,9707	62,4999	220,8066	0,5675	0,7136	0,8241	3,0334

Tables 22 present the maximum dimensionless shear stress ($\bar{\sigma}_{xz}$) for beams with different slenderness ratios, boundary conditions, and CNT distributions. As the slenderness ratio increases, the maximum shear stress values increase for all beam types and boundary conditions. This is because a slenderer beam is less stiff and therefore more prone to deformation, which results in higher stresses.

The peak shear stress value of $\bar{\sigma}_{xz}$ is observed for the C-F boundary condition, followed by the S-S, C-S, and C-C boundary conditions in descending order. This is because the C-F boundary condition provides the least constraint, which results in the lowest stiffness and therefore the highest stresses.

Among the different CNT distributions, the FGO beam consistently exhibits the highest maximum shear stress values, followed by the FGA, UD, and FGX beams in descending order. This can be explained by the distribution of CNTs within the beam. The FGO distribution concentrates the CNTs at the top surface of the beam, while the FGA distribution concentrates the CNTs at the bottom surface. This results in a lower overall stiffness compared to the UD and FGX distributions, which distribute the CNTs more evenly throughout the beam or concentrate them at the top and bottom surfaces, respectively. The FGX distribution, with its concentration of CNTs at the top and bottom surfaces, provides the highest stiffness and therefore the lowest shear stress. It is noteworthy that the FGA and UD distributions exhibit similar maximum shear stress values, with the FGA distribution being slightly higher.

Table 22. The maximum shear stress ($\overline{\sigma}_{xz}$) values of UD,FGA,FGX and FGO beams under different slenderness ratios, boundary and volume fractions ($\theta = 0$)

L_t/h	V_{tcnt}	UD				FGA			
		C-C	**S-S**	**C-S**	**C-F**	**C-C**	**S-S**	**C-S**	**C-F**
10	**0,12**	0,5643	0,7011	0,7106	1,2786	0,5657	0,7022	0,7211	1,2817
	0,17	0,5720	0,7048	0,7234	1,2940	0,5750	0,7076	0,7355	1,3007
	0,28	0,5546	0,6968	0,6950	1,2591	0,5649	0,7074	0,7180	1,2821
15	**0,12**	0,5950	0,7177	0,7591	1,3329	0,5966	0,7186	0,7659	1,3357
	0,17	0,6067	0,7202	0,7641	1,3376	0,6102	0,7227	0,7725	1,3438
	0,28	0,5881	0,7148	0,7524	1,3263	0,5979	0,7250	0,7712	1,3481
20	**0,12**	0,6296	0,7262	0,7956	1,3445	0,6311	0,7269	0,8005	1,3471
	0,17	0,6350	0,7282	0,8036	1,3457	0,6382	0,7303	0,8104	1,3518
	0,28	0,6219	0,7240	0,7844	1,3425	0,6330	0,7338	0,8022	1,3637
25	**0,12**	0,6406	0,7315	0,8126	1,3562	0,6419	0,7320	0,8164	1,3589
	0,17	0,6414	0,7331	0,8146	1,3578	0,6443	0,7350	0,8201	1,3639
	0,28	0,6380	0,7296	0,8083	1,3511	0,6485	0,7391	0,8242	1,3731
30	**0,12**	0,6404	0,7351	0,8143	1,3558	0,6415	0,7354	0,8173	1,3582
	0,17	0,6382	0,7364	0,8123	1,3514	0,6409	0,7381	0,8170	1,3570
	0,28	0,6414	0,7335	0,8148	1,3578	0,6513	0,7427	0,8292	1,3787
35	**0,12**	0,6351	0,7377	0,8090	1,3458	0,6362	0,7379	0,8115	1,3483
	0,17	0,6312	0,7389	0,8046	1,3449	0,6337	0,7404	0,8088	1,3508
	0,28	0,6385	0,7363	0,8126	1,3519	0,6479	0,7452	0,8260	1,3719
40	**0,12**	0,6280	0,7397	0,8009	1,3441	0,6289	0,7397	0,8031	1,3466
	0,17	0,6230	0,7407	0,7951	1,3428	0,6254	0,7420	0,7990	1,3487
	0,28	0,6327	0,7385	0,8063	1,3452	0,6418	0,7471	0,8190	1,3659
45	**0,12**	0,6203	0,7412	0,7920	1,3420	0,6213	0,7412	0,7939	1,3445
	0,17	0,6149	0,7422	0,7855	1,3404	0,6172	0,7433	0,7891	1,3462
	0,28	0,6258	0,7401	0,7985	1,3436	0,6346	0,7485	0,8106	1,3641
50	**0,12**	0,6130	0,7425	0,7832	1,3397	0,6139	0,7423	0,7850	1,3422
	0,17	0,6074	0,7433	0,7783	1,3378	0,6097	0,7443	0,7822	1,3436
	0,28	0,6189	0,7415	0,7902	1,3416	0,6275	0,7497	0,8020	1,3621

Table 22. Continues

L_t/h	V_{tcnt}	FGX				FGO			
		C-C	**S-S**	**C-S**	**C-F**	**C-C**	**S-S**	**C-S**	**C-F**
10	**0,12**	0,5026	0,6347	0,6246	1,1421	0,7075	0,8446	0,8883	1,5687
	0,17	0,4994	0,6242	0,6235	1,1328	0,7586	0,8893	0,9497	1,6503
	0,28	0,4593	0,5925	0,5664	1,0635	0,8530	1,0192	1,0710	1,8930
15	**0,12**	0,5357	0,6516	0,6816	1,2083	0,7504	0,8574	0,9476	1,5888
	0,17	0,5268	0,6397	0,6725	1,1877	0,7893	0,9015	0,9988	1,6709
	0,28	0,4990	0,6103	0,6313	1,1271	0,9055	1,0347	1,1430	1,9173
20	**0,12**	0,5647	0,6603	0,7101	1,2250	0,7505	0,8641	0,9528	1,5890
	0,17	0,5588	0,6477	0,7039	1,2003	0,7818	0,9079	0,9940	1,6564
	0,28	0,5196	0,6194	0,6547	1,1504	0,9060	1,0429	1,1499	1,9182
25	**0,12**	0,5813	0,6656	0,7348	1,2311	0,7384	0,8682	0,9403	1,5785
	0,17	0,5712	0,6526	0,7230	1,2095	0,7659	0,9119	0,9764	1,6525
	0,28	0,5414	0,6249	0,6827	1,1572	0,8916	1,0479	1,1352	1,9052
30	**0,12**	0,5857	0,6692	0,7428	1,2399	0,7244	0,8710	0,9243	1,5746
	0,17	0,5728	0,6559	0,7272	1,2126	0,7503	0,9145	0,9581	1,6476
	0,28	0,5503	0,6287	0,6966	1,1652	0,8747	1,0512	1,1159	1,9006
35	**0,12**	0,5840	0,6719	0,7423	1,2364	0,7116	0,8730	0,9128	1,5702
	0,17	0,5693	0,6584	0,7242	1,2055	0,7370	0,9163	0,9551	1,6426
	0,28	0,5521	0,6315	0,7006	1,1687	0,8593	1,0536	1,1017	1,8954
40	**0,12**	0,5793	0,6739	0,7375	1,2288	0,7008	0,8744	0,9107	1,5660
	0,17	0,5635	0,6602	0,7180	1,2015	0,7267	0,9176	0,9528	1,6379
	0,28	0,5499	0,6336	0,6992	1,1645	0,8462	1,0553	1,0992	1,8903
45	**0,12**	0,5734	0,6755	0,7309	1,2274	0,6930	0,8755	0,9087	1,5621
	0,17	0,5571	0,6617	0,7106	1,1998	0,7246	0,9186	0,9506	1,6339
	0,28	0,5459	0,6353	0,6950	1,1582	0,8365	1,0566	1,0968	1,8855
50	**0,12**	0,5672	0,6768	0,7237	1,2257	0,6912	0,8763	0,9068	1,5586
	0,17	0,5507	0,6628	0,7031	1,1979	0,7229	0,9193	0,9487	1,6304
	0,28	0,5409	0,6366	0,6895	1,1571	0,8344	1,0577	1,0945	1,8814

Table 23 to Table 24 investigate the effects of different angles and boundary variations on the $\bar{w}, \bar{\sigma}_{xx}, and\ \bar{\sigma}_{xz}$ values for short beams (L_t/h =5) and long beams (L_t/h =20).

Tables 23 present the dimensionless vertical displacement ($\overline{w}$) of UD, FGA, FGX, and FGO beams with a slenderness ratio of $L_t/h = 5$, under different boundary conditions and volume fractions, and with varying CNT orientation angles (θ).

The results show that for all beam types and boundary conditions, dimensionless vertical displacement generally increases as the θ increases from 0° to 90°, with the influence of CNT distributions diminishing as the angle approaches 45° and 90°. This convergence at higher angles suggests that altering the distribution of carbon nanotubes within the beam has a diminishing effect on the overall behavior.

The FGX beam consistently exhibits the lowest displacement values, followed by the UD, FGA, and FGO beams in ascending order. This is because the FGX distribution concentrates the CNTs at the top and bottom surfaces of the beam, which increases the stiffness of the beam in the vertical direction and reduces the amount of deflection.

The C-C boundary condition demonstrates the lowest displacement values, followed by the C-S, S-S, and C-F boundary conditions. This is because the C-C boundary condition provides the most constraint, which increases the stiffness of the beam and reduces the amount of deflection.

It is important to note that the dimensionless vertical displacement in Tables 23 ($x = L/2$). The vertical displacement will vary along the length of the beam and will be highest at the mid-span and lowest at the boundaries.

Tables 24 present the dimensionless vertical displacement ($\overline{w}$) of UD, FGA, FGX, and FGO beams with a slenderness ratio of $L_t/h = 20$, under different boundary conditions and volume fractions, and with varying CNT orientation angles (θ).

The FGX beam consistently exhibits the lowest displacement values, followed by the UD, FGA, and FGO beams in ascending order. This is because the FGX beam concentrates the CNTs at the top and bottom surfaces of the beam, which increases the stiffness of the beam in the vertical direction and reduces the amount of deflection.

The C-C boundary condition demonstrates the lowest displacement values, followed by the C-S, S-S, and C-F boundary conditions. This is because the C-C boundary condition provides the most constraint, which increases the stiffness of the beam and reduces the amount of deflection.

The vertical displacement will vary along the length of the beam and will be highest at the mid-span and lowest at the boundaries.

Table 23. The maximum vertical displacements ($\overline{w}$) of UD and FGA beam for various θ, boundary conditions and volume fractions (L_t/h=5)

Boundary Condition	V_{tcnt}	UD			FGA		
		0°	45°	90°	0°	45°	90°
C-C	0,12	1,0438	3,4660	3,5953	1,0787	3,4667	3,5843
	0,17	0,6326	2,0361	2,1157	0,6559	2,0288	2,1006
	0,28	0,5051	1,7752	1,8553	0,5151	1,7310	1,8067
S-S	0,12	1,6455	13,0239	13,7191	1,6803	12,9921	13,6392
	0,17	1,0031	7,6634	8,0896	1,0262	7,5849	7,9819
	0,28	0,7955	6,7052	7,1297	0,8020	6,3719	6,7887
C-S	0,12	1,3357	6,2129	6,4931	1,4201	6,2167	6,4732
	0,17	0,8110	3,6526	3,8247	0,8676	3,6411	3,7973
	0,28	0,6464	3,1901	3,3623	0,6772	3,1108	3,2737
C-F	0,12	8,1089	114,7161	121,2491	9,7454	114,8539	120,8762
	0,17	5,1156	67,5245	71,5279	6,2584	67,3522	71,0110
	0,28	3,7850	59,1277	63,1087	4,4810	57,6542	61,4253
		FGX			**FGO**		
		0°	45°	90°	0°	45°	90°
C-C	0,12	0,9673	3,3623	3,4938	1,3555	3,5674	3,6800
	0,17	0,5955	1,9412	2,0222	0,8023	2,1179	2,1863
	0,28	0,4889	1,6025	1,6830	0,6038	1,8809	1,9547
S-S	0,12	1,4969	12,3649	13,0689	2,1689	13,6978	14,3166
	0,17	0,9182	7,0729	7,5041	1,3248	8,2276	8,6026
	0,28	0,7669	5,6826	6,1055	0,9586	7,5232	7,9191
C-S	0,12	1,2276	2,3352	2,3228	1,7379	2,0109	2,1147
	0,17	0,7545	2,4153	2,3927	1,0400	1,9511	2,0765
	0,28	0,6243	2,6744	2,6298	0,7718	1,8616	1,9966
C-F	0,12	6,8403	13,4440	13,4078	12,1922	11,5402	12,0415
	0,17	4,3085	13,8842	13,8185	7,7862	11,1469	11,7670
	0,28	3,3632	15,3115	15,1361	5,3443	10,4967	11,1606

Table 24. The maximum vertical displacements ($\overline{w}$) of UD and FGA beam for various θ, boundary conditions and volume fractions(L_t/h=20)

Boundary Condition	V_{tcnt}	**UD**			**FGA**		
		0°	**45°**	**90°**	**0°**	**45°**	**90°**
C-C	**0,12**	0,1524	2,4458	2,5869	0,1876	2,4488	2,4513
	0,17	0,0968	7,0369	7,4712	0,1215	6,9621	6,8545
	0,28	0,0706	2,5900	2,7691	0,0858	2,5254	2,3271
S-S	**0,12**	0,4617	1,4397	1,5262	0,4983	1,4361	1,4045
	0,17	0,3075	6,1650	6,5965	0,3335	5,8448	5,5287
	0,28	0,2031	110,5322	117,1164	0,2194	110,6792	110,7213
C-S	**0,12**	0,2478	1,2609	1,3469	0,3211	1,2295	1,1355
	0,17	0,1606	5,0223	5,3166	0,212	5,0288	5,0323
	0,28	0,1124	65,0791	69,1125	0,1444	64,9215	63,3782
C-F	**0,12**	3,8421	11,9519	12,6609	5,4839	11,9225	11,9732
	0,17	2,5954	2,9568	3,1370	3,7473	2,9495	2,8820
	0,28	1,6614	57,0189	61,0257	2,3901	55,5971	51,1014
		FGX			**FGO**		
		0°	**45°**	**90°**	**0°**	**45°**	**90°**
C-C	**0,12**	0,1262	2,3085	2,5789	0,2345	2,5870	2,7131
	0,17	0,0799	6,4155	7,3676	0,1514	7,6414	8,0254
	0,28	0,0617	2,1489	2,6952	0,1025	2,9577	3,1251
S-S	**0,12**	0,3374	1,3171	1,5152	0,8311	1,5586	1,6349
	0,17	0,2233	5,0995	6,2685	0,5618	7,0576	7,4608
	0,28	0,1527	104,0580	116,7559	0,36	117,2070	123,0962
C-S	**0,12**	0,1949	1,0500	1,3109	0,4086	1,4356	1,5159
	0,17	0,1256	4,7345	5,3002	0,2696	5,3187	5,5817
	0,28	0,0924	59,3016	68,6120	0,1779	70,7041	74,2701
C-F	**0,12**	2,6926	11,2557	12,5842	7,2273	12,6695	13,3035
	0,17	1,8118	2,6998	3,1143	4,9372	3,2063	3,3656
	0,28	1,1814	47,1157	59,3934	3,1231	65,3291	69,0731

Tables 25 present the dimensionless normal stresses ($\bar{\sigma}_{xx}$) for UD, FGA, FGX, and FGO beams with a slenderness ratio of L_t/h = 5, under different boundary conditions and volume fractions, and with varying θ.

$\bar{\sigma}_{xx}$ decreases as the θ increases from 0° to 90°, with the influence of CNT distributions diminishing as the angle approaches 45° and 90°. This convergence at higher angles suggests that altering the distribution within the beam has a diminishing effect on the overall behavior. The FGX beam consistently exhibits the highest stress values, followed by the UD, FGA, and FGO beams in descending order. This is because the FGX distribution concentrates the CNTs at the top and bottom surfaces of the beam, which are the regions that experience the most stress during bending. This increases the stiffness of the beam in the axial direction, which in turn increases the $\bar{\sigma}_{xx}$. The C-C boundary condition demonstrates the highest stress values, followed by the C-S, S-S, and C-F boundary conditions.

Tables 26 illustrate the dimensionless normal stresses ($\bar{\sigma}_{xx}$) of UD, FGA, FGX, and FGO beams with a slenderness ratio of L_t/h = 20, under different boundary conditions and volume fractions, and with varying θ. For UD and FGX beams, the normal stresses generally decrease as the CNT orientation angle increases from 0° to 90°. Conversely, the opposite trend is observed for FGA and FGO beams, where normal stresses increase with increasing CNT orientation angle.

Examining the effect of CNT distribution under different boundary conditions reveals distinct patterns. For C-C and S-S boundary conditions, normal stresses decrease with increasing CNT distribution for UD and FGX beams. In the case of C-S and C-F boundary conditions, normal stresses initially decrease and then increase with increasing CNT distribution for UD and FGX beams, reaching their highest values at a volume fraction of 0,28. For FGA and FGO beams, normal stresses consistently decrease with increasing CNT distribution across all boundary conditions.

The observed differences in normal stresses based on CNT distribution type can be attributed to the varying stiffness profiles across the beam's thickness. FGX beams, with CNTs concentrated at the top and bottom surfaces, exhibit higher stiffness in the axial direction compared to UD beams, where CNTs are uniformly distributed. This increased stiffness results in lower normal stresses for FGX beams under most loading conditions. Conversely, FGA and FGO beams, with CNTs concentrated at the bottom and top surfaces, respectively, exhibit lower axial stiffness compared to UD beams, leading to higher normal stresses.

Table 25. The maximum normal stresses ($\bar{\sigma}_{xx}$) of UD, FGA, FGX and FGO beam for various θ, boundary conditions and volume fractions (L_t/h=5)

Boundary condition	V_{tcnt}	**UD**			**FGA**		
		0°	**45°**	**90°**	**0°**	**45°**	**90°**
C-C	**0,12**	13,9377	3,8165	3,7453	0,3948	3,3622	3,4437
	0,17	13,1346	3,8088	3,7358	0,2407	3,1840	3,3007
	0,28	14,8405	3,7926	3,7128	0,1661	2,8345	2,9645
S-S	**0,12**	5,5448	3,8002	3,7967	0,1629	3,2982	3,4443
	0,17	5,2851	3,7998	3,7963	0,1005	3,1025	3,2832
	0,28	5,8707	3,7990	3,7952	0,0681	2,7000	2,8925
C-S	**0,12**	6,5902	2,1929	2,2125	0,2079	1,9795	2,0781
	0,17	5,9599	2,1950	2,2151	0,1246	1,9035	2,0216
	0,28	7,3352	2,1994	2,2218	0,0894	1,7658	1,8908
C-F	**0,12**	23,6699	12,6687	12,6879	0,8802	11,3504	11,8389
	0,17	22,2141	12,6706	12,6908	0,5438	10,8633	11,4649
	0,28	25,3833	12,6749	12,6977	0,369	9,9480	10,5903
		FGX			**FGO**		
		0°	**45°**	**90°**	**0°**	**45°**	**90°**
C-C	**0,12**	20,1079	4,1265	4,0297	0,7813	3,4102	3,4871
	0,17	19,1201	4,2904	4,1772	0,4666	3,2537	3,3645
	0,28	21,8556	4,8173	4,6438	0,3248	2,9611	3,0807
S-S	**0,12**	7,9562	4,0395	4,0192	0,2424	3,4557	3,5958
	0,17	7,5776	4,1736	4,1441	0,1489	3,3333	3,5084
	0,28	8,7107	4,6070	4,5433	0,0986	3,1255	3,3124
C-S	**0,12**	9,9227	5,7047	5,5901	0,2379	4,7495	4,8712
	0,17	9,0815	5,9225	5,7873	0,1277	4,5414	4,7103
	0,28	11,4843	6,6219	6,4113	0,0981	4,1568	4,3384
C-F	**0,12**	34,5262	18,9296	18,6891	0,9501	15,9648	16,4943
	0,17	32,5992	19,6095	19,3124	0,5564	15,3311	16,0210
	0,28	38,0805	21,8004	21,2949	0,3881	14,2029	14,9418

Table 26. The maximum normal stresses ($\bar{\sigma}_{xx}$) of UD, FGA, FGX and FGO beam for various θ, boundary conditions and volume fractions (L_t/h=20)

Boundary condition	V_{tcnt}	**UD**			**FGA**		
		0°	**45°**	**90°**	**0°**	**45°**	**90°**
C-C	**0,12**	19,5243	10,4438	10,4142	0,6995	9,3145	9,6784
	0,17	18,5330	10,4406	10,4103	0,4346	8,8898	9,3476
	0,28	20,6819	10,4338	10,4010	0,2914	8,0790	8,5712
S-S	**0,12**	15,4491	15,0125	15,0117	0,4889	13,0315	13,6200
	0,17	15,3840	15,0125	15,0116	0,3133	12,2604	12,9851
	0,28	15,5311	15,0123	15,0113	0,1970	10,6726	11,4440
C-S	**0,12**	26,0032	11,0587	11,0806	0,9637	9,8915	10,3221
	0,17	24,8951	11,0611	11,0834	0,6037	9,4581	9,9872
	0,28	27,2862	11,0661	11,0904	0,3987	8,6348	9,2002
C-F	**0,12**	79,4977	53,6527	53,6844	3,2868	47,9559	49,9810
	0,17	77,4499	53,6561	53,6885	2,0870	45,8327	48,3372
	0,28	81,8949	53,6634	53,6986	1,3457	41,7957	44,4762
		FGX			**FGO**		
		0°	**45°**	**90°**	**0°**	**45°**	**90°**
C-C	**0,12**	27,9957	11,1235	11,0446	0,9115	9,4780	9,8450
	0,17	26,7015	11,5019	11,3951	0,5486	9,1317	9,5948
	0,28	30,3731	12,7242	12,5143	0,3739	8,5365	9,0317
S-S	**0,12**	20,6054	15,9435	15,8783	0,7236	13,6636	14,2286
	0,17	20,5159	16,4674	16,3671	0,4643	13,1867	13,8899
	0,28	20,7796	18,1590	17,9296	0,2912	12,3807	13,1309
C-S	**0,12**	36,5508	11,7192	11,6971	1,2328	10,086	10,5232
	0,17	35,1533	12,0940	12,0488	0,7488	9,7468	10,2852
	0,28	39,0850	13,3041	13,1739	0,5046	9,1804	9,7540
C-F	**0,12**	109,6898	56,9420	56,7488	3,7251	48,864	50,9150
	0,17	107,0223	58,7977	58,4835	2,3207	47,1775	49,7221
	0,28	114,5885	64,7908	64,0229	1,5130	44,3385	47,0522

Table 27 presents the maximum shear stresses ($\bar{\sigma}_{xz}$) of UD, FGA, FGX, and FGO beams with a slenderness ratio of L_t/h = 5 for various θ and V_{tcnt}, boundary conditions. The data reveals a consistent trend across all beam types and support conditions: maximum shear stresses generally increase as the CNT orientation angle decreases from 0° to 90°. This convergence at higher angles suggests that altering the distribution within the beam has a diminishing effect on the overall behavior.

UD beams consistently exhibit higher maximum shear stress ($\bar{\sigma}_{xz}$) values compared to FGA beams across all configurations. This suggests that a UD might lead to higher shear stresses compared to an FGA in short beams. FGX configuration consistently displays the lowest maximum shear stress values, indicating its superior shear resistance due to the strategic placement of CNTs at both the top and bottom surfaces.

The influence of boundary conditions is also evident, with C-C support consistently yielding the highest shear stresses, followed by C-S, S-S, and C-F, respectively. This trend reflects the decreasing level of constraint and stiffness offered by each support type.

Table 28 presents the maximum shear stresses ($\bar{\sigma}_{xz}$) of UD, FGA, FGX, and FGO beams with a slenderness ratio of L_t/h = 20 for various θ and V_{tcnt}, boundary conditions.

$\bar{\sigma}_{xz}$ increases as the θ increases from 0° to 90°, with the influence of CNT distributions diminishing as the angle approaches 45° and 90°.The influence of the angle on shear stress becomes nearly negligible between 45 and 90 degrees. Higher angles indicate a diminishing influence of CNT distribution on overall beam behavior. As observed in short beams, the data reveals that for both UD and FGA beams, maximum shear stresses generally increase as the CNT orientation angle increases from 0° to 90°. This reinforces the understanding that CNTs aligned closer to the beam axis are less effective in resisting shear deformation, regardless of beam length.

Contrary to the observations in short beams (Table 27), the difference in maximum shear stresses between UD and FGA beams is less noticeable in these longer beams. This suggests that the effect of concentrating CNTs at the bottom surface (FGA) on shear stress might be less significant as the beam length increases.

The influence of boundary conditions on maximum shear stress remains consistent with previous observations. The C-C support type consistently exhibits the highest values, followed by C-S, S-S, and C-F, respectively. This reaffirms the relationship between constraint level and shear stress, where higher constraint leads to higher shear stresses.

Table 27. The maximum shear stresses ($\bar{\sigma}_{xz}$) of UD, FGA, FGX, and FGO beam for various θ, boundary conditions and volume fractions (L_t/h=5)

Boundary Condition	V_{tcnt}	**UD**			**FGA**		
		0°	**45°**	**90°**	**0°**	**45°**	**90°**
C-C	**0,12**	0,4493	0,6404	0,6396	0,4489	0,6390	0,6380
	0,17	0,6519	0,6404	0,6395	0,6507	0,6368	0,6358
	0,28	0,5538	0,6402	0,6391	0,5654	0,6267	0,6257
S-S	**0,12**	1,1295	0,7350	0,7357	1,1279	0,7332	0,7337
	0,17	0,4622	0,7351	0,7357	0,4608	0,7306	0,7312
	0,28	0,6593	0,7352	0,7359	0,6563	0,7185	0,7197
C-S	**0,12**	0,5723	0,8144	0,8137	0,5831	0,8125	0,8116
	0,17	1,1493	0,8143	0,8135	1,1455	0,8098	0,8088
	0,28	0,4340	0,8142	0,8132	0,4286	0,7970	0,7961
C-F	**0,12**	0,6433	1,3559	1,3542	0,6326	1,3528	1,3507
	0,17	0,5329	1,3557	1,3539	0,5382	1,3482	1,3461
	0,28	1,1098	1,3554	1,3533	1,0930	1,3268	1,3248
		FGX			**FGO**		
		0°	**45°**	**90°**	**0°**	**45°**	**90°**
C-C	**0,12**	0,3855	0,5911	0,5908	0,6250	0,6993	0,6976
	0,17	0,5768	0,5692	0,5691	0,8076	0,7329	0,7308
	0,28	0,4688	0,5170	0,5174	0,7631	0,8443	0,8410
S-S	**0,12**	0,9929	0,6770	0,6779	1,4493	0,8049	0,8047
	0,17	0,3834	0,6514	0,6524	0,6744	0,8452	0,8448
	0,28	0,5630	0,5909	0,5921	0,8542	0,9792	0,9786
C-S	**0,12**	0,4676	0,7512	0,7512	0,8291	0,8897	0,8879
	0,17	0,9732	0,7232	0,7234	1,5355	0,9328	0,9304
	0,28	0,3212	0,6564	0,6573	0,7534	1,0754	1,0716
C-F	**0,12**	0,4986	1,2514	1,2508	0,9744	1,4806	1,4771
	0,17	0,4019	1,2050	1,2047	0,9182	1,5519	1,5476
	0,28	0,8497	1,0945	1,0953	1,7484	1,7882	1,7842

Table 28. The maximum shear stresses ($\bar{\sigma}_{xz}$) of UD, FGA, FGX, and FGO beam for various θ, boundary conditions and volume fractions (L_t/h=20)

Boundary Condition	V_{tcnt}	**UD**			**FGA**		
		0°	**45°**	**90°**	**0°**	**45°**	**90°**
C-C	**0,12**	0,6296	0,5838	0,5834	0,6286	0,5824	0,5819
	0,17	0,6350	0,5837	0,5834	0,6323	0,5805	0,5799
	0,28	0,6219	0,5836	0,5833	0,6120	0,5712	0,5708
S-S	**0,12**	0,7262	0,7483	0,7484	0,7240	0,7462	0,7464
	0,17	0,7282	0,7483	0,7484	0,7236	0,7435	0,7438
	0,28	0,7240	0,7483	0,7484	0,7095	0,7311	0,7320
C-S	**0,12**	0,7956	0,7669	0,7665	0,7974	0,7651	0,7645
	0,17	0,8036	0,7668	0,7664	0,8029	0,7625	0,7619
	0,28	0,7844	0,7667	0,7663	0,7756	0,7504	0,7499
C-F	**0,12**	1,3445	1,3175	1,3169	1,3419	1,3145	1,3134
	0,17	1,3457	1,3174	1,3168	1,3393	1,3101	1,3090
	0,28	1,3425	1,3173	1,3165	1,3184	1,2892	1,2884
		FGX			**FGO**		
		0°	**45°**	**90°**	**0°**	**45°**	**90°**
C-C	**0,12**	0,5575	0,5386	0,5385	0,7505	0,6381	0,6372
	0,17	0,5442	0,5187	0,5186	0,7818	0,6693	0,6682
	0,28	0,4805	0,4714	0,4715	0,9060	0,7735	0,7721
S-S	**0,12**	0,6518	0,6898	0,6902	0,8641	0,8186	0,8179
	0,17	0,6307	0,6640	0,6644	0,9079	0,8592	0,8582
	0,28	0,5727	0,6028	0,6036	1,0429	0,9941	0,9928
C-S	**0,12**	0,7010	0,7075	0,7074	0,9528	0,8383	0,8371
	0,17	0,6855	0,6813	0,6812	0,9940	0,8794	0,8780
	0,28	0,6053	0,6191	0,6193	1,1499	1,0163	1,0145
C-F	**0,12**	1,2094	1,2156	1,2153	1,5890	1,4402	1,4383
	0,17	1,1688	1,1705	1,1704	1,6564	1,5108	1,5084
	0,28	1,0636	1,0637	1,0640	1,9182	1,7462	1,7430

Figure 21 shows the change in dimensionless vertical displacement ($\overline{w}$) with various L_t/h, boundary conditions and distribution types. Notably, due to the significantly high values attained at the C-F boundary condition, separate illustration is provided on Figure 22.

The FGX beam consistently exhibits the lowest displacement values, followed by the UD, FGA, and FGO beams in ascending order. This is because the FGX distribution concentrates the CNTs at the top and bottom surfaces of the beam, which increases the stiffness of the beam in the vertical direction and reduces the amount of deflection. The C-C boundary condition demonstrates the lowest displacement values, followed by the C-S, S-S, and C-F boundary conditions. This is because the C-C boundary condition provides the most constraint, which increases the stiffness of the beam and reduces the amount of deflection. The vertical displacement will vary along the length of the beam and will be highest at the mid-span and lowest at the boundaries.

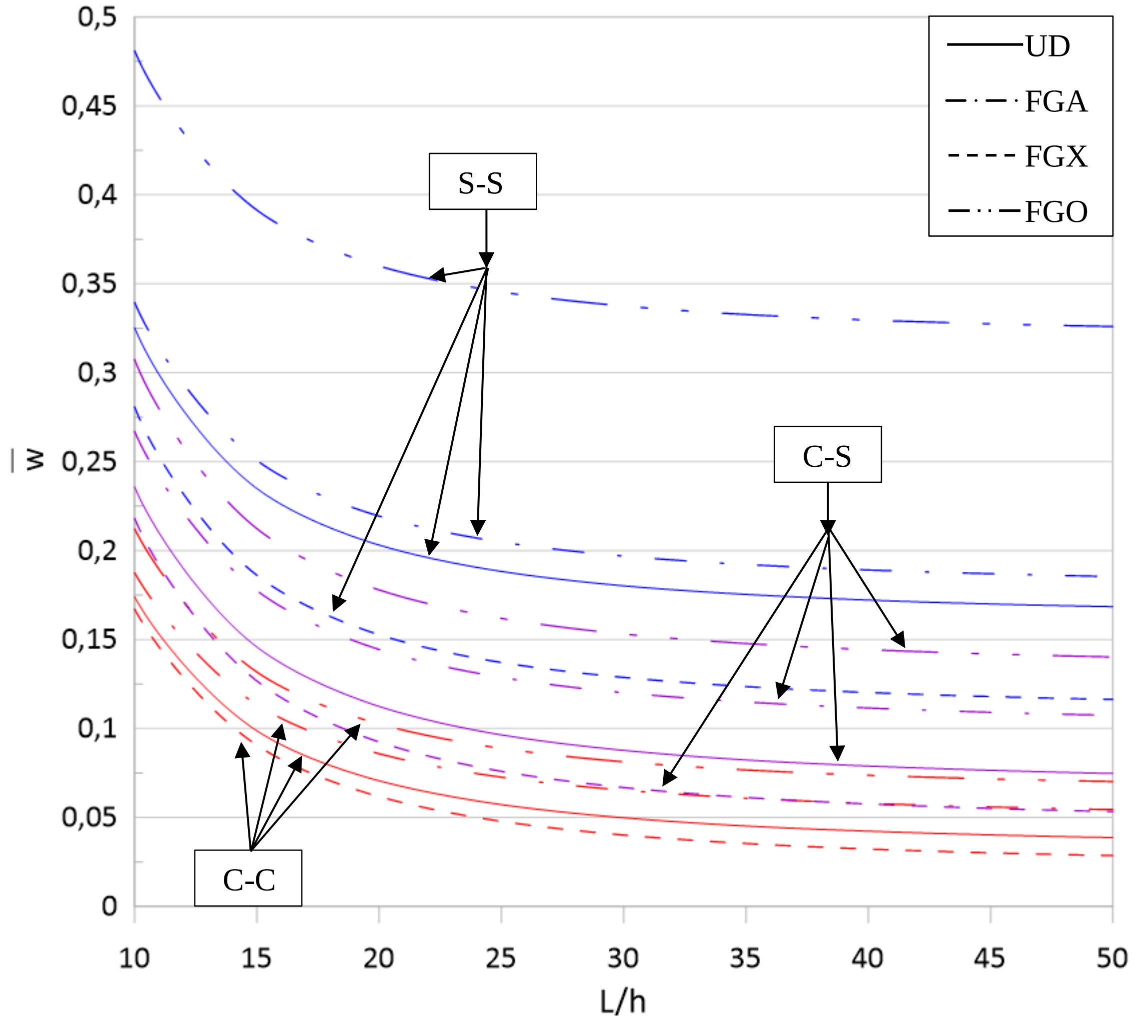

Figure 21. The change in dimensionless vertical displacement with L_t/h for various boundary conditions and CNT distribution types (V_{tcnt} = 0,28)

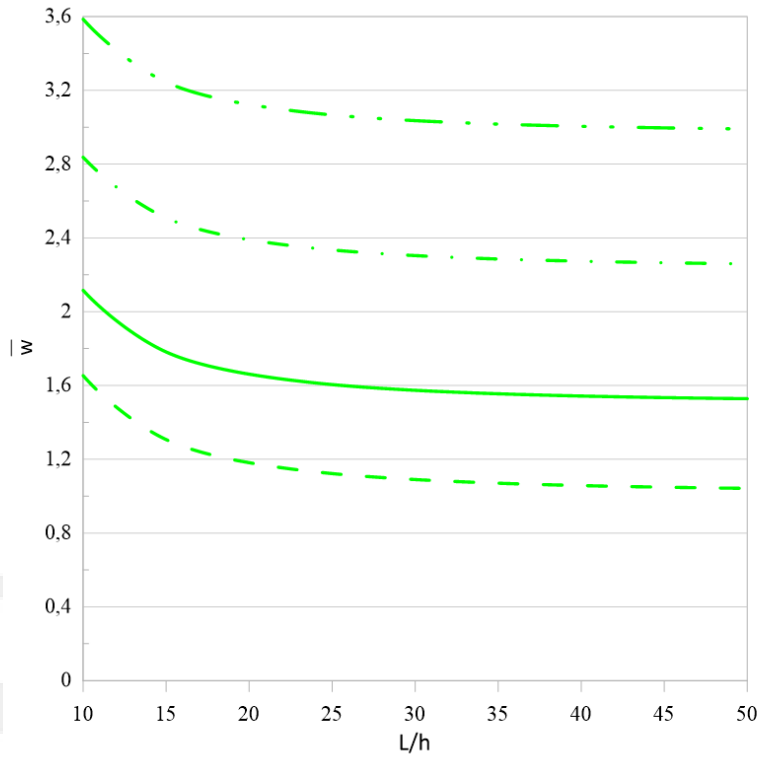

Figure 22. The dimensionless displacements under different slenderness ratios and CNT distributions (C-F) ($V_{tcnt} = 0{,}28$)

Figures 23 to 26 show the vertical displacement of the beam along the beam length for various CNT distribution types in case of C-C, S-S, C-S and C-F, respectively. Among the beam types, the FGO beam exhibited the highest displacement, signifying greater flexibility, followed by FGA, UD, and FGX. Upon examining the FGO distribution, it is noted that the CNT distribution decreases at the upper and lower regions of the beam while increasing at the mid regions. This in turn leads to a decrease in flexural rigidity, independent of the selected boundary condition. The maximum vertical displacement occurred at the center of the beam in both the C-C and S-S boundary conditions. However, in the case of the C-S boundary, the peak displacement was observed beyond the beam's center due to the absence of symmetry. Furthermore, the C-F boundary, which lacks restraint at its right end, resulted in the non-return of the beam's right end to the 0 point.

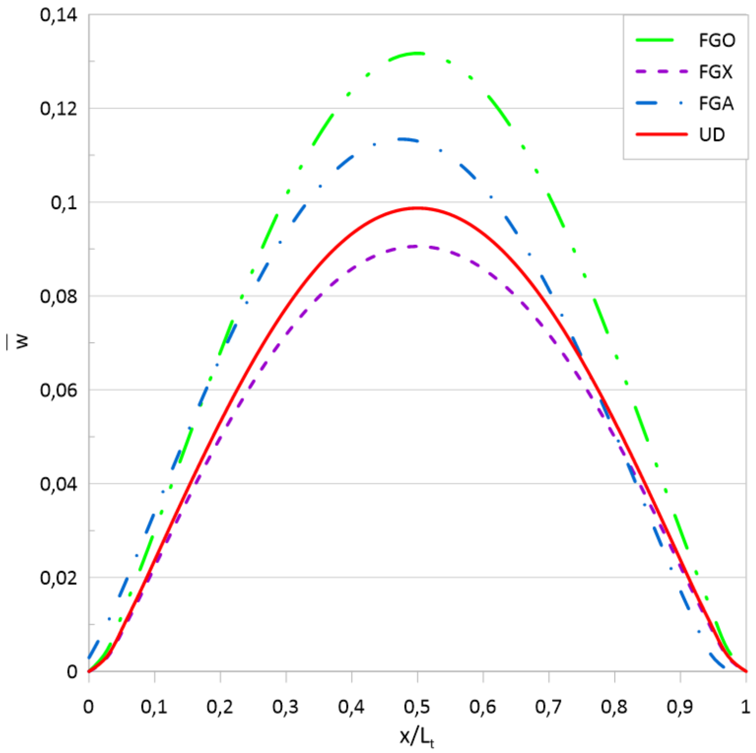

Figure 23. Dimensionless vertical displacement of beam along the beam length under different CNT distribution (C-C) ($V_{tcnt} = 0{,}28$)

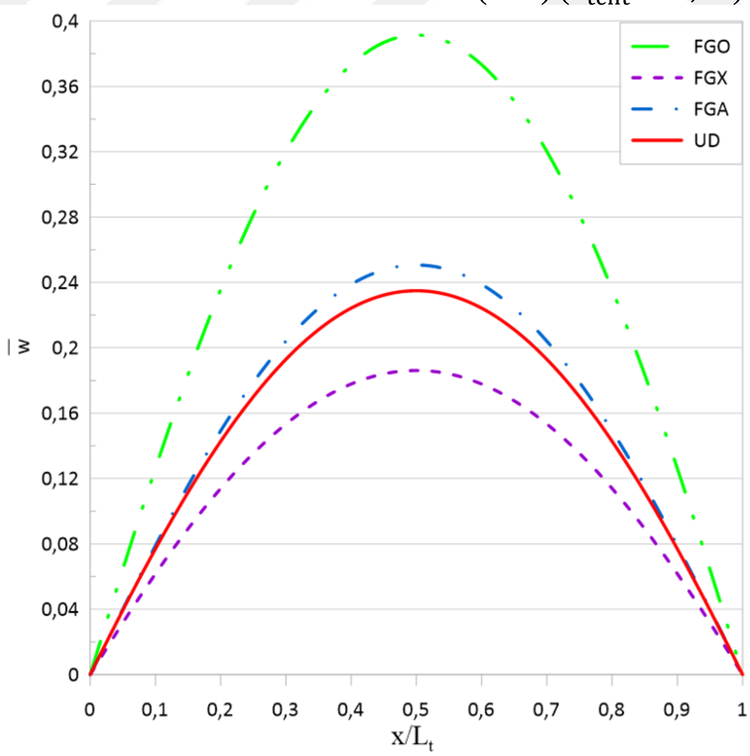

Figure 24. Dimensionless vertical displacement of beam along the beam length under different CNT distribution (S-S) ($V_{tcnt} = 0{,}28$)

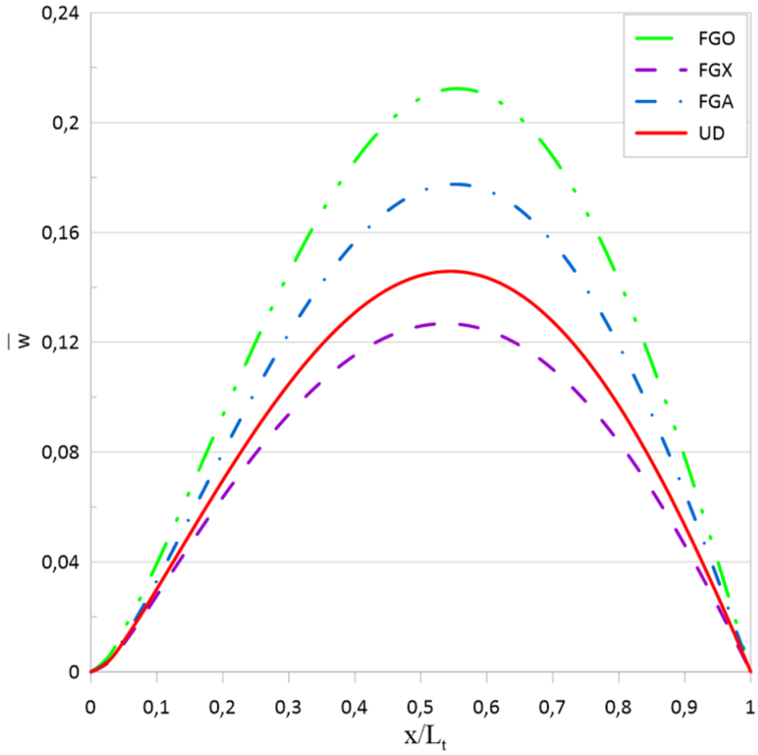

Figure 25. Dimensionless vertical displacement of beam along the beam length under different CNT distribution (C-S) ($V_{tcnt} = 0{,}28$)

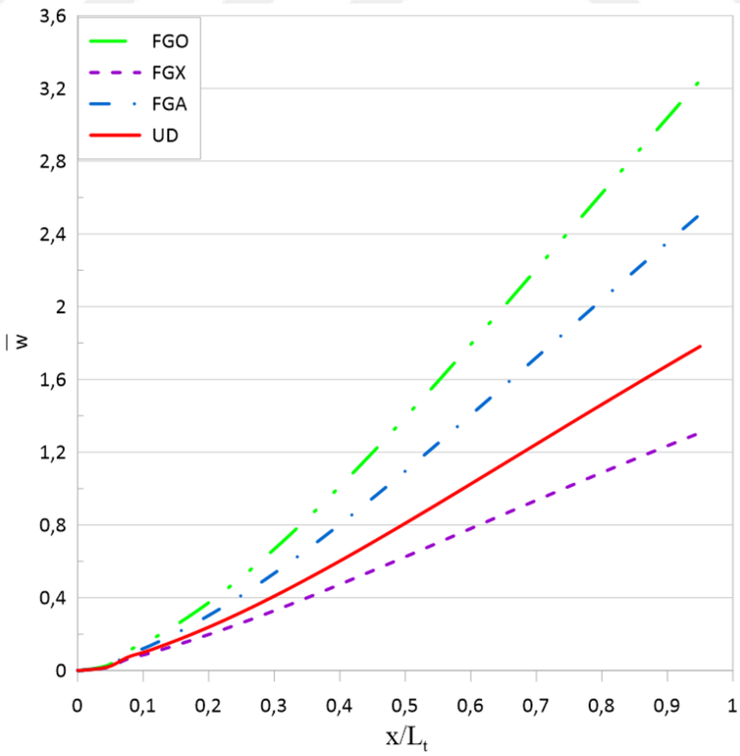

Figure 26. Dimensionless vertical displacement of beam along the beam length under different CNT distribution (C-F) ($V_{tcnt} = 0{,}28$)

Figure 27 shows the non-dimensional normal stress ($\bar{\sigma}_{xx}$) distribution through the thickness of a simply supported (S-S) UD beam with a length-to-height ratio of L_t/h = 15, for different V_{cnt}.

The results show that the normal stress is highest at the top and bottom surfaces of the beam, and lowest at the mid-plane. This is because the top and bottom surfaces experience the most stress during bending. The normal stress also increases with increasing CNT volume fraction. This is because the stiffness of the beam in the axial direction increases as the CNTs become more aligned with the beam axis. The normal stress distribution is nearly linear for all CNT volume fractions. This is because the UD beam has a uniform distribution of CNTs throughout its thickness.

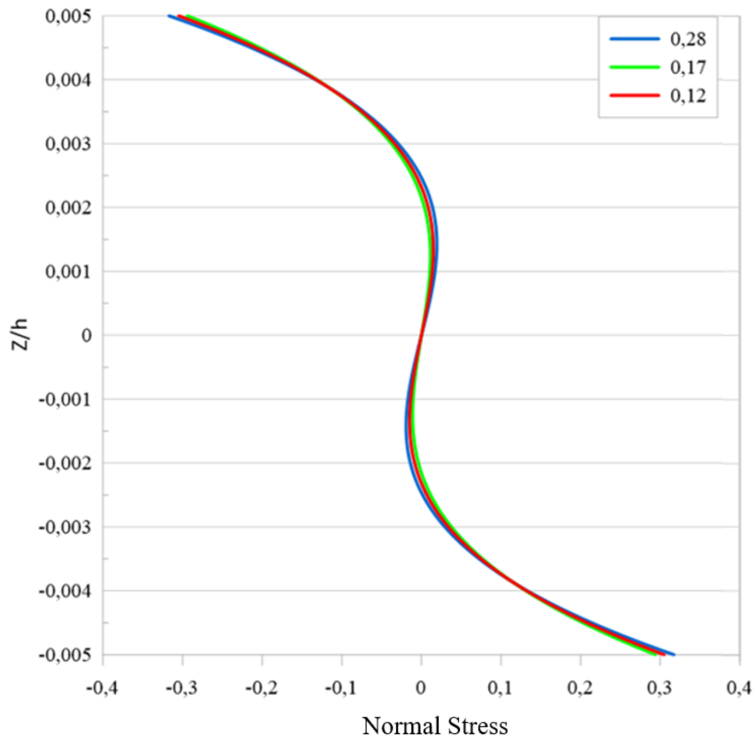

Figure 27. Non dimensional normal stress ($\bar{\sigma}_{xx}$) UD beam along the depth at x=0 with L_t/h=15 and different V_{tcnt} (S-S)

Figures 28 and 29 illustrate the variation in dimensionless normal stress along the height of the beam at the x=0 point. The V_{cnt} was kept constant at 0,12, and L_t/h =15 was used. Analysis of the results reveals that, at the midpoint (z=0) of the beam, all distributions except FGA converge towards zero. The asymmetry of the FGA distribution accounts for its failure to approach zero. Furthermore, an increase in CNT distribution at the upper and lower points of the beam leads to an increase in beam rigidity. The highest value is observed in the FGA distribution, followed by FGX, UD, and FGO distributions.

Figures 28 and 29 show the non-dimensional normal stress ($\bar{\sigma}_{xx}$) distribution through the thickness of a C-C and S-S FG-CNTRC beam, respectively, with a length-to-height ratio of L_t/h = 15 and a CNT volume fraction of V_{cnt} = 0,12, for different CNT distributions.

The results show that the normal stress is highest at the top and bottom surfaces of the beam, and lowest at the mid-plane. This is because the top and bottom surfaces experience the most stress during bending. The normal stress distribution is nearly linear for the UD beam, as expected due to the uniform distribution of CNTs throughout its thickness. However, the normal stress distribution is non-linear for the FG beams, due to the non-uniform distribution of CNTs. For the C-C, the FGX beam exhibits the highest normal stresses, followed by the UD, FGA, and FGO beams in descending order. This is because the FGX distribution concentrates the CNTs at the top and bottom surfaces of the beam, which increases the stiffness of the beam in the axial direction and therefore the normal stresses.

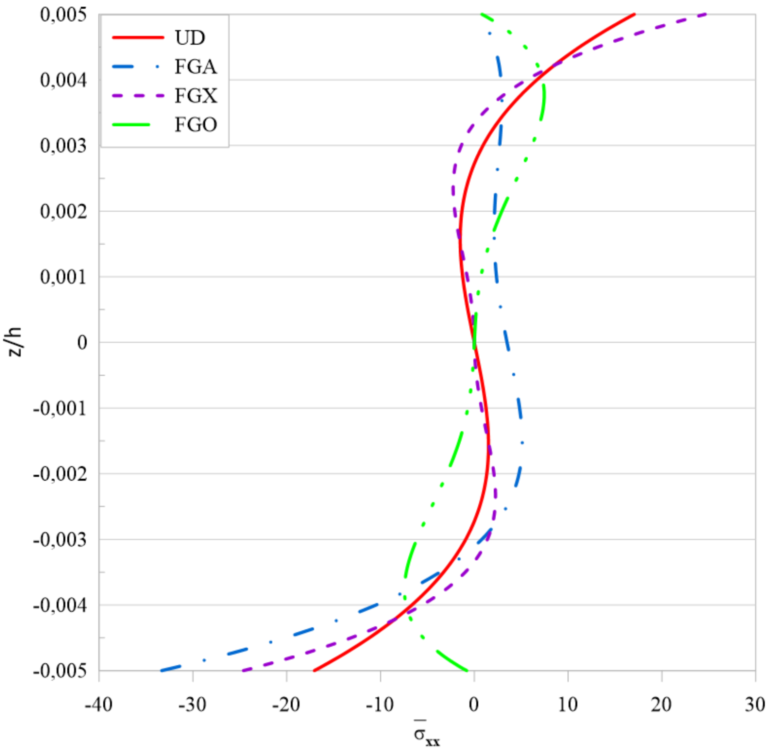

Figure 28. Non dimensional normal stress ($\bar{\sigma}_{xx}$) along the beam length at x=0 with L_t/h = 15 and V_{tcnt} = 0,12 (C-C)

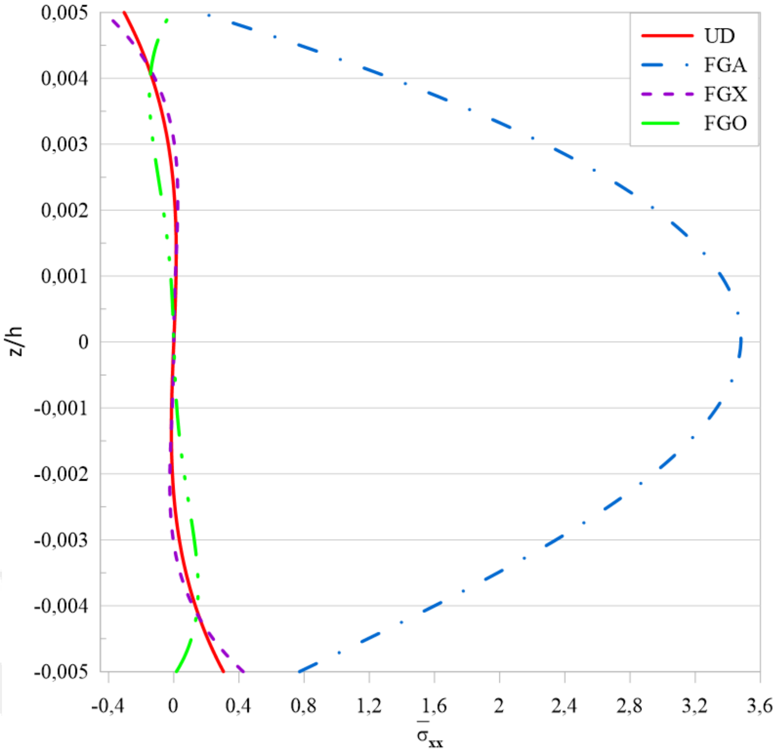

Figure 29. Non dimensional normal stress ($\bar{\sigma}_{xx}$) along the beam length at x=0 with L_t/h = 15 and V_{tcnt} = 0,12 (S-S)

Figures 30 and 31 show the non-dimensional normal stress ($\bar{\sigma}_{xx}$) distribution through the thickness of a C-S and C-F FG-CNTRC beam, respectively, with a L_t/h = 15 and a CNT volume fraction of V_{cnt} = 0,12, for different CNT distributions.The results show that the normal stress is highest at the top and bottom surfaces of the beam, and lowest at the mid-plane. This is because the top and bottom surfaces experience the most stress during bending. The normal stress distribution is nearly linear for the UD beam, as expected due to the uniform distribution of CNTs throughout its thickness. However, the normal stress distribution is non-linear for the FG beams, due to the non-uniform distribution of CNTs.

For the C-S, the FGX and FGA beams exhibit the highest normal stresses, followed by the UD and FGO beams in descending order. This is because the FGX and FGA beams concentrate the CNTs at the top and bottom surfaces of the beam, respectively, which increases the stiffness of the beam in the axial direction and therefore the normal stresses.

For the C-F, the FGX beam exhibits the highest normal stresses, followed by the UD, FGA, and FGO beams in descending order. This is because the FGX distribution concentrates the CNTs at the top and bottom surfaces of the beam, which increases the stiffness of the beam in the axial direction and therefore the normal stresses.

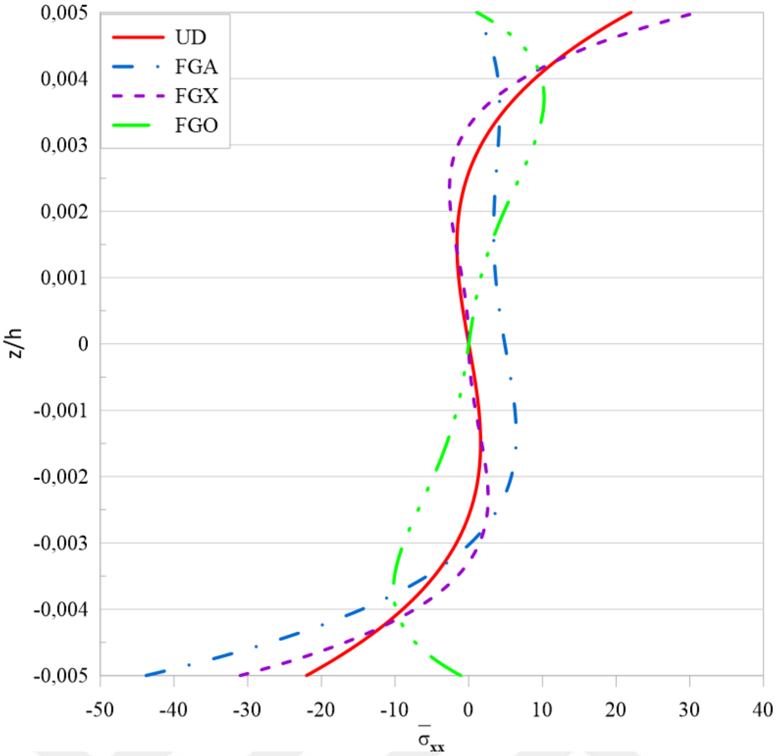

Figure 30. Non dimensional normal stress ($\bar{\sigma}_{xx}$) along the beam length at x=0 with $L_t/h = 15$ and $V_{tcnt} = 0{,}12$ (C-S)

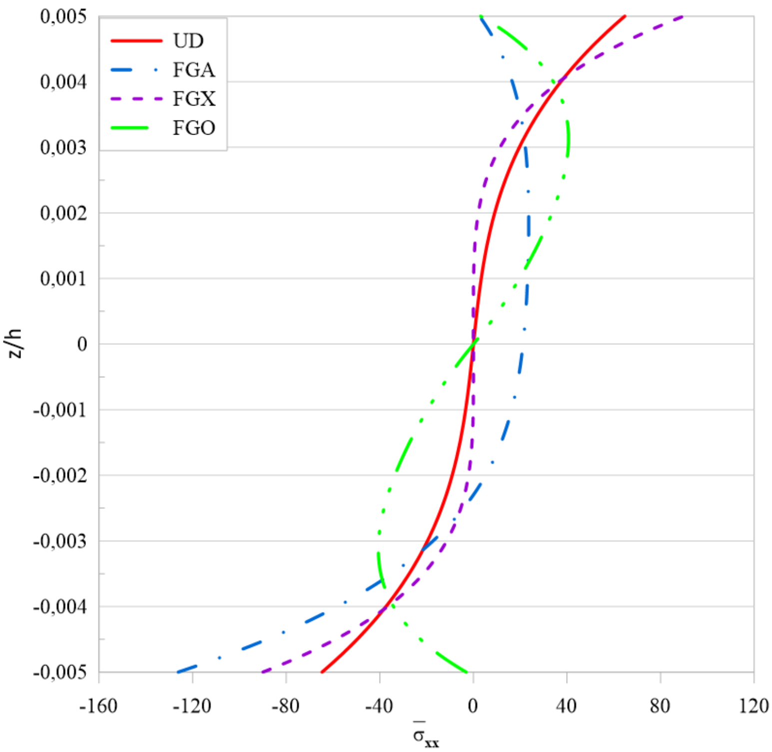

Figure 31. Non dimensional normal stress ($\bar{\sigma}_{xx}$) along the beam length at x=0 with $L_t/h = 15$ and $V_{tcnt} = 0{,}12$ (C-F)

Figures 32 and 33 show the non-dimensional normal stress ($\bar{\sigma}_{xx}$) distribution along the length of a beam with a length-to-height ratio of L_t/h = 15 and a CNT volume fraction of V_{cnt}= 0,12, for different CNT distributions and boundary conditions.

The results show that the normal stress is highest at the boundaries and lowest at the mid-span of the beam. This is because the boundaries provide the most constraint, and therefore the beam experiences the most stress at these points.

The normal stress distribution is also affected by the CNT distribution and boundary conditions. For example, the FGX beam with C-C boundary exhibits the highest normal stresses, followed by the UD beam with C-C boundary. This is because the FGX distribution concentrates the CNTs at the top and bottom surfaces of the beam, which increases the stiffness of the beam in the axial direction and therefore the normal stresses. Additionally, the C-C boundary condition provides the most constraint, which further increases the normal stresses.

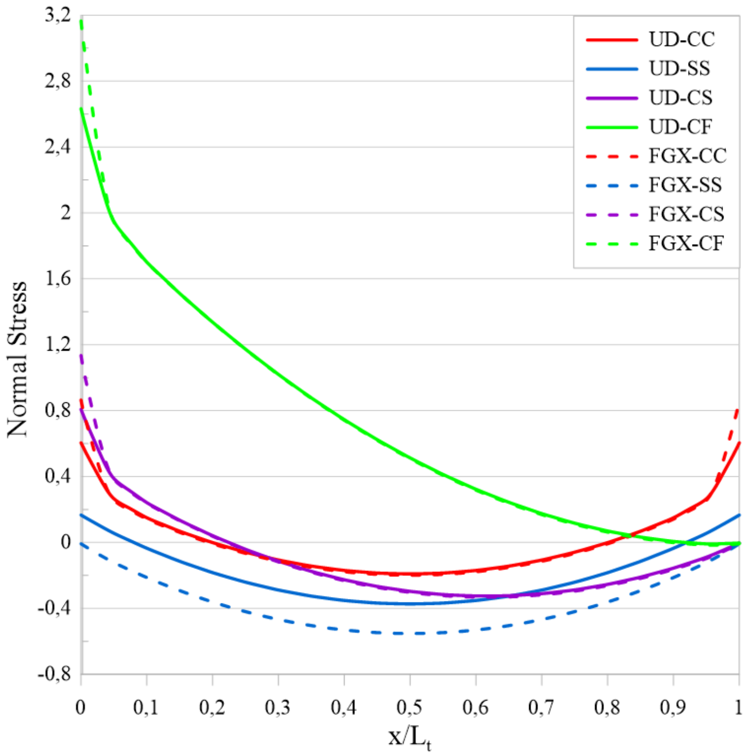

Figure 32. Non dimensional normal stress ($\bar{\sigma}_{xx}$) of UD and FGX beam along the beam length at x=0 with L_t/h = 15 and V_{tcnt} = 0,12

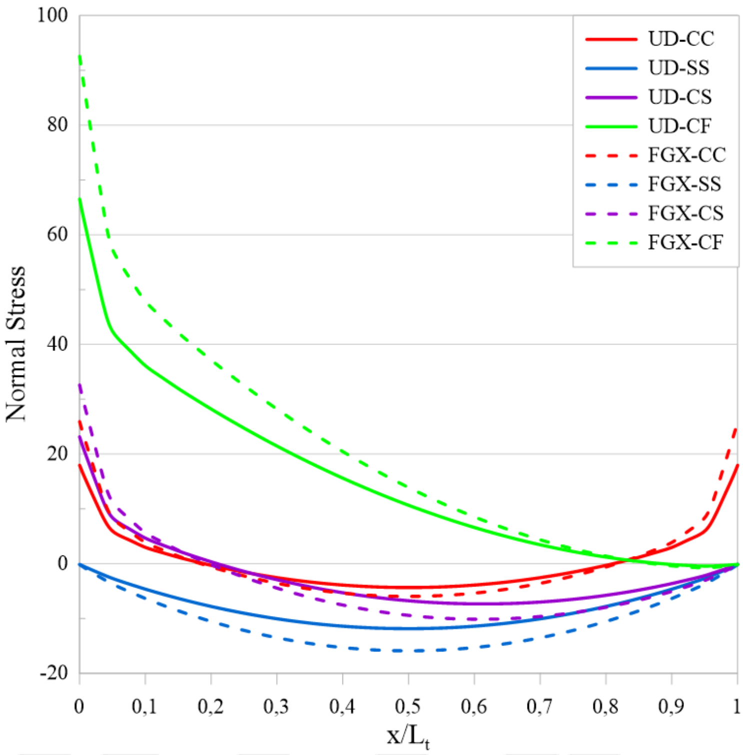

Figure 33. Non dimensional normal stress ($\bar{\sigma}_{xx}$) of FGA and FGO beam along the beam length at x=0 with L_t/h = 15 and $V_{tcnt} = 0{,}12$

Figures 34 and 35 show the dimensionless shear stress ($\bar{\sigma}_{xz}$) distribution through the thickness of a C-C and S-S FG-CNTRC beam, respectively, with a length-to-height ratio of L_t/h = 15 and a CNT volume fraction of V_{tcnt}= 0,28, for different CNT distributions.

The results show that the shear stress is highest at the mid-plane of the beam and lowest at the top and bottom surfaces. This is because the shear stress is zero at the top and bottom surfaces of the beam, and the shear stress distribution is parabolic through the thickness of the beam. The shear stress distribution is also affected by the CNT distribution. For example, the FGO beam exhibits the highest shear stresses, followed by the UD, FGA, and FGX beams in descending order. This is because the FGO distribution concentrates the CNTs at the mid-plane of the beam, which increases the shear stiffness of the beam and therefore the shear stresses.

Overall, the results in Figures 36 and 37 show that the CNT distribution and boundary condition have a significant effect on the shear stress distribution in FG-CNTRC beams.

It is important to note that the dimensionless shear stresses in Figures 36 and 37 are calculated at the mid-span of the beam (x = L/2). The shear stresses will vary along the length of the beam and will be highest at the boundaries and lowest at the mid-span.

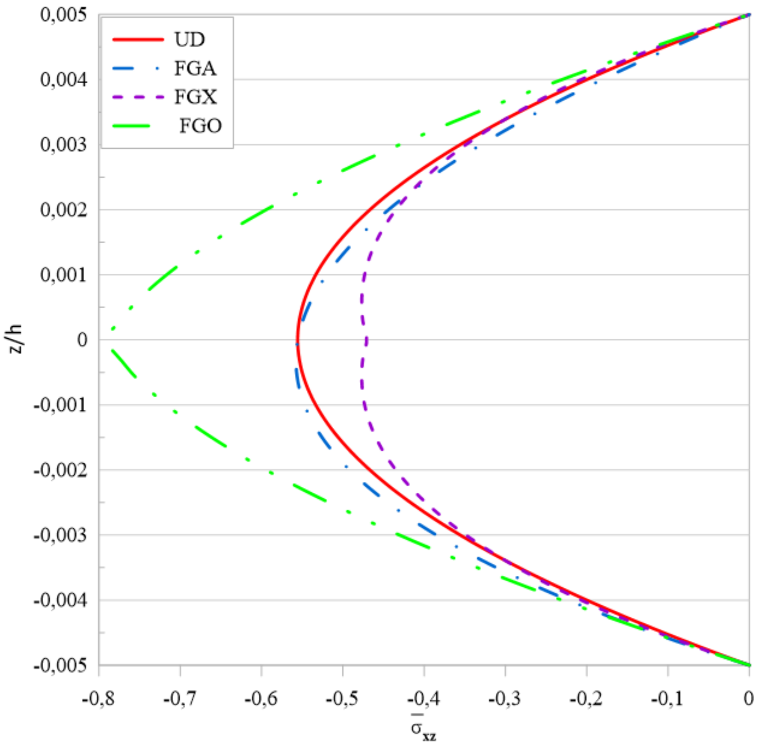

Figure 34. Dimensionless shear stresses under uniform load through beam height (C-C) (L_t/h =15) ($V_{tcnt} = 0{,}28$)

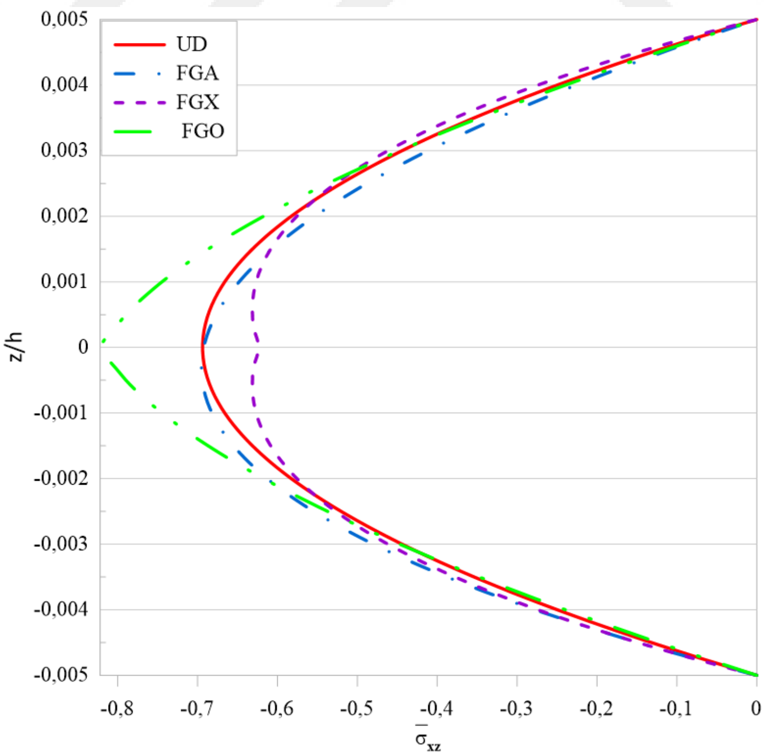

Figure 35. Dimensionless shear stresses under uniform load through beam height (S-S) (L_t/h =15) ($V_{tcnt} = 0{,}28$)

Figures 36 and 37 show the dimensionless shear stress ($\bar{\sigma}_{xz}$) distribution through the thickness of a C-S and C-F FG-CNTRC beam, respectively, with a L_t/h = 15 and a CNT volume fraction of V_{cnt} = 0,12, for different CNT distributions.

The results show that the shear stress is highest at the mid-plane of the beam and lowest at the top and bottom surfaces. This is because the shear stress is zero at the top and bottom surfaces of the beam, and the shear stress distribution is parabolic through the thickness of the beam.

The shear stress distribution is also affected by the CNT distribution. For example, the FGO beam exhibits the highest shear stresses, followed by the UD, FGA, and FGX beams in descending order. This is because the FGO beam concentrates the CNTs at the mid-plane of the beam, which increases the shear stiffness of the beam and therefore the shear stresses.

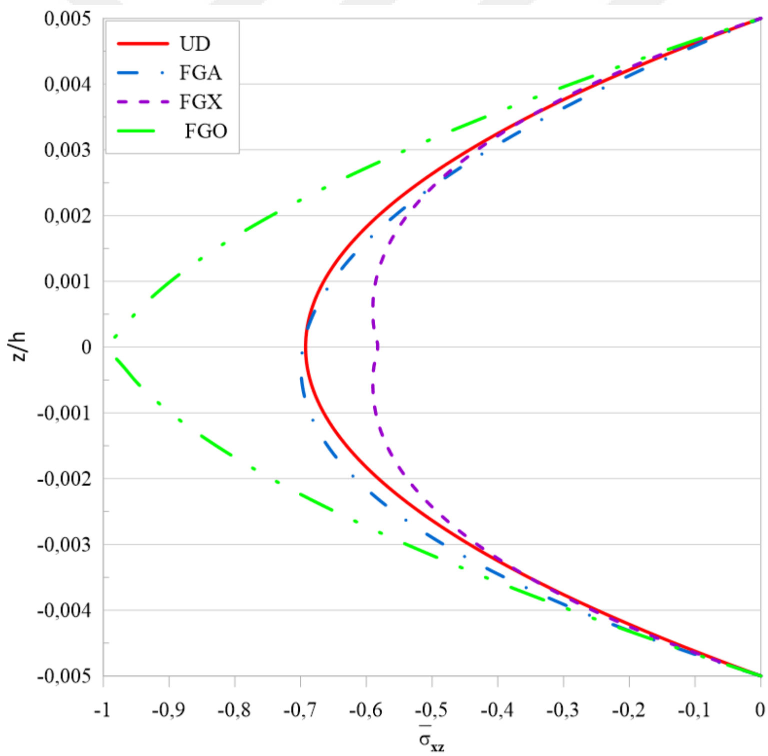

Figure 36. Dimensionless shear stresses under uniform load through beam height (C-S) (L_t/h =15) (V_{tcnt} = 0,12)

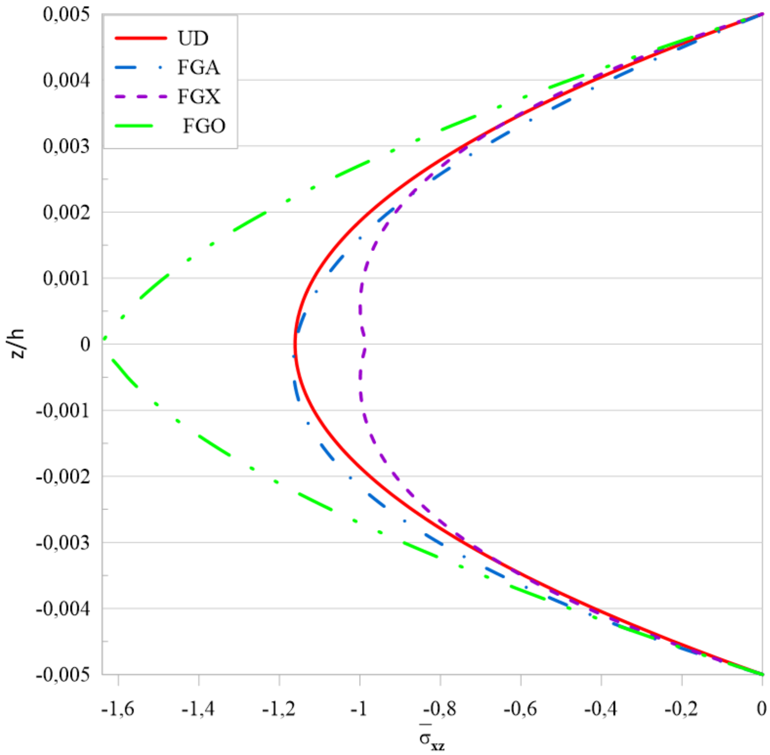

Figure 37. Dimensionless shear stresses under uniform load through beam height (C-F) (L_t/h =15) (V_{tcnt} = 0,12)

Figures 38 and 39 show the non-dimensional shear stress ($\bar{\sigma}_{xz}$) distribution along the length of a C-C and S-S FG-CNTRC beam, respectively, with a length-to-height ratio of L_t/h = 15 and a CNT volume fraction of V_{tcnt} = 0,12, for different CNT distributions. The shear stress is calculated at the mid-plane of the beam (z = 0).

The results show that the shear stress is highest at the boundaries and lowest at the mid-span of the beam. This is because the shear stress is zero at the mid-span of the beam, and the shear stress distribution is parabolic along the length of the beam.

The shear stress distribution is also affected by the CNT distribution. For example, the FGO beam exhibits the highest shear stresses, followed by the FG-V, FG-Λ, and FGX beams in descending order. This is because the FGO distribution concentrates the CNTs at the mid-plane of the beam, which increases the shear stiffness of the beam and therefore the shear stresses.

In Figure 38 and 39, the UD beam is the red line that is again almost completely overlapping with the green line (FGX beam).

The reason why the UD and FGX beams have similar shear stress distributions is because they both have a relatively high concentration of CNTs at the mid-plane of the beam.

The UD beam has a uniform distribution of CNTs, while the FGX beam has a higher concentration of CNTs at the top and bottom surfaces, but it still has a significant amount of CNTs at the mid-plane.

In contrast, the FGA and FGO beams have a lower concentration of CNTs at the mid-plane of the beam, which results in lower shear stiffness and therefore lower shear stresses.

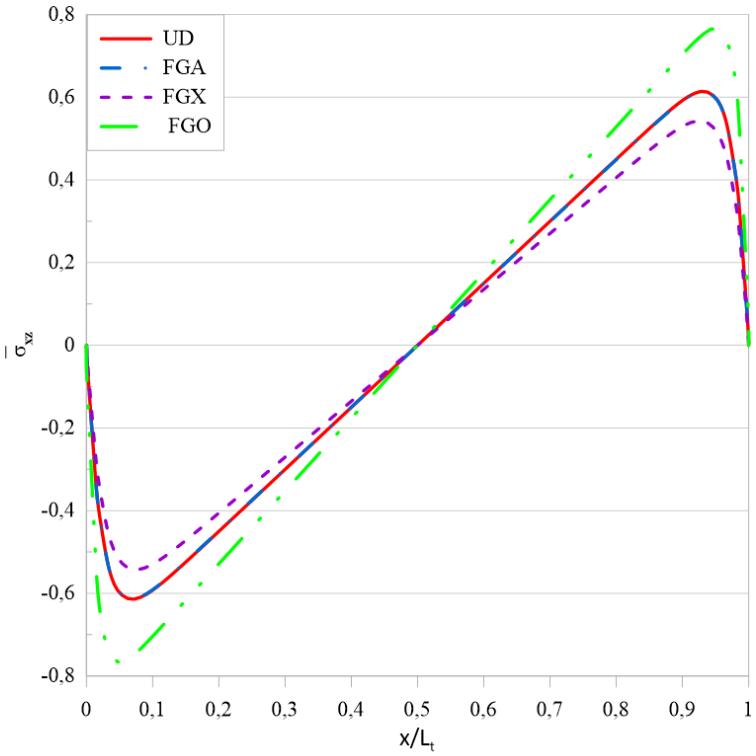

Figure 38. Non dimensional shear stress ($\bar{\sigma}_{xz}$) along the beam length at z=0 with L_t/h = 15 and $V_{tcnt} = 0{,}12$ (C-C)

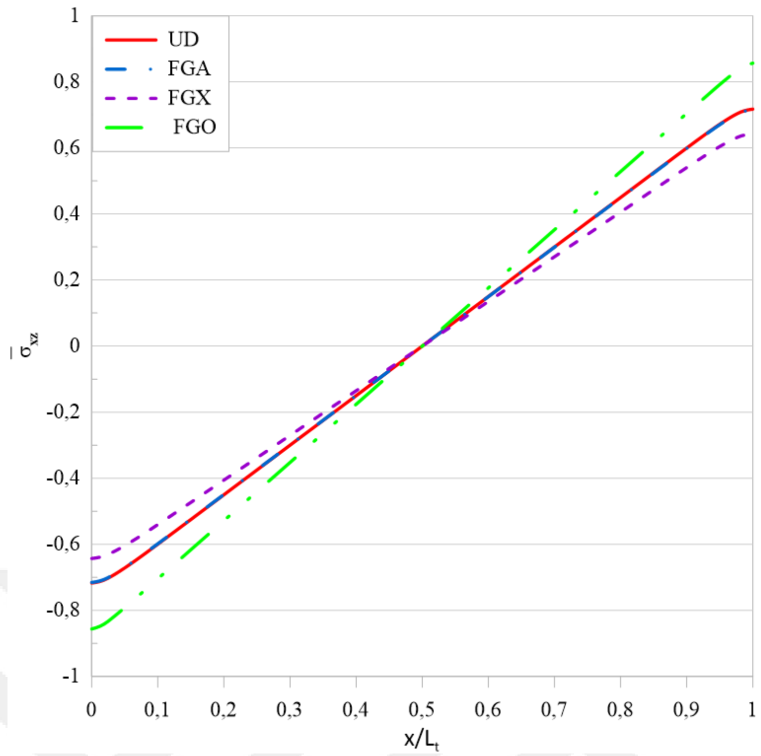

Figure 39. Non dimensional shear stress ($\bar{\sigma}_{xz}$) along the beam length at z=0 with L_t/h = 15 and $V_{tcnt} = 0{,}12$ (S-S)

Figures 40 and 41 show the $\bar{\sigma}_{xz}$ along the length of a C-S and C-F FG-CNTRC beam, respectively, with a L_t/h = 15 and a CNT volume fraction of V_{tcnt} = 0,12, for different CNT distributions. The shear stress is calculated at the mid-plane of the beam (z = 0).

The results show that the shear stress is highest at the boundaries and lowest at the mid-span of the beam. This is because the shear stress is zero at the mid-span of the beam, and the shear stress distribution is parabolic along the length of the beam.

The shear stress distribution is also affected by the CNT distribution and boundary condition. For both C-S and C-F beams, the FGO beam exhibits the highest shear stresses, followed by the UD, FGA, and FGX beams in descending order. This is because the FGO distribution concentrates the CNTs at the mid-plane of the beam, which increases the shear stiffness of the beam and therefore the shear stresses.

The C-S boundary condition demonstrates higher shear stress values compared to the C-F boundary condition. This is because the C-S boundary condition provides more constraint than the C-F boundary condition, which increases the shear stiffness of the beam and therefore the shear stresses.

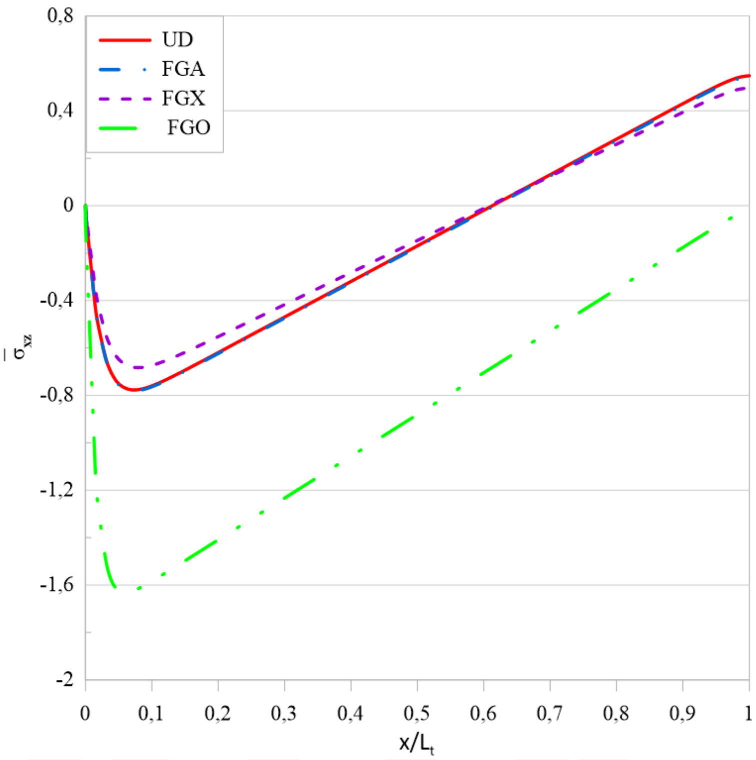

Figure 40. Non dimensional shear stress ($\bar{\sigma}_{xz}$) along the beam length at z=0 with L_t/h = 15 and $V_{tcnt} = 0{,}12$ (C-S)

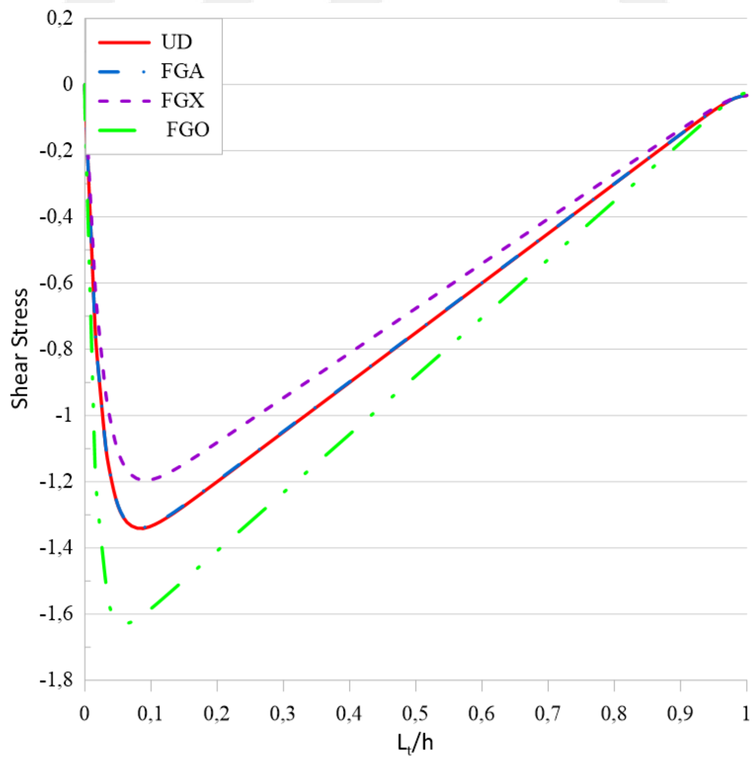

Figure 41. Non dimensional shear stress ($\bar{\sigma}_{xz}$) along the beam length at z=0 with L_t/h = 15 and $V_{tcnt} = 0{,}12$ (C-F)

3.3.3. Buckling Analysis

Buckling analysis is a type of engineering analysis that is used to predict the load at which a beam will suddenly deform and lose its ability to carry its load. This type of analysis is important for designing beams that are safe and will not collapse under normal operating conditions.

Table 29 presents the non-dimensional critical buckling load ($\bar{N}_{cr}$) of FG-CNTRC beams with various boundary conditions. To justify the accuracy and reliability of the attained values, a link is made with the results of Kumar and Srinivas (2017b), who employed Timoshenko beam theory and the FEM. The relationship reveals close agreement between the two sets of results.

Examination of the buckling values for each beam distribution under different boundary conditions demonstrates that the $\bar{N}_{cr}$ increases with increasing V_{cnt}. The FGX beam had the highest values, followed by UD, FGA, and FGO beams. Among the boundary conditions, C-C boundary showed the highest values, followed by C-S, S-S, and C-F boundary.

Table 29. $\bar{N}_{cr}$ of FG-CNTRC beams under different boundary conditions (Material Properties B, L_t/h =15, $\theta = 0$)

B.C.*	V_{tcnt}	**UD**		**FGA**		**FGX**		**FGO**	
		Kumar and Srinivas	**Present**	**Kumar and Srinivas**	**Present**	**Kumar and Srinivas**	**Present**	**Kumar and Srinivas**	**Present**
C-C	**0,12**	0,2384	0,2361	0,2034	0,1998	0,2726	0,2736	0,1759	0,1635
	0,17	0,3833	0,3782	0,322	0,3143	0,4467	0,4387	0,2751	0,2583
	0,28	0,5023	0,4999	0,4425	0,4303	0,5834	0,5469	0,382	0,3725
S-S	**0,12**	0,1088	0,1080	0,1023	0,1012	0,1419	0,1415	0,0649	0,0631
	0,17	0,166	0,1647	0,1556	0,1536	0,2201	0,2172	0,0969	0,0945
	0,28	0,2426	0,2411	0,2304	0,2265	0,3171	0,3035	0,1474	0,1452
C-S	**0,12**	0,1656	0,1644	0,1404	0,1316	0,2003	0,2007	0,1107	0,1053
	0,17	0,2601	0,2576	0,2172	0,2024	0,3208	0,3161	0,1692	0,1622
	0,28	0,3576	0,3561	0,3105	0,2889	0,4364	0,4130	0,2470	0,2411
C-F	**0,12**	0,0343	0,0342	0,0241	0,0240	0,0487	0,0486	0,0184	0,0183
	0,17	0,0509	0,0507	0,0354	0,0352	0,0728	0,0724	0,0270	0,0267
	0,28	0,0792	0,0790	0,0554	0,0551	0,1124	0,1105	0,0425	0,0422

B.C.*=Boundary Condition

Table 30 presents a comparative assessment of the buckling behavior of UD, FGX, and FGO beams, as investigated by Belarbi et al. (2023) using a hyperbolic shear deformation theory and the FEM. The comparison reveals close agreement between the outcomes obtained in the present study and those reported by Belarbi et al. (2023), with discrepancies remaining within a margin of 5%.

Across all beam types, the FGX beam consistently exhibits the highest critical buckling load, followed by the UD and FGO beams in descending order. This resulting from the concentration of CNTs at the top and bottom surfaces of the FGX beam. It is also observed that the buckling values for all beam types converge as the L_t/h ratio increases. This is because the beam becomes more slender and therefore less stiff as the L_t/h ratio increases. As a result, the buckling load becomes less sensitive to the CNT distribution and boundary condition.

Belarbi et al. (2023) report that the FGX distribution yields identical results to the UD distribution for L_t/h values of 20 and 50. Consequently, the FGX distribution was excluded from the comparison.

Table 30. $\bar{N}_{cr}$ values for FG-CNTRC beams with varying slenderness ratios ($\theta = 0$, Material Properties A, S-S)

L_t/h	$\boldsymbol{V_{tcnt}}$	**UD**		**FGX**		**FGO**	
		Present	**Belarbi et al.**	**Present**	**Belarbi et al.**	**Present**	**Belarbi et al.**
10	**0,12**	0,1721	0,1655	0,2115	0,2082	0,1088	0,1049
	0,17	0,2697	0,2593	0,3338	0,3260	0,1677	0,162
	0,28	0,3757	0,3584	0,4396	0,4270	0,2512	0,2414
15	**0,12**	0,1016	0,0988	0,1344	0,1314	0,0587	0,0574
	0,17	0,1550	0,1506	0,2067	0,2011	0,0882	0,0862
	0,28	0,2291	0,2206	0,2923	0,2811	0,1363	0,1324
20	**0,12**	0,6465	0,0630	0,0890	-	0,0357	0,0351
	0,17	0,9726	0,0946	0,1349	-	0,0530	0,0521
	0,28	0,1484	0,1430	0,1995	-	0,0831	0,0812
50	**0,12**	0,0121	0,0119	0,0177	-	0,0063	0,0062
	0,17	0,0178	0,0174	0,0262	-	0,0092	0,0091
	0,28	0,0284	0,0276	0,0415	-	0,0146	0,0144

Tables 31 and 32 present the $\overline{N}_{cr}$ of UD, FGA, FGX, and FGO beams with a slenderness ratio of $L_t/h = 5$, under different boundary conditions and volume fractions, and with varying θ.

The results show that, for all beam types and boundary conditions, the non-dimensional critical buckling load generally decreases while the CNT θ increases from 0° to 90°. The stiffness of the beam in the axial direction increases as the CNTs become more aligned with the beam axis.

The FGX beam consistently exhibits the highest values, respected by the UD, FGA, and FGO beams in descending order. This is because the FGX distribution concentrates the CNTs at the bottom and top surfaces of the beam, which are the regions that experience the most stress during buckling.

The C-C boundary condition demonstrates the highest buckling load values, respected by the C-S, S-S, and C-F boundary conditions. This is because the C-C boundary condition provides the most constraint, which increases the stiffness of the beam.

Overall, the results in Tables 42 and 43 show that the CNT orientation angle, CNT distribution, and boundary condition all have an important effect on the $\overline{N}_{cr}$ of short beams.

Tables 32 present the $\overline{N}_{cr}$ of UD, FGA, FGX, and FGO beams with a $L_t/h = 20$, under different boundary conditions and volume fractions, and with varying θ.

The results demonstrate a consistent trend across all beam types and boundary conditions: the non-dimensional critical buckling load decreases as the CNT θ increases from 0° to 90°, regardless of beam length.

The FGX beam consistently exhibits the highest values, respected by the UD, FGA, and FGO beams in descending order. This is because the FGX distribution concentrates the CNTs at the bottom and top surfaces of the beam, which are the regions that experience the most stress during buckling. The C-C boundary condition demonstrates the highest $\overline{N}_{cr}$ values, followed by the C-S, S-S, and C-F boundary conditions.

Table 31. $\overline{N}_{cr}$ of UD, FGA, FGX, and FGO beams, influence of CNT orientation angle, boundary conditions, and volume fractions (L_t/h =5)

Boundary Condition	V_{tcnt}	**UD**			**FGA**		
		0°	**45°**	**90°**	**0°**	**45°**	**90°**
C-C	**0,12**	0,1914	0,1241	0,1194	0,1776	0,1241	0,1198
	0,17	0,2964	0,2113	0,2029	0,2684	0,2120	0,2044
	0,28	0,3702	0,2422	0,2312	0,3403	0,2483	0,2374
S-S	**0,12**	0,1027	0,0394	0,0374	0,0994	0,0395	0,0376
	0,17	0,1501	0,0669	0,0634	0,1439	0,0676	0,0643
	0,28	0,2058	0,0765	0,0719	0,1979	0,0805	0,0756
C-S	**0,12**	0,1425	0,0725	0,0692	0,1279	0,0724	0,0694
	0,17	0,2156	0,1232	0,1175	0,1872	0,1236	0,1183
	0,28	0,2797	0,1410	0,1336	0,2454	0,1446	0,1372
C-F	**0,12**	0,0364	0,0106	0,0100	0,0294	0,0105	0,0100
	0,17	0,0509	0,0179	0,0169	0,0393	0,0180	0,0170
	0,28	0,0752	0,0205	0,0192	0,0568	0,0210	0,0197
		FGX			**FGO**		
		0°	**45°**	**90°**	**0°**	**45°**	**90°**
C-C	**0,12**	0,2098	0,1283	0,1232	0,1540	0,1203	0,1164
	0,17	0,3262	0,2224	0,2131	0,2313	0,2023	0,1956
	0,28	0,3885	0,2703	0,2567	0,3080	0,2269	0,2179
S-S	**0,12**	0,1244	0,0415	0,0392	0,0717	0,0374	0,0358
	0,17	0,1853	0,0725	0,0683	0,0994	0,0623	0,0596
	0,28	0,2436	0,0902	0,0840	0,1403	0,0682	0,0648
C-S	**0,12**	0,1626	0,0756	0,0721	0,1080	0,0695	0,0669
	0,17	0,2486	0,1317	0,1251	0,1566	0,1163	0,1118
	0,28	0,3078	0,1620	0,1523	0,2141	0,1287	0,1229
C-F	**0,12**	0,0482	0,0112	0,0105	0,0229	0,0100	0,0095
	0,17	0,0689	0,0196	0,0184	0,0303	0,0166	0,0158
	0,28	0,1004	0,0246	0,0228	0,0443	0,0180	0,0170

Table 32. $\overline{N}_{cr}$ of UD, FGA, FGX, and FGO beams, influence of CNT orientation angle, boundary conditions, and volume fractions (L_t/h =20)

Boundary Condition	V_{tcnt}	**UD**			**FGA**		
		0°	**45°**	**90°**	**0°**	**45°**	**90°**
C-C	**0,12**	0,1802	0,0106	0,0100	0,1445	0,0105	0,0100
	0,17	0,2826	0,0179	0,0169	0,2223	0,0180	0,0170
	0,28	0,3900	0,0205	0,0192	0,3170	0,0210	0,0197
S-S	**0,12**	0,0693	0,0027	0,0025	0,0643	0,0027	0,0026
	0,17	0,1040	0,0046	0,0043	0,0962	0,0046	0,0044
	0,28	0,1573	0,0052	0,0049	0,1460	0,0055	0,0051
C-S	**0,12**	0,1158	0,0055	0,0052	0,0883	0,0054	0,0052
	0,17	0,1779	0,0093	0,0087	0,1332	0,0093	0,0088
	0,28	0,2565	0,0106	0,0099	0,1971	0,0109	0,0102
C-F	**0,12**	0,0200	0,0007	0,0006	0,0139	0,0007	0,0006
	0,17	0,0295	0,0011	0,0011	0,0203	0,0011	0,0011
	0,28	0,0466	0,0246	0,0228	0,0320	0,0180	0,0170
		FGX			**FGO**		
		0°	**45°**	**90°**	**0°**	**45°**	**90°**
C-C	**0,12**	0,2195	0,0112	0,0105	0,1156	0,0100	0,0095
	0,17	0,3461	0,0196	0,0184	0,1782	0,0166	0,0158
	0,28	0,4508	0,0246	0,0228	0,2648	0,0180	0,0170
S-S	**0,12**	0,0946	0,0029	0,0027	0,0385	0,0025	0,0024
	0,17	0,1430	0,0050	0,0047	0,0570	0,0042	0,0040
	0,28	0,2088	0,0063	0,0058	0,0890	0,0046	0,0043
C-S	**0,12**	0,1489	0,0058	0,0054	0,0693	0,0052	0,0049
	0,17	0,2302	0,0102	0,0095	0,1045	0,0085	0,0081
	0,28	0,3156	0,0128	0,0118	0,1592	0,0093	0,0088
C-F	**0,12**	0,0290	0,0007	0,0007	0,0105	0,0006	0,0006
	0,17	0,0428	0,0013	0,0012	0,0153	0,0011	0,0010
	0,28	0,0666	0,0016	0,0015	0,0243	0,0011	0,0011

Tables 33 present the $\overline{N}_{cr}$ for UD, FGA, FGX, and FGO beams under different slenderness ratios, boundary conditions, and volume fractions. The results show that, for all beam types, the $\overline{N}_{cr}$ decreases as the slenderness ratio increases and as the boundary conditions become looser, from C-C to C-F. Conversely, the $\overline{N}_{cr}$ increases as the volume fraction increases.

Comparison of the different beam types reveals that beams with the FGX distribution exhibit the highest $\overline{N}_{cr}$, followed by those with UD and FGA distributions, while beams with the FGO distribution consistently have the lowest $\overline{N}_{cr}$. Additionally, the C-F, S-S, and C-S boundary conditions all exhibit decreasing rates of critical buckling load change with increasing slenderness ratio, with the smallest change observed in the C-C boundary condition.

Table 33. The maximum $\bar{N}_{cr}$ of UD, FGA, FGX, and FGO beams under different slenderness ratios, boundary and volume fractions

L_t/h	V_{tcnt}	UD				FGA			
		C-C	**S-S**	**C-S**	**C-F**	**C-C**	**S-S**	**C-S**	**C-F**
10	**0,12**	0,3073	0,1802	0,2371	0,0693	0,2782	0,1717	0,2042	0,0501
	0,17	0,5042	0,2826	0,3821	0,1040	0,4506	0,2681	0,3238	0,0742
	0,28	0,6358	0,3900	0,4991	0,1573	0,5863	0,3745	0,4373	0,1138
15	**0,12**	0,2361	0,1080	0,1644	0,0342	0,1998	0,1012	0,1316	0,0240
	0,17	0,3782	0,1647	0,2576	0,0507	0,3143	0,1536	0,2024	0,0352
	0,28	0,4999	0,2411	0,3561	0,0790	0,4303	0,2265	0,2889	0,0551
20	**0,12**	0,1802	0,0693	0,1158	0,0200	0,1445	0,0643	0,0883	0,0139
	0,17	0,2826	0,1040	0,1779	0,0295	0,2223	0,0962	0,1332	0,0203
	0,28	0,3900	0,1573	0,2565	0,0466	0,3170	0,1460	0,1971	0,0320
25	**0,12**	0,1385	0,0474	0,0841	0,0131	0,1067	0,0438	0,0621	0,0090
	0,17	0,2137	0,0706	0,1274	0,0192	0,1617	0,0650	0,0926	0,0131
	0,28	0,3050	0,1088	0,1890	0,0305	0,2373	0,1002	0,1401	0,0208
30	**0,12**	0,1080	0,0342	0,0630	0,0092	0,0809	0,0315	0,0456	0,0063
	0,17	0,1647	0,0507	0,0946	0,0135	0,1213	0,0465	0,0675	0,0092
	0,28	0,2411	0,0790	0,1431	0,0214	0,1817	0,0725	0,1035	0,0145
35	**0,12**	0,0857	0,0258	0,0486	0,0068	0,0630	0,0237	0,0347	0,0047
	0,17	0,1296	0,0380	0,0726	0,0099	0,0937	0,0348	0,0511	0,0068
	0,28	0,1933	0,0597	0,1112	0,0159	0,1423	0,0546	0,0791	0,0107
40	**0,12**	0,0693	0,0200	0,0385	0,0052	0,0501	0,0184	0,0272	0,0036
	0,17	0,1040	0,0295	0,0572	0,0076	0,0742	0,0270	0,0399	0,0052
	0,28	0,1573	0,0466	0,0885	0,0122	0,1138	0,0425	0,0622	0,0083
45	**0,12**	0,0569	0,0160	0,0311	0,0041	0,0407	0,0147	0,0219	0,0028
	0,17	0,0850	0,0236	0,0461	0,0061	0,0601	0,0215	0,0320	0,0041
	0,28	0,1300	0,0373	0,0719	0,0097	0,0928	0,0340	0,0501	0,0065
50	**0,12**	0,0474	0,0131	0,0256	0,0034	0,0337	0,0120	0,0179	0,0023
	0,17	0,0706	0,0192	0,0379	0,0049	0,0495	0,0175	0,0262	0,0033
	0,28	0,1088	0,0305	0,0594	0,0079	0,0769	0,0278	0,0411	0,0053

Table 33. Continues

L_t/h	V_{tcnt}	FGX				FGO			
		C-C	S-S	C-S	C-F	C-C	S-S	C-S	C-F
10	**0,12**	0,3378	0,2195	0,2713	0,0946	0,2332	0,1156	0,1682	0,0385
	0,17	0,5505	0,3461	0,4366	0,1430	0,3820	0,1782	0,2683	0,0570
	0,28	0,6598	0,4508	0,5401	0,2088	0,5274	0,2648	0,3824	0,0890
15	**0,12**	0,2736	0,1415	0,2007	0,0486	0,1635	0,0631	0,1053	0,0183
	0,17	0,4387	0,2172	0,3161	0,0724	0,2583	0,0945	0,1622	0,0267
	0,28	0,5469	0,3035	0,4130	0,1105	0,3725	0,1452	0,2411	0,0422
20	**0,12**	0,2195	0,0946	0,1489	0,0290	0,1156	0,0385	0,0693	0,0105
	0,17	0,3461	0,1430	0,2302	0,0428	0,1782	0,0570	0,1045	0,0153
	0,28	0,4508	0,2088	0,3156	0,0666	0,2648	0,0890	0,1592	0,0243
25	**0,12**	0,1757	0,0664	0,1120	0,0190	0,0841	0,0257	0,0481	0,0068
	0,17	0,2730	0,0994	0,1709	0,0281	0,1274	0,0378	0,0717	0,0099
	0,28	0,3697	0,1491	0,2431	0,0441	0,1931	0,0594	0,1109	0,0158
30	**0,12**	0,1415	0,0486	0,0861	0,0134	0,0631	0,0183	0,0350	0,0048
	0,17	0,2172	0,0724	0,1301	0,0198	0,0945	0,0267	0,0519	0,0069
	0,28	0,3035	0,1105	0,1901	0,0312	0,1452	0,0422	0,0809	0,0110
35	**0,12**	0,1150	0,0370	0,0676	0,0100	0,0487	0,0136	0,0265	0,0035
	0,17	0,1750	0,0548	0,1015	0,0146	0,0724	0,0199	0,0391	0,0051
	0,28	0,2507	0,0846	0,1511	0,0232	0,1123	0,0315	0,0613	0,0081
40	0,12	0,0946	0,0290	0,0542	0,0077	0,0385	0,0105	0,0207	0,0027
	0,17	0,1430	0,0428	0,0809	0,0113	0,0570	0,0153	0,0304	0,0039
	0,28	0,2088	0,0666	0,1223	0,0179	0,0890	0,0243	0,0479	0,0062
45	0,12	0,0788	0,0232	0,0442	0,0061	0,0312	0,0084	0,0166	0,0021
	0,17	0,1185	0,0343	0,0658	0,0089	0,0460	0,0122	0,0243	0,0031
	0,28	0,1756	0,0537	0,1005	0,0142	0,0720	0,0194	0,0384	0,0049
50	0,12	0,0664	0,0190	0,0367	0,0049	0,0257	0,0068	0,0136	0,0017
	0,17	0,0994	0,0281	0,0545	0,0073	0,0378	0,0099	0,0199	0,0025
	0,28	0,1491	0,0441	0,0839	0,0116	0,0594	0,0158	0,0314	0,0040

Figure 42, which is derived from the data in Tables 46 and 47, shows the result of the L_t/h ratio on the $\overline{N}_{cr}$ parameters of CNT composite beams.

The beams are made of four different types of functionally graded FG-CNTRCs: UD, FGA, FGX, and FGO. The figure also shows the results for four various boundary conditions: C-C, C-S, S-S, and C-F.

The results show that, for all beam types and boundary conditions, the $\overline{N}_{cr}$ decreases as the slenderness ratio increases. This is because the beam becomes more slender and therefore less stiff as the L_t/h ratio increases. A stiffer beam will deflect less than a less stiff beam when subjected to the same load. As the L_t/h ratio of a beam increases, the beam becomes slenderer.

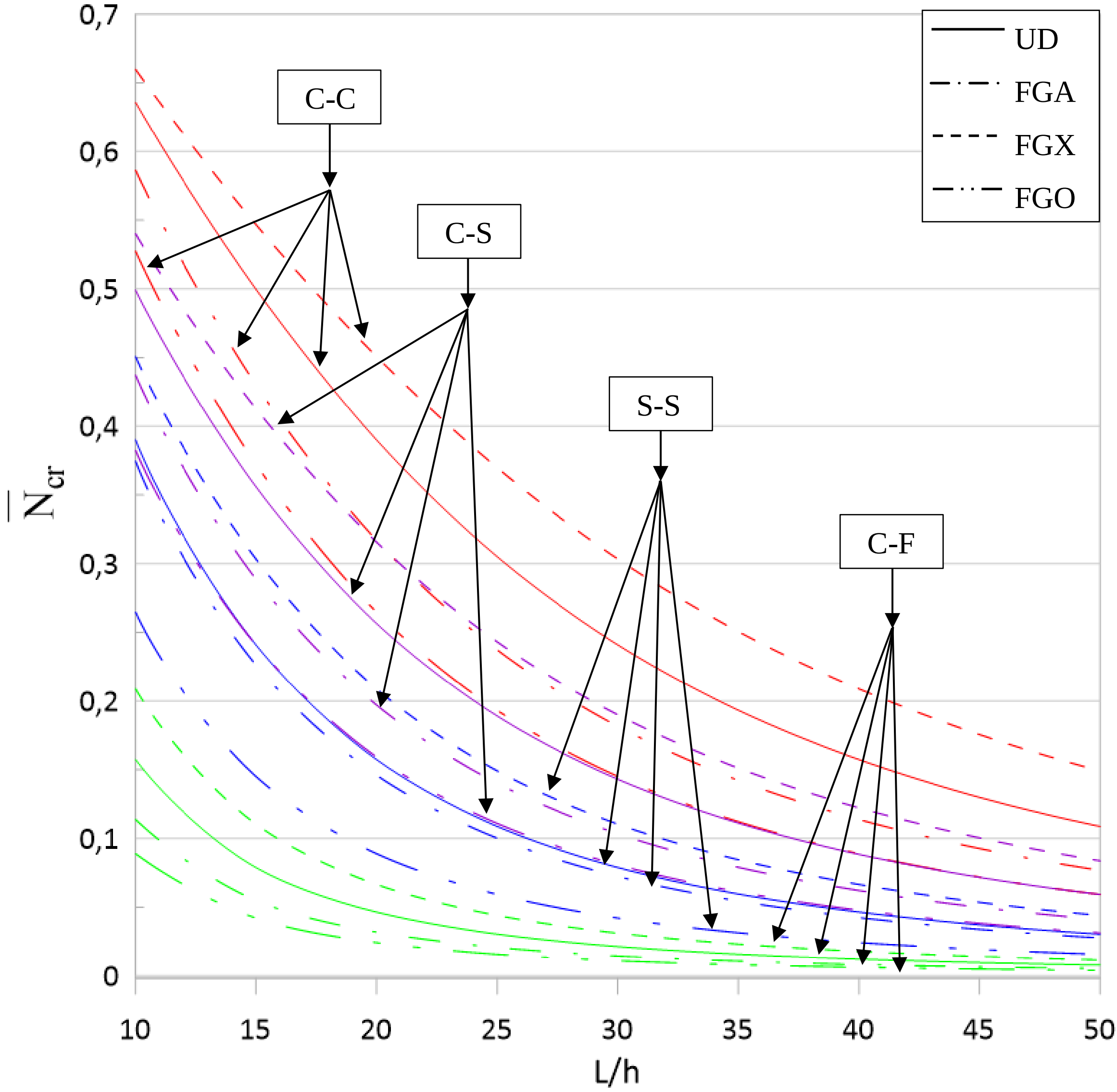

Figure 42. Influence of slenderness ratio on $\overline{N}_{cr}$ of beams (V_{tcnt} = 0,28)

Figures 43 to 46 depict the first mode shapes of UD, FGA, FGX, and FGO beams under buckling analysis. For beams with C-C and S-S boundary conditions, the maximum deflection occurs at the beam's midpoint due to the symmetrical nature of the constraints. However, this behavior is not observed for the C-S boundary condition, where the maximum deflection is shifted towards the simply supported end. Additionally, the C-F beam does not exhibit zero deflection at the right end, as would be expected for a free end.

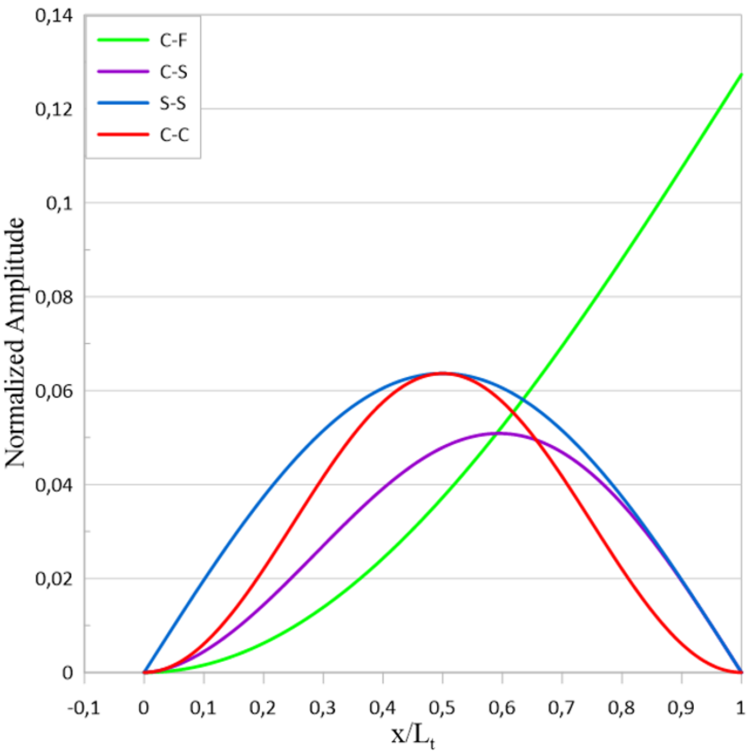

Figure 43. Effect of boundary conditions on the $\overline{N}_{cr}$ of UD beams ($V_{tcnt} = 0{,}28$)

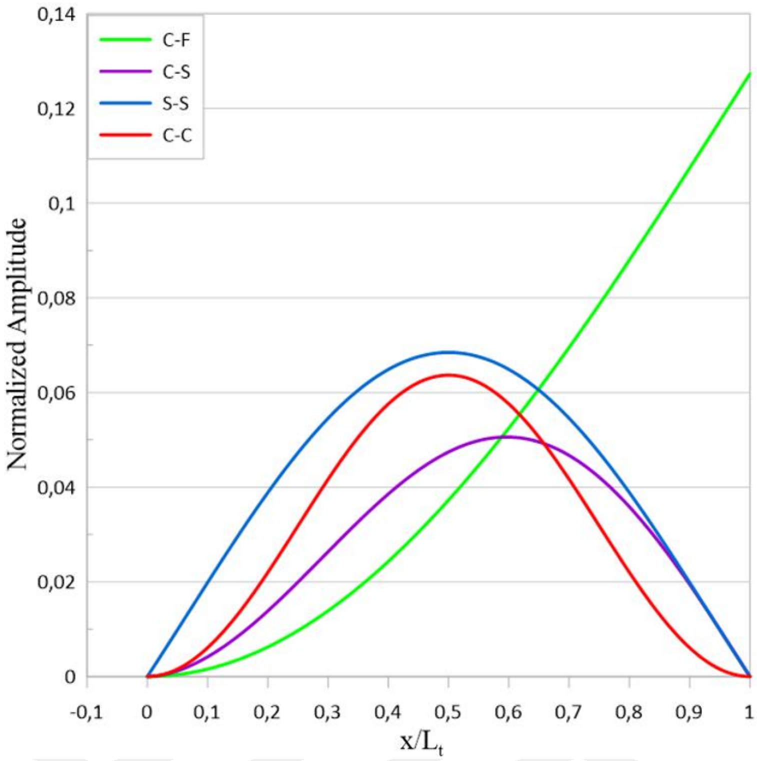

Figure 44. Effect of boundary conditions on the $\overline{N}_{cr}$ of FGA beams ($V_{tcnt} = 0,28$)

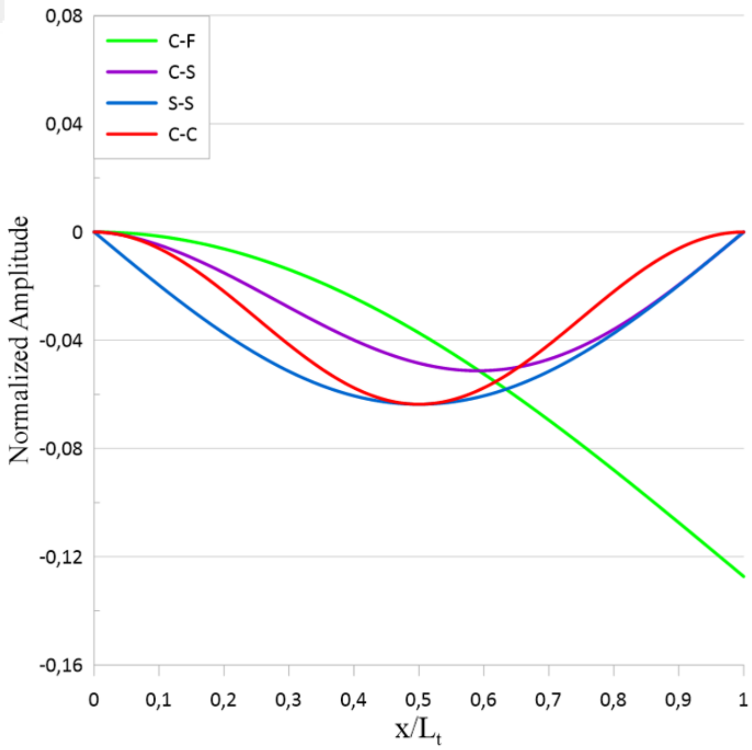

Figure 45. Effect of boundary conditions on the $\overline{N}_{cr}$ of FGX beams ($V_{tcnt} = 0,28$)

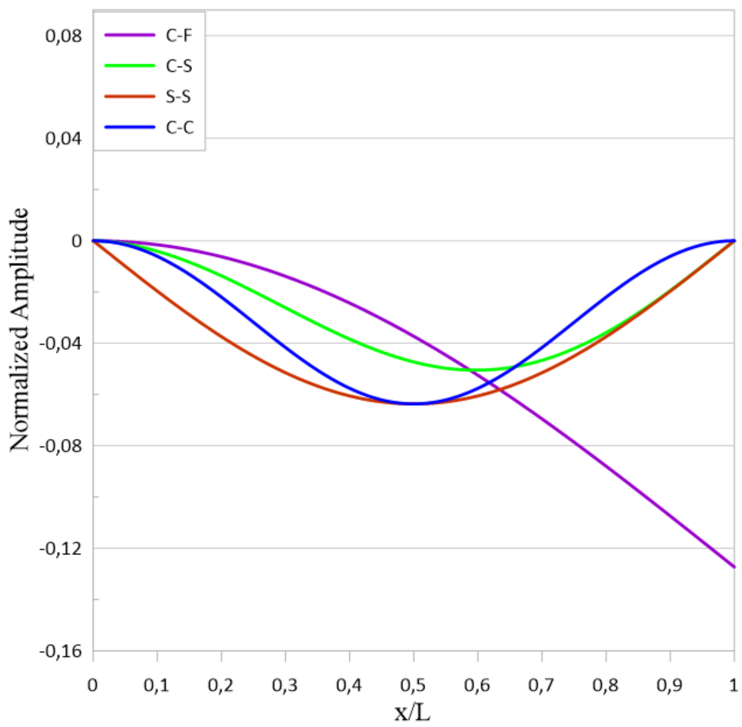

Figure 46. Effect of boundary conditions on the $\overline{N}_{cr}$ of FGO beams ($V_{tcnt} = 0{,}28$)

Figures 47 to 50 depict the first five non-dimensional buckling modes for UD, FGA, FGX, and FGO beams under various boundary conditions. Each figure illustrates the impact of different boundary conditions on the modal behavior of a single beam specimen.

In Figure 47, the first mode shape for all boundary conditions is a single half-sine wave, with the maximum deflection occurring at the midpoint of the beam. However, the higher mode shapes differ depending on the boundary condition. For example, the second mode shape for the C-C beam is a full sine wave, while the second mode shape for the C-F beam is a single half-sine wave with the maximum deflection occurring at the free end.

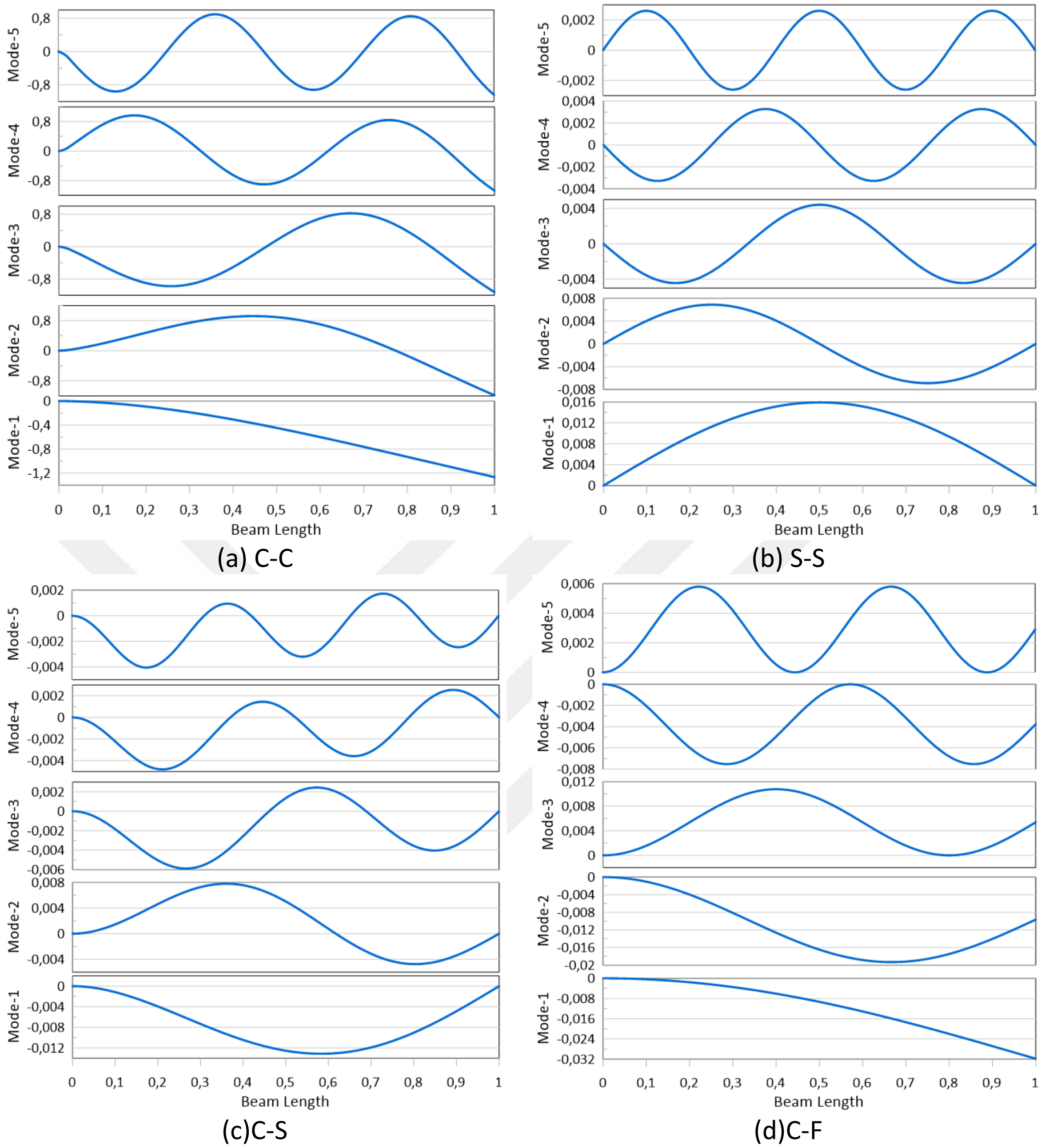

Figure 47. First five modes of UD beams with different boundary conditions at $\overline{N}_{cr}$ ($L_t/h=5$ and $V_{tcnt} = 0{,}12$)

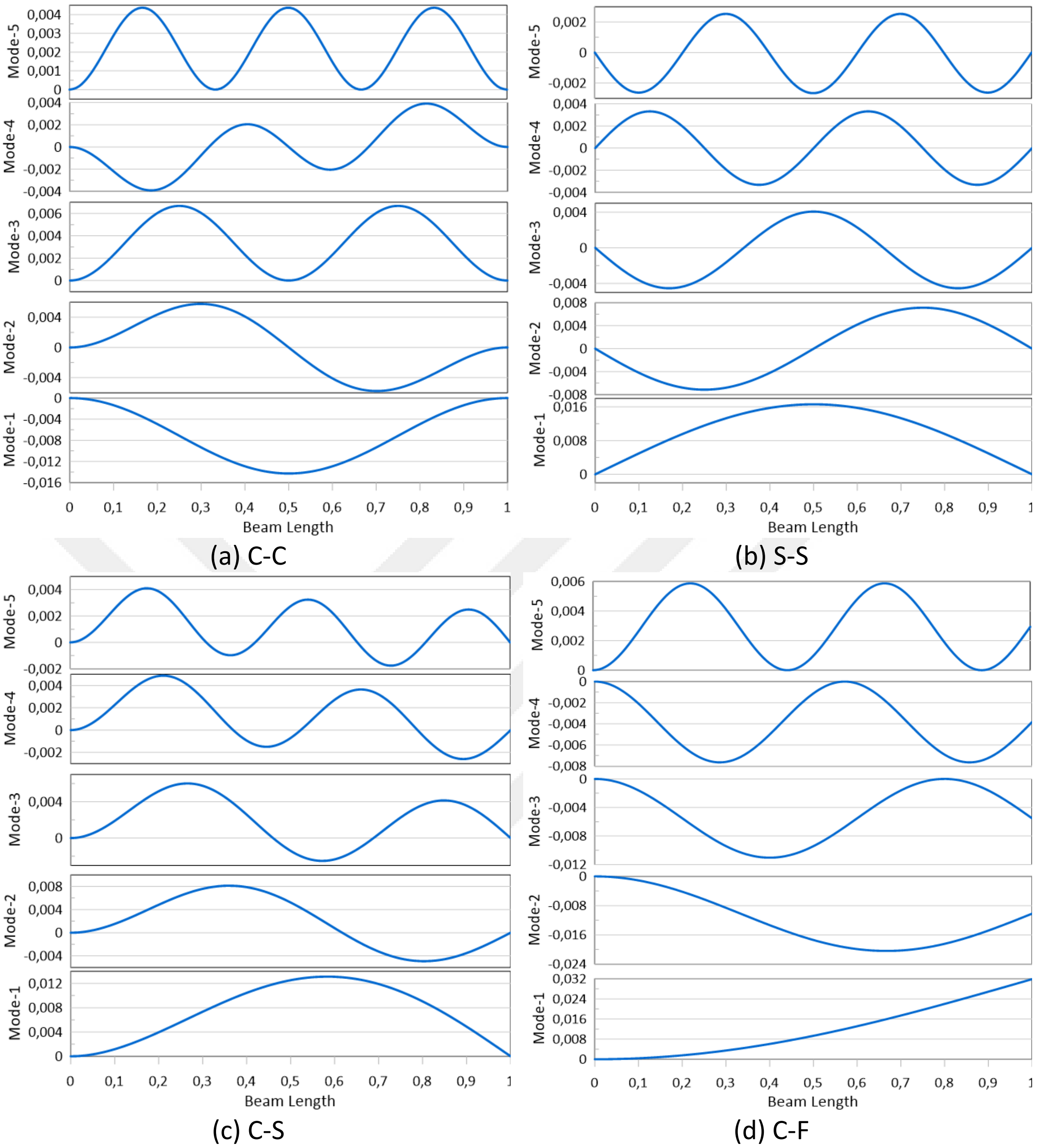

Figure 48. First five modes of FGA beams with different boundary conditions at $\overline{N}_{cr}$ (L_t/h=5 and $V_{tcnt} = 0{,}12$)

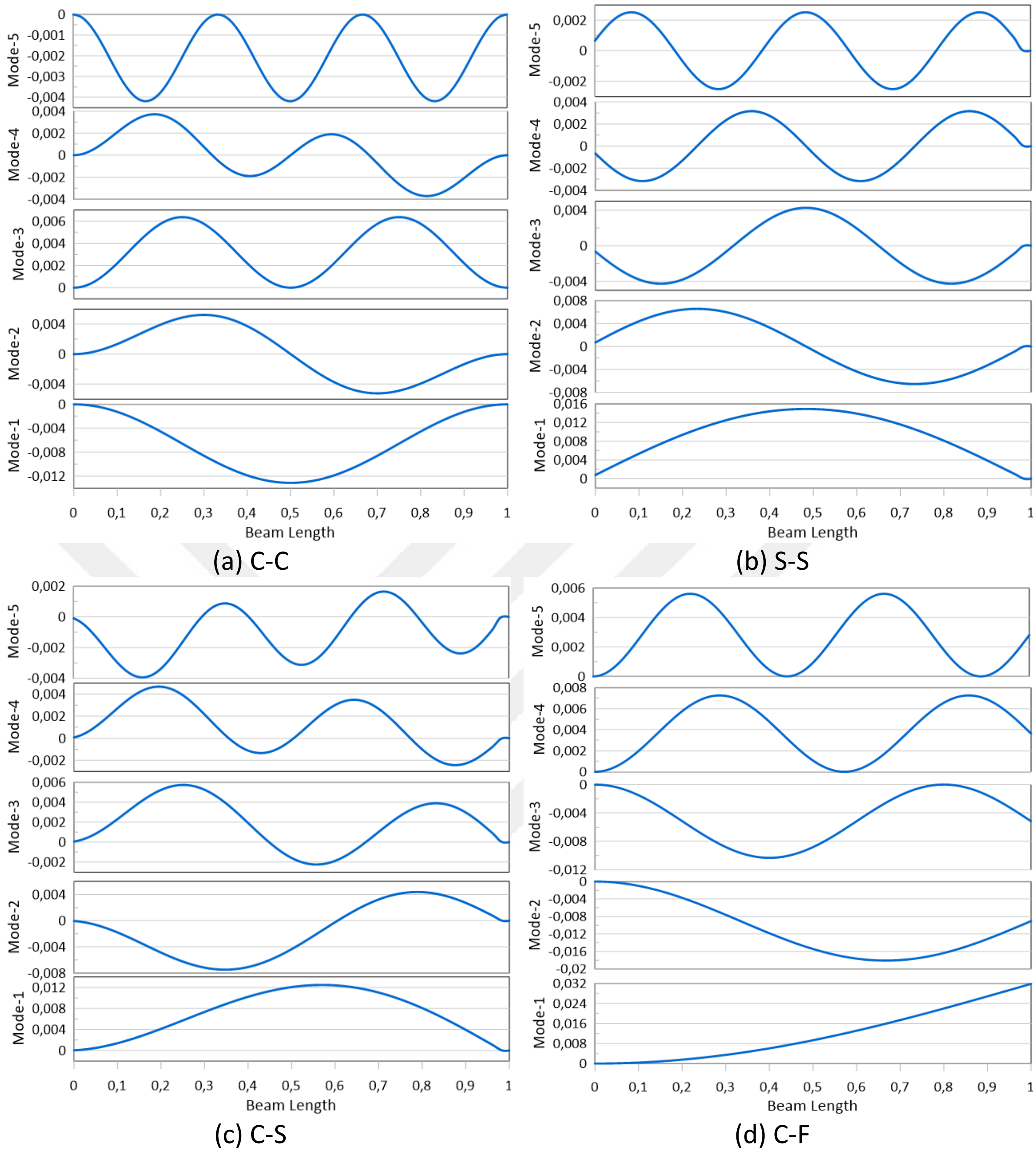

Figure 49. First five modes of FGX beams with different boundary conditions at $\overline{N}_{cr}$ (L_t/h=5 and $V_{tcnt} = 0,12$)

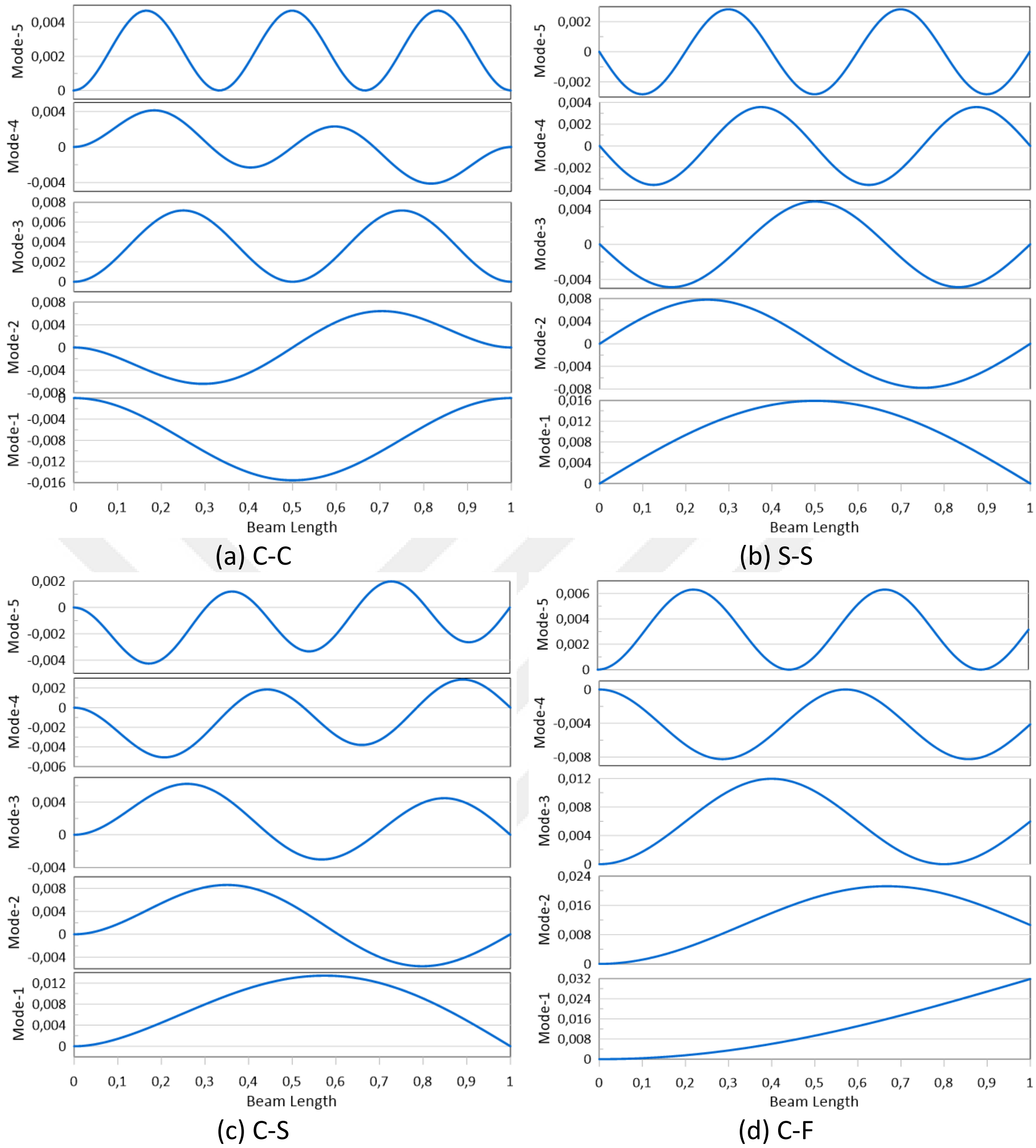

Figure 50. First five modes of FGO beams with different boundary conditions at $\overline{N}_{cr}$ (L_t/h=5 and $V_{tcnt} = 0{,}12$)

4. CONCLUSION

This study has investigated the free vibration, bending, and buckling behavior of functionally graded FG-CNTRC beams using a HSDT and the FEM. The results show that the CNT distribution, CNT orientation angle, and boundary condition all have a significant effect on the free vibration, buckling, and bending responses of FG-CNTRC beams.

Specifically, the FGX beam consistently exhibits the highest natural frequencies, lowest displacement values, and highest critical buckling load; thereafter, the UD, FGA, and FGO beams demonstrate progressively lower values. This is because the FGX distribution concentrates the CNTs at the outermost layers of the beam, where the stresses are most significant during vibration, bending, and buckling.

The C-C boundary condition also demonstrates the highest natural frequencies, lowest displacement values, and highest critical buckling load, followed by the C-S, S-S, and C-F boundary conditions. This is because the C-C boundary condition provides the most constraint, which increases the stiffness of the beam and reduces the amount of deflection and buckling.

Overall, the results of presents valuable insights into the behavior of FG-CNTRC beams under various loading conditions. This information can be used to design and optimize FG-CNTRC beams for various structural applications.

This study has focused on the free vibration, bending, and buckling behavior of FG-CNTRC beams. Future studies could investigate other aspects of the mechanical behavior of FG-CNTRC beams, such as their forced vibration and post-buckling behavior. Additionally, future studies could investigate the effect of other factors, such as temperature and moisture, on the mechanical behavior of FG-CNTRC beams.

Another potential area of future research is the development of new and improved methods for manufacturing FG-CNTRC beams. This could lead to the development of FG-CNTRC beams with even better mechanical properties.

Finally, future studies could investigate the use of FG-CNTRC beams in various structural applications, such as aerospace, automotive, and civil engineering.

5. REFERENCES

Alimirzaei, S., Mohammadimehr, M., & Tounsi, A. (2019). Nonlinear analysis of viscoelastic micro-composite beam with geometrical imperfection using FEM: MSGT electro-magneto-elastic bending, buckling and vibration solutions. *Struct Eng Mech*, *71*(5), 485-502.

Ansari, R., Shojaei, M. F., Mohammadi, V., Gholami, R., & Sadeghi, F. (2014). Nonlinear forced vibration analysis of functionally graded carbon nanotube-reinforced composite Timoshenko beams. *Composite Structures*, *113*, 316-327.

Arefi, M., Pourjamshidian, M., & Ghorbanpour Arani, A. (2017). Application of nonlocal strain gradient theory and various shear deformation theories to nonlinear vibration analysis of sandwich nano-beam with FG-CNTRCs face-sheets in electro-thermal environment. *Applied Physics A*, *123*, 1-18.

Bathe, K.J., (2019). Finite Element Procedures 2nd Edition. Massachusetts:United State of America

Baddour, C. E., & Briens, C. (2005). Carbon nanotube synthesis: a review. *International journal of chemical reactor engineering*, *3*(1).

Belarbi, M.-O., Salami, S. J., Garg, A., Daikh, A.-A., Houari, M.-S.-A., Dimitri, R., & Tornabene, F. (2023). Mechanical behavior analysis of FG-CNT-reinforced polymer composite beams via a hyperbolic shear deformation theory. *Continuum Mechanics and Thermodynamics*, *35*(2), 497-520.

Biswas, S., & Datta, P. (2021). Finite element model for free vibration analyses of FG-CNT reinforced composite beams using refined shear deformation theories. IOP Conference Series: Materials Science and Engineering,

Bousahla, A. A., Bourada, F., Mahmoud, S., Tounsi, A., Algarni, A., Bedia, E. A., & Tounsi, A. (2020). Buckling and dynamic behavior of the simply supported CNT-RC beams using an integral-first shear deformation theory. *Computers and Concrete, An International Journal*, *25*(2), 155-166.

Chaudhari, V. K., & Lal, A. (2016). Nonlinear free vibration analysis of elastically supported nanotube-reinforced composite beam in thermal environment. *Procedia Engineering*, *144*, 928-935.

Dash, S., Chakraborty, S., Dey, T., & Kumar, R. (2022). Buckling and free vibration analysis of randomly distributed CNT reinforced composite beam under thermomechanical loading. *European Journal of Mechanics-A/Solids*, *96*, 104749.

Ebrahimi, F., & Rostami, P. (2018). Wave propagation analysis of carbon nanotube reinforced composite beams. *The European Physical Journal Plus*, *133*, 1-12.

Eghbali, M., & Hosseini, S. A. (2023). On Moving Harmonic Load and Dynamic Response of Carbon Nanotube-Reinforced Composite Beams using Higher-Order Shear Deformation Theories. *Mechanics Of Advanced Composite Structures*, *10*(2), 257-270.

El-Ashmawy, A., & Xu, Y. (2021). Combined effect of carbon nanotubes distribution and orientation on functionally graded nanocomposite beams using finite element analysis. *Materials Research Express*, *8*(1), 015012.

García-Macías, E., Rodriguez-Tembleque, L., Castro-Triguero, R., & Sáez, A. (2017). Buckling analysis of functionally graded carbon nanotube-reinforced curved panels under axial compression and shear. *Composites Part B: Engineering*, *108*, 243-256.

Garg, A., Chalak, H., Zenkour, A., Belarbi, M.-O., & Sahoo, R. (2022). Bending and free vibration analysis of symmetric and unsymmetric functionally graded CNT reinforced sandwich beams containing softcore. *Thin-Walled Structures*, *170*, 108626.

Han, Y., & Elliott, J. (2007). Molecular dynamics simulations of the elastic properties of polymer/carbon nanotube composites. *Computational Materials Science*, *39*(2), 315-323.

Houalef, I. E., Bensaid, I., Saimi, A., & Cheikh, A. (2023). An analysis of vibration and buckling behaviors of nano-composite beams reinforced with agglomerated carbon nanotubes via differential quadrature finite element method. *Mechanics of Advanced Materials and Structures*, 1-19.

Karamanli, A., & Vo, T. P. (2021). Finite element model for carbon nanotube-reinforced and graphene nanoplatelet-reinforced composite beams. *Composite Structures*, *264*, 113739.

Kumar, M., & Sarangi, S. K. (2021). Harmonic response of carbon nanotube reinforced functionally graded beam by finite element method. *Materials Today: Proceedings*, *44*, 4531-4536.

Kumar, P., & Srinivas, J. (2017a). Free vibration, bending and buckling of a FG-CNT reinforced composite beam: Comparative analysis with hybrid laminated composite beam. *Multidiscipline Modeling in Materials and Structures*, *13*(4), 590-611.

Kumar, P., & Srinivas, J. (2017b). Vibration, buckling and bending behavior of functionally graded multi-walled carbon nanotube reinforced polymer composite plates using the layer-wise formulation. *Composite Structures*, *177*, 158-170.

Lin, F., & Xiang, Y. (2014). Vibration of carbon nanotube reinforced composite beams based on the first and third order beam theories. *Applied Mathematical Modelling*, *38*(15-16), 3741-3754.

Iijima, S. (1991). Helical microtubules of graphitic carbon. *nature*, *354*(6348), 56-58.

Madenci, E., Özkılıç, Y. O., Aksoylu, C., Asyraf, M. R. M., Syamsir, A., Supian, A. B. M., & Mamaev, N. (2023). Buckling Analysis of CNT-Reinforced Polymer Composite Beam Using Experimental and Analytical Methods. *Materials, 16*(2), 614.

Mohammadimehr, M., Mohammadi-Dehabadi, A., Alavi, S. A., Alambeigi, K., Bamdad, M., Yazdani, R., & Hanifehlou, S. (2018). Bending, buckling, and free vibration analyses of carbon nanotube reinforced composite beams and experimental tensile test to obtain the mechanical properties of nanocomposite. *Steel Compos. Struct., Int. J, 29*(3), 405-422.

Murmu, T., & Pradhan, S. (2009). Buckling analysis of a single-walled carbon nanotube embedded in an elastic medium based on nonlocal elasticity and Timoshenko beam theory and using DQM. *Physica E: Low-dimensional Systems and Nanostructures, 41*(7), 1232-1239.

Mustafa, A., & Aydogdu, M. (2016). Bending of CNTs under the partial uniform load. *International Journal of Engineering and Applied Sciences*, *8*(2), 21-29.

Pradhan, S., & Mandal, U. (2013). Finite element analysis of CNTs based on nonlocal elasticity and Timoshenko beam theory including thermal effect. *Physica E: Low-dimensional Systems and Nanostructures, 53*, 223-232.

Reddy, J. N. (2003). *Mechanics of laminated composite plates and shells: theory and analysis*. CRC press.

Shen, H.-S., & Xiang, Y. (2013). Nonlinear analysis of nanotube-reinforced composite beams resting on elastic foundations in thermal environments. *Engineering Structures*, *56*, 698-708.

Şimşek, M., & Reddy, J. (2013). Bending and vibration of functionally graded microbeams using a new higher order beam theory and the modified couple stress theory. *International Journal of Engineering Science*, *64*, 37-53.

Tagrara, S., Benachour, A., Bouiadjra, M. B., & Tounsi, A. (2015). On bending, buckling and vibration responses of functionally graded carbon nanotube-reinforced composite beams. *Steel and Composite Structures*, *19*(5), 1259-1277.

Thai, H.-T., & Vo, T. P. (2012). Bending and free vibration of functionally graded beams using various higher-order shear deformation beam theories. *International journal of mechanical sciences*, *62*(1), 57-66.

Thostenson, E. T., Ren, Z., & Chou, T.-W. (2001). Advances in the science and technology of carbon nanotubes and their composites: a review. *Composites science and technology*, *61*(13), 1899-1912.

Vo-Duy, T., Ho-Huu, V., & Nguyen-Thoi, T. (2019). Free vibration analysis of laminated FG-CNT reinforced composite beams using finite element method. *Frontiers of Structural and Civil Engineering, 13*, 324-336.

Vodenitcharova, T., & Zhang, L. (2006). Bending and local buckling of a nanocomposite beam reinforced by a single-walled carbon nanotube. *International journal of solids and structures, 43*(10), 3006-3024.

Wang, S., Qiao, Y., Liu, C., & Luo, L. (2022). An energy method for buckling behavior analysis of functionally graded carbon nanotube-reinforced composite sandwich structures. *Materials Research Express, 9*(12), 125306.

Wattanasakulpong, N., & Ungbhakorn, V. (2013). Analytical solutions for bending, buckling and vibration responses of carbon nanotube-reinforced composite beams resting on elastic foundation. *Computational Materials Science, 71*, 201-208.

Yang, S. (2023). Properties, applications, and prospects of carbon nanotubes in the construction industry. *Architecture, Structures and Construction*, 1-10.

Yas, M., & Samadi, N. (2012). Free vibrations and buckling analysis of carbon nanotube-reinforced composite Timoshenko beams on elastic foundation. *International Journal of Pressure Vessels and Piping, 98*, 119-128.

Yengejeh, S. I., Kazemi, S. A., & Öchsner, A. (2015). *A primer on the geometry of carbon nanotubes and their modifications*. Springer.

Zadeh, A. L., Shariati, M., & Torabi, H. (2012). Buckling analysis of carbon nanotube bundles under axial compressive, bending and torsional loadings via a structural mechanics model. *Journal of physics and chemistry of solids, 73*(11), 1282-1289.

Zerrouki, R., Karas, A., Zidour, M., Bousahla, A. A., Tounsi, A., Bourada, F., Tounsi, A., Benrahou, K. H., & Mahmoud, S. (2021). Effect of nonlinear FG-CNT distribution on mechanical properties of functionally graded nano-composite beam. *Structural Engineering and Mechanics, An Int'l Journal, 78*(2), 117-124.

RESUME

He completed his primary, middle and high schools in 2008, 2012 and 2016, respectively. In 2016, he started his bachelor's study in the Civil Engineering Department of Karadeniz Technical University. He completed his bachelor's degree in 2021 as a high honor student and was the second-best in his class. He currently works as a research assistant at the Civil Engineering Department, Karadeniz Technical University.